

# Non-synchronous Vibration due to Internal Radial Clearance in Roller Bearings

Jing Wu



Department of Mechanical Engineering  
McGill University  
Montreal, Canada

May 2010

---

A thesis submitted to McGill University  
in partial fulfillment of the requirements for the degree of  
Master of Engineering

© 2010 Jing Wu



## Abstract

Non-synchronous vibration is a common phenomenon in rotor-bearing systems which causes cabin comfort issues in mid size business jets. In rotating systems, the most significant source of non-synchronous vibration is the nonlinear contact in supporting bearings which is affected by internal radial clearance, contact materials, roller numbers and mass imbalance, etc.

In this study, a Jeffcott rotor-bearing system is modeled using the finite element method. For solutions of the system's governing equations, both the time-marching technique and harmonic balance method are used. Moreover, a modal reduction technique is applied to save the computations. For bearing contacts, three treatment approaches are adopted: the Hertz theory, the Lagrange multipliers technique and the forcing functions. Finally, the non-synchronous vibration is investigated with respect to the bearing's parameters, and the internal radial clearance is proven to play the most significant role in controlling the non-synchronous vibration.



## Résumé

Les vibrations non-synchrones représentent un problème connu des machines tournantes et sont à l'origine de problèmes acoustiques dans les avions de taille moyenne. Dans les roulements de support, ces vibrations asynchrones sont initiées par les contacts non-linéaires qui dépendent du jeu de fonctionnement, du type de matériaux en contact, du nombre de rouleaux, etc.

Ce travail est consacré à la modélisation d'un système de Jeffcott et à son traitement numérique par la méthode des éléments finis. Les équations du mouvement sont résolues par intégration temporelle directe et par la méthode de l'équilibrage harmonique. Qui plus est, des gains informatiques sont réalisés grâce à la mise en œuvre d'une méthode de synthèse modale. Le traitement des conditions de contact s'effectue selon trois approches: la théorie de Hertz, la technique des multiplicateurs de Lagrange et par chargement équivalent. Les vibrations non-synchrones sont ensuite analysées en fonction des paramètres des roulements et il est mis en évidence que le jeu de fonctionnement au sein de ces roulements est le paramètre principal caractérisant ce type de vibrations.



## Acknowledgements

I would like to express my most sincerely gratitude to my supervisors, Prof. Christophe Pierre and Dr. Mathias Legrand. Their generous efforts, patience and dedication help and encourage me throughout the course of this work. I am gratefully to Pratt & Whitney Canada, Rotordynamics Group, which supports my studies financially. Special thanks to Dr. Mathias Legrand for his scientific insights and careful reviews of the manuscript of my thesis. Moreover, deep thanks to Dr. Mathias Legrand for teaching me to program with Matlab and Maple, and precious instruction on L<sup>A</sup>T<sub>E</sub>X to write the manuscript. Let me express my great gratitude of having the opportunity to work in Structural Dynamics and Vibration Laboratory, McGill University. Many thanks to my colleagues, the kindness and team spirit of them gave me excellent memories of working here. I also want to thank Alain Batailly for helping me in Matlab and his scientific advice. I am also grateful to Zou Ting, who gave me firm support during the completion of this work. Last but not least, let me thank my parents, Wu Yirui and Wang Pei, who are at the root of every effort embedded in this work.



---

# Contents

<b>1</b>	<b>Introduction</b>	<b>1</b>
1.1	Background . . . . .	1
1.2	Motivation and Objectives . . . . .	4
<b>2</b>	<b>Jeffcott Rotor System</b>	<b>7</b>
2.1	Finite Element Model . . . . .	7
2.2	Linear Model and Modal Analysis . . . . .	12
2.3	Modal Reduction: Craig-Bampton Method . . . . .	20
2.4	Summary . . . . .	23
<b>3</b>	<b>Roller Bearings and Contact Mechanics</b>	<b>25</b>
3.1	Rolling Element Bearing Introduction . . . . .	25
3.2	Internal Radial Clearance and Bearing Contacts . . . . .	27
3.2.1	Contact Solution Methods . . . . .	27
3.2.2	Forcing Functions . . . . .	31
3.3	Roller Rotation and Ring Waviness . . . . .	33
3.4	Roller Bearing Stiffness . . . . .	35
3.5	Summary . . . . .	40
<b>4</b>	<b>Numerical Methods</b>	<b>41</b>
4.1	Time-marching Technique . . . . .	41
4.1.1	Time Step Size Convergence . . . . .	42
4.1.2	Runge-Kutta and Newmark- $\beta$ Method . . . . .	43
4.2	Time-marching with Reduced-order Model . . . . .	43
4.2.1	Hertz Approach . . . . .	45

---

4.2.2	Lagrange Multipliers Approach . . . . .	55
4.2.3	Forcing Functions Approach . . . . .	60
4.3	Harmonic Balance Method . . . . .	62
4.4	Summary . . . . .	70
<b>5</b>	<b>Non-synchronous Vibration Analysis</b>	<b>71</b>
5.1	Hertz Approach . . . . .	71
5.1.1	Sensitivity to Internal Radial Clearance . . . . .	72
5.1.2	Sensitivity to Mass Imbalance . . . . .	74
5.1.3	Sensitivity to Number of Rollers . . . . .	76
5.2	Lagrange Multipliers Approach . . . . .	77
5.2.1	Sensitivity to Internal Radial Clearance . . . . .	78
5.2.2	Sensitivity to Mass Imbalance . . . . .	79
5.2.3	Sensitivity to Number of Rollers . . . . .	79
5.3	Largest Non-synchronous Vibration with Internal Radial Clearance . . . . .	81
5.4	Summary . . . . .	83
<b>6</b>	<b>Closing Remarks</b>	<b>85</b>
6.1	Conclusions . . . . .	85
6.2	Future Work . . . . .	87
<b>A</b>	<b>Elementary Matrices</b>	<b>93</b>
<b>B</b>	<b>Forcing Functions Coefficients</b>	<b>95</b>

---

# List of Figures

2.1	Turbine machine model . . . . .	7
2.2	A typical example of rotor-bearing system . . . . .	8
2.3	Finite element model of the rotor-bearing model . . . . .	9
2.4	Elementary and disk DOFs . . . . .	10
2.5	Linearized bearing model (Lalanne and Ferraris, 1998) . . . . .	13
2.6	Linear model of the system . . . . .	14
2.7	Mode shapes of the Jeffcott rotor . . . . .	15
2.8	Convergence of finite element discretization . . . . .	16
2.9	Orbit at shaft end 1 of the first linear mode . . . . .	17
2.10	Linear modes of the system . . . . .	19
2.11	Campbell diagram . . . . .	20
3.1	Rolling element bearings (Palmgren, 1945) . . . . .	26
3.2	Roller bearing model and its geometry . . . . .	26
3.3	Internal radial clearance with respect to rotational velocity . . . . .	27
3.4	Bearing contact model (Harris and Kotzalas, 2006a) . . . . .	28
3.5	Flowchart of the Lagrange multipliers technique . . . . .	32
3.6	Roller rotation . . . . .	33
3.7	Ring waviness . . . . .	35
3.8	Force-deflection surface under radial clearance of 10 $\mu\text{m}$ . . . . .	37
3.9	Force-deflection surface under radial clearance of 60 $\mu\text{m}$ . . . . .	38
3.10	Bearing stiffness with respect to the internal radial clearance . . . . .	39
4.1	Time step size convergence . . . . .	42
4.2	Responses through Runge-Kutta method and Newmark- $\beta$ method . . . . .	43

4.3	Internal DOFs convergence . . . . .	44
4.4	Time responses of reduced-order and full-order model at $\omega = 50$ Hz . . . . .	45
4.5	Time responses of reduced-order and full-order model at $\omega = 750$ Hz . . . . .	46
4.6	Responses under $\gamma_0 = 10 \mu\text{m}$ . . . . .	47
4.7	Contact evaluations under $\gamma_0 = 10 \mu\text{m}$ . . . . .	48
4.8	Responses under $\gamma_0 = 30 \mu\text{m}$ . . . . .	49
4.9	Contact evaluations under $\gamma_0 = 30 \mu\text{m}$ . . . . .	50
4.10	Responses under $\gamma_0 = 60 \mu\text{m}$ . . . . .	51
4.11	Contact evaluations under $\gamma_0 = 60 \mu\text{m}$ . . . . .	52
4.12	Responses at $\omega = 160$ Hz . . . . .	53
4.13	Contact evaluations at $\omega = 160$ Hz . . . . .	54
4.14	Responses at $\omega = 750$ Hz . . . . .	55
4.15	Contact evaluations at $\omega = 750$ Hz . . . . .	56
4.16	Responses with $me = 8 \times 10^{-5}$ m . . . . .	57
4.17	Contact evaluations with $me = 8 \times 10^{-5}$ m . . . . .	58
4.18	Time responses with roller rotation . . . . .	59
4.19	Time response with ring waviness and varying compliance frequency . . . . .	60
4.20	Frequency responses with respect to waviness orders . . . . .	61
4.21	Responses through Lagrange multipliers technique at $\omega = 50$ Hz and $\gamma_0 = 10 \mu\text{m}$ . . . . .	62
4.22	Responses through Lagrange multipliers technique at $\omega = 50$ Hz and $\gamma_0 = 30 \mu\text{m}$ . . . . .	62
4.23	Responses through Lagrange multipliers technique at $\omega = 160$ Hz and $\gamma_0 = 10 \mu\text{m}$ . . . . .	63
4.24	Response through forcing functions with $me = 2 \times 10^{-5}$ m . . . . .	63
4.25	Response through forcing functions with $me = 4 \times 10^{-5}$ m . . . . .	64
4.26	Harmonic balance method introduction (Sinou, 2009) . . . . .	65
4.27	Comparison of HBM and time-marching technique . . . . .	67
4.28	Nonlinear responses under $\gamma_0 = 10 \mu\text{m}$ . . . . .	68
4.29	Effects of internal radial clearance on nonlinear responses . . . . .	69
5.1	Cascade diagram under effects of the internal radial clearance through Hertz approach ( $N_b = 8$ and $me = 4 \times 10^{-5}$ m) . . . . .	72

---

5.2	Cascade diagram under effects of the internal radial clearance through Hertz approach ( $N_b = 16$ and $me = 4 \times 10^{-5}$ m) . . . . .	73
5.3	Cascade diagram under effects of the mass imbalance through Hertz approach ( $N_b = 8$ and $\gamma_0 = 20 \mu\text{m}$ ) . . . . .	75
5.4	Cascade diagram under effects of the mass imbalance through Hertz approach ( $N_b = 8$ and $\gamma_0 = 60 \mu\text{m}$ ) . . . . .	76
5.5	Cascade diagram under effects of the number of rollers through Hertz approach ( $me = 4 \times 10^{-5}$ m and $\gamma_0 = 20 \mu\text{m}$ ) . . . . .	77
5.6	Cascade diagram under effects of the number of rollers through Hertz approach ( $me = 4 \times 10^{-5}$ m and $\gamma_0 = 120 \mu\text{m}$ ) . . . . .	78
5.7	Cascade diagram under effects of the internal radial clearance through Lagrange multipliers approach . . . . .	79
5.8	Cascade diagram under effects of the mass imbalance through Lagrange multipliers approach . . . . .	80
5.9	Cascade diagram under effects of the number of rollers through Lagrange multipliers approach . . . . .	81
5.10	Largest non-synchronous vibration with respect to internal radial clearance	82



# List of Tables

2.1	Natural frequencies of the system . . . . .	15
4.1	Runge-Kutta method and Newmark- $\beta$ method . . . . .	43
4.2	Full-order model and reduced-order model . . . . .	44
5.1	Curve fitting coefficients for the largest non-synchronous vibration . . . . .	82
B.1	Curve fitting coefficients for internal radial clearance . . . . .	95
B.2	Forcing function coefficients . . . . .	95



# Chapter 1

## Introduction

### 1.1 Background

The non-synchronous vibration is a common phenomenon in rotor-bearing systems. Generally, the industrial rotor-bearing systems are very complicated, thus it is difficult to model them mathematically. Therefore, a simplified system, which is the *Jeffcott rotor*, is widely used to represent rotor-bearing systems. The Jeffcott rotor includes all the basic necessary elements in a rotor-bearing system: rotating shaft, disks and supporting bearings (Adams, 1999; Papadopoulos et al., 2007). In general, in order to model the Jeffcott rotor mathematically, the *Finite Element Method* is usually employed (Nelson and McVaugh, 1976). In rotordynamic analysis, the supporting bearings are often simplified as a set of linear springs and dampers (Adams, 1999). This is the so-called *linear rotor-bearing system*. In rotordynamics, the focus is on studying the operating conditions which lead to the instability of the system (Lalanne and Ferraris, 1998). To this purpose, modal analysis is significant in studying rotor-bearing systems. In modal analysis, based on the linear system, a transformation between modal coordinates and physical coordinates can be constructed to study the *linear normal modes* (Hirsch and Smale, 1974).

Based on the full-order finite element model, the simplest way to solve the governing equations of the dynamic system is to use direct integration in time domain (Harris and Kotzalas, 2006a). Obviously, this method is very computational expensive. In rotor-bearing systems, the number of linear degrees of freedom (DOF) is substantial in comparison with that of nonlinear components. Although the nonlinear components constitute a small part of the whole DOFs, the system still behaves in a nonlinear fashion (Qu, 2002). From this

point of view, the reduction of system size is significant in improving the computational efficiency. Actually, if the number of nonlinear components is very small compared to the whole system, the computational efforts will be expected to reduce substantially (Zheng and Hasebe, 1999). In general, two popular groups of modal reduction methods are available in rotor-bearing systems: *Guyan reduction technique* (Guyan, 1965) and *Craig-Bampton reduction method* (Craig and Bampton, 1968). Guyan reduction is capable to reduce the static system size, while for dynamic systems, it is not applicable due to its low modal accuracy (Qu, 2002). The Craig-Bampton reduction method is more commonly used to reduce the DOFs in rotor-bearing systems. In the Craig-Bampton method, the boundary DOFs and the connection between internal and boundary DOFs are kept while other internal DOFs are synthesized. The Craig-Bampton modal reduction technique features high modal accuracy and low computational cost (Craig and Bampton, 1968).

One significant source of non-synchronous vibration in roller bearings is the nonlinear contact between rollers and the outer ring (Sinou, 2009). With the development of high-speed rotating machines, the contacts in roller bearings have drawn a lot of attentions recently (Harris, 2001). Actually, the modeling of contacts in rolling element bearings is complicated due to its strong nonlinearity. Several bearing parameters, such as internal radial clearance, materials of contact surface, rotational velocity, preload, etc., can play roles in the nature of contacts (Harris and Kotzalas, 2006b). Among these parameters, the effect of internal radial clearance is usually significant (Harsha, 2006b). In most bearing studies, this internal radial clearance is simplified to be independent of operating conditions (Tiwari and Gupta, 2000; Bai and Xu, 2006). In fact, the internal radial clearance is dependent of rotational velocity and can expand under oil-flow and thermal effects (Fleming et al., 2006). According to Pratt & Whitney (2008), the variance of the internal radial clearance is significant at high speeds due to oil-flow effects. Also, it opens up due to centrifugal forces of rollers against the outer ring (Fleming and Poplawski, 2005).

In general, two approaches are widely used to handle the contacts in roller bearings: the classical Hertz contact theory and the Lagrange multipliers technique (Tiwari and Gupta, 2000; Mijar and Arora, 2000). In the classical Hertz approach, the contact forces are modeled involving an approximation of contact stiffness and contact damping coefficients (Harris and Kotzalas, 2006a; Wang et al., 2007). However, in some specific working conditions, this approximation is very difficult (Cook and Young, 1999). Unlike the Hertz approach, the Lagrange multipliers technique handles the contacts as constraints of the

system (Faik and Witteman, 2000). Sahinkaya et al. (2007) used constrained Lagrangian equations of motion to model the contact dynamics and developed an efficient method to solve contact problems in rotor-magnetic bearing system through Lagrange multipliers. In the work of Carpenter et al. (1991), the explicit central difference scheme with Lagrange multipliers technique was adopted to solve the contact problems. Generally speaking, the main difference between these two methods lies in that the Hertz approach treats the contacts as external forces while the Lagrange multipliers technique handles the contacts as constraints on the generalized coordinates (Harsha, 2006a; Mijar and Arora, 2000). Besides, *forcing functions* are employed to solve bearing contact problems sometimes (Fleming and Poplawski, 2005). In some specific working conditions, it is of interest to construct a direct relationship of bearing contact force with rotational velocity, which is the so-called forcing functions (Fleming et al., 2006). The forcing functions are able to connect the bearing deflection and contact force to the operating velocity directly (Fleming and Poplawski, 2005). Based on the contact approaches, the bearing equivalent stiffness can be obtained (Tiwari and Gupta, 2000). Actually, the equivalent stiffness is inherently nonlinear which depends on internal radial clearance, materials of contact surface, preload, etc (Harris, 2001). According to Pratt & Whitney (2008), prediction of the equivalent stiffness of roller bearing with respect to the internal radial clearance is an important objective in this project. In the past years, the bearing equivalent stiffness has been extensively studied due to its high nonlinearity and complexity under operating conditions (Tiwari and Vyas, 1998). In fact, the equivalent stiffness is significant in bearing applications because the natural frequencies of rotor-bearing systems are relevant to it (Harsha, 2006b). In general, the linearization method is commonly used to get the equivalent stiffness (Harris and Kotzalas, 2006a). In this method, the equivalent stiffness is obtained through linearizing contact forces and moments over translational displacements and rotational angles (Tamura et al., 1985).

In order to obtain the system responses under effects of bearing contacts, several numerical tools are available to solve the nonlinear governing equations. The time-marching technique is often used in rotor-bearing systems, in which the solutions are obtained at each time step (White and Young, 1993). Among the existing time-marching techniques, the Runge-Kutta method, Wilson- $\theta$  algorithm and Newmark- $\beta$  method are widely adopted (Meirovitch, 2001). For systems with a large number of DOFs, the Newmark- $\beta$  method is commonly as a robust numerical tool to solve nonlinear ordinary differential equations (Harsha, 2006a). Besides, a frequency domain strategy, known as harmonic bal-

ance method (HBM), is also used (Villa et al., 2008). This HBM is known as a powerful numerical method to improve the computational efficiency for nonlinear systems (Hu and Tang, 2006). The main principle of the HBM is to transform the displacement responses and nonlinear forces from the time domain to the frequency domain (Cameron and Griffin, 1989). The second order differential equations are then transformed into a set of nonlinear algebraic equations, which can be solved using nonlinear solver, such as Newton-Raphson method (Groll and Ewins, 1989). In rotor-bearing systems, the HBM is often adopted to obtain the synchronous responses (Kim and Noah, 1990). In the work of Lalanne and Ferraris (1998), one harmonic was used to handle the system nonlinear responses. However, for strong nonlinear systems, only one harmonic is too limited (Villa et al., 2008). The influence of harmonic orders on nonlinear responses was analyzed in the work of Sinou (2009). In his study, the nonlinear unbalance response was proven to depend on harmonic orders, mass imbalance and internal radial clearance.

Within the framework of the bearing contact approaches and numerical tools, the non-synchronous vibration can be studied. In aircraft industry, the non-synchronous vibration in roller bearings is known as an important source of noise for mid-size business jets. The frequency range of this non-synchronous vibration is typically in the region which causes cabin comfort issues for mid size business jets (Pratt & Whitney, 2008). Not only the bearing's parameters have effects on the non-synchronous vibration, but also the unbalanced forces on the rotating shaft play roles in controlling it (Muszynska, 1988). Jing et al. (2005) analyzed the non-synchronous vibration in a rotor-bearing system with a flexible shaft and supporting journal bearings. A typical oil-whip phenomenon, which could lead to the failure of the rotor-bearing system, was found and analyzed. The oil-whip phenomenon was also studied by Castro et al. (2008). In their work, the authors studied the influence of imbalance on both the synchronous and non-synchronous vibrations for short journal bearings. They pointed out that, besides the journal bearing's parameters, the mass imbalance was also an important factor for the oil-whip phenomenon. Moreover, this oil-whip is independent of rotational velocity, which is called the frequency-locked phenomenon (Muszynska, 1986).

## 1.2 Motivation and Objectives

The non-synchronous vibration is not only an important source of noise in aircraft engines, but also an significant factor in leading to failures of rotor-bearing systems. Ac-

According to Pratt & Whitney (2008), this non-synchronous vibration is strongly relevant to the internal radial clearance. Hence, the investigation of the non-synchronous vibration with respect to the internal clearance is significant due to the fact that it is possible to predict dangerous operating conditions.

In this work, the key parameter controlling the non-synchronous vibration is expected to be determined. A Jeffcott rotor with two supporting roller bearings is used to represent rotor-bearing systems. The finite element method is adopted to model the Jeffcott rotor system mathematically. In order to save computational efforts, the Craig-Bampton modal reduction technique is used to reduce the system size. For the contacts in the roller bearing, two approaches are proposed to use: the Hertz contact theory and the Lagrange multipliers technique. Based on the contact solution methods, both the time-marching technique and harmonic balance method are employed to obtain the system responses. Afterwards, through fast Fourier transform of time responses for each operating velocity, the Cascade diagram is obtained to investigate the non-synchronous vibration. In our analysis, this non-synchronous vibration will be studied with respect to the internal radial clearance, the mass imbalance and the number of rollers via both the Hertz contact theory and the Lagrange multipliers technique.



---

## Chapter 2

# Jeffcott Rotor System

### 2.1 Finite Element Model

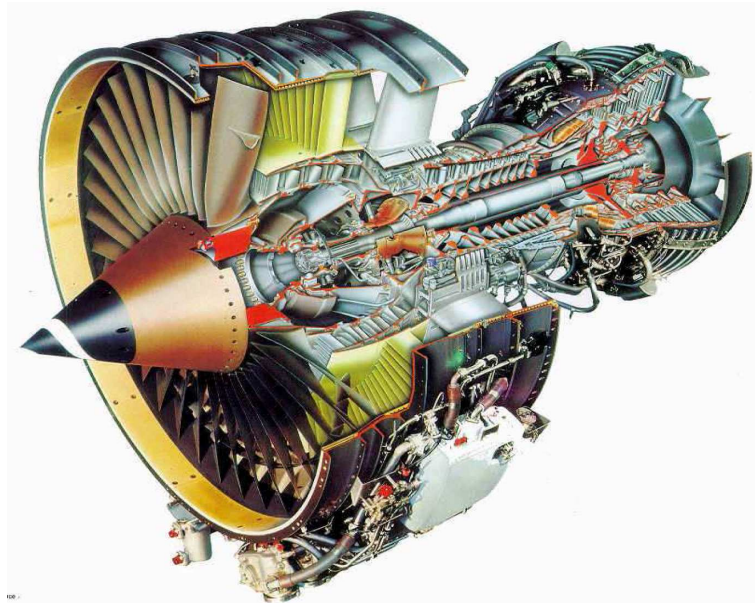


**Fig. 2.1** Turbine machine model

Rotor-bearing systems are widely used in jet engines and turbine machines as an example shown in Fig. 2.1. In general, there are three basic elements included in a rotor-bearing system: rotating shafts, attached disks and supporting bearings (Lalanne and Ferraris, 1998). A typical rotor-bearing system is depicted in Fig. 2.2. In rotor-bearing systems, the

excitation forces are due to geometric imperfections sources of mass imbalance and can not be avoided completely. The supporting forces arise from contacts in supporting bearings. Generally speaking, there are three types of supporting bearings: journal bearing, ball bearing and roller bearing. Each type has its corresponding working conditions. With the development of high speed machines, ball bearings and roller bearings are more commonly used.

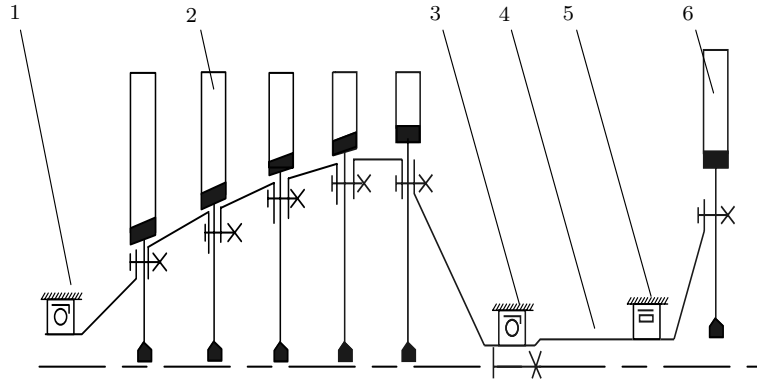


**Fig. 2.2** A typical example of rotor-bearing system: 1-ball bearing; 2-disk and blades; 3-ball bearing; 4-shaft; 5-roller bearing; 6-disk (Adams, 1999)

In 1919, a model constituted by a flexible uniform shaft with a centrally mounted disk was employed by H. H. Jeffcott, which was the so-called *Jeffcott rotor*. The Jeffcott rotor is a simplified model of the rotor-bearing system. Although it is not complicated, it contains all the necessary basic elements: disk, rotating shaft and supporting bearings (Adams, 1999). Because of its simplicity and capability to capture the nonlinear behaviors of the rotor-bearing system, the Jeffcott rotor is employed in our analysis. In order to construct the Jeffcott rotor mathematically, the finite element method (FEM) is employed. In the FEM, the flexible shaft is represented as a series of beam elements, and a concentrated mass is attached to the shaft at its center position. The finite element model of the system is shown in Fig. 2.3.

Following Adams (1999), Lagrange's equations are applied to obtain the system's governing equations as:

$$\frac{d}{dt} \left( \frac{\partial T}{\partial \dot{\mathbf{q}}} \right) - \left( \frac{\partial T}{\partial \mathbf{q}} \right) + \left( \frac{\partial U}{\partial \mathbf{q}} \right) = \mathbf{Q} \quad (2.1)$$

where  $T$  is the kinetic energy of the system,  $U$  is the strain energy,  $\mathbf{q}$  is displacement vector, “.” denotes differentiation with respect to time, and  $\mathbf{Q}$  is the generalized force vector.

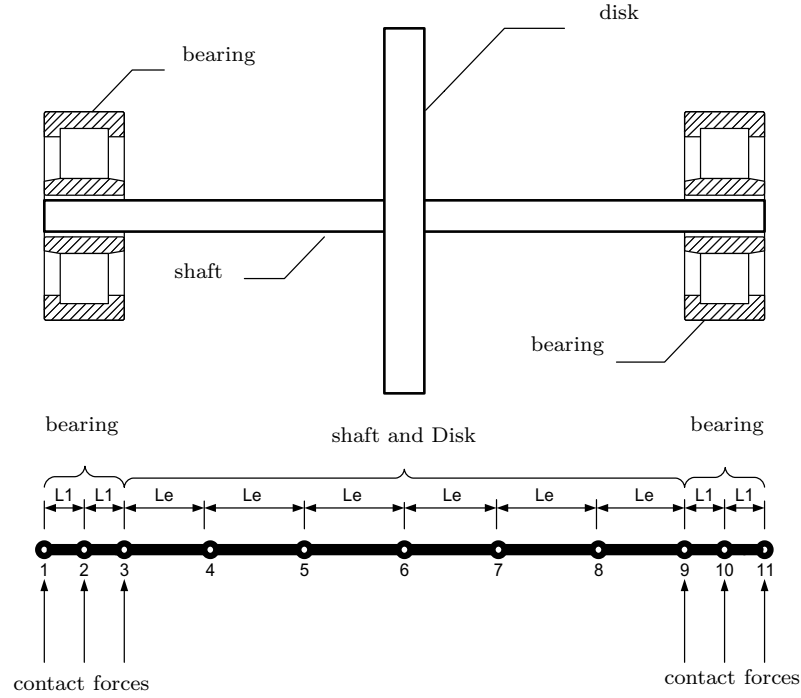


**Fig. 2.3** Finite element model of the rotor-bearing model

In our system, the shaft is represented as Euler-Bernoulli beam with a circular cross section and is characterized by kinetic and strain energies. According to Lalanne and Ferraris (1998), the kinetic energy for the beam element is expressed as:

$$T = \frac{\rho A}{2} \int_0^l (\dot{u}_y^2 + \dot{u}_x^2) dz + \frac{\rho I}{2} \int_0^l (\dot{\theta}_y^2 + \dot{\theta}_x^2) dz + \rho I l \omega^2 + 2\rho I \omega \int_0^l \dot{\theta}_y \dot{\theta}_x dz \quad (2.2)$$

where  $\rho$  is the density,  $A$  is the cross section area of the beam,  $I$  is the area moment of inertia of the cross section about the neutral axis,  $\omega$  is the rotational velocity of the shaft,  $l$  is the length of the beam element,  $u_x$  and  $u_y$  are the nodal translational displacements, and  $\theta_y$  and  $\theta_x$  are the nodal rotational displacements. The strain energy for the beam element is written as:

$$U = \frac{EI}{2} \int_0^l \left[ \left( \frac{\partial^2 u_x}{\partial y^2} \right)^2 + \left( \frac{\partial^2 u_y}{\partial x^2} \right)^2 \right] + \frac{F_z}{2} \int_0^l \left[ \left( \frac{\partial u_x}{\partial y} \right)^2 + \left( \frac{\partial u_y}{\partial x} \right)^2 \right] dz \quad (2.3)$$

where  $F_z$  is the axial force, and  $E$  is the elastic modulus. It is noticeable that the shaft is

symmetric, i.e.,  $I_x = I_y = I$ .

On the basis of the Lagrange's equation, the governing equation of the finite element model is given as (Lalanne and Ferraris, 1998):

$$\mathbf{M}\ddot{\mathbf{q}} + \mathbf{D}\dot{\mathbf{q}} + \mathbf{K}\mathbf{q} = \mathbf{F}_{\text{LN}} + \mathbf{F}_{\text{NL}} \quad (2.4)$$

where  $\mathbf{M} \in \mathbb{R}^{n \times n}$  is the symmetric global mass matrix,  $\mathbf{K} \in \mathbb{R}^{n \times n}$  is the symmetric global stiffness matrix, the global damping matrix  $\mathbf{D} = \omega\mathbf{G} + \alpha\mathbf{K} + \beta\mathbf{M}^1$  is anti-symmetric,  $\mathbf{G}$  is the gyroscopic matrix which is also anti-symmetric,  $\mathbf{F}_{\text{LN}} \in \mathbb{R}^n$  is linear force vector containing the gravity force and unbalanced force,  $\mathbf{F}_{\text{NL}} \in \mathbb{R}^n$  is the nonlinear force vector, which is due to contacts between rollers and the outer ring in supporting bearings. The system's global mass, damping and stiffness matrices are assembled through the corresponding  $8 \times 8$  elementary matrices of the shaft (Lalanne and Ferraris, 1998).

For the beam element, each node has four DOFs, i.e., two translational displacements ( $u_y$  and  $u_x$ ) and two rotational deflections ( $\theta_y$  and  $\theta_x$ ). The DOFs of the beam element and the central disk are shown in Figs. 2.4(a) and 2.4(b), respectively. According to Euler-

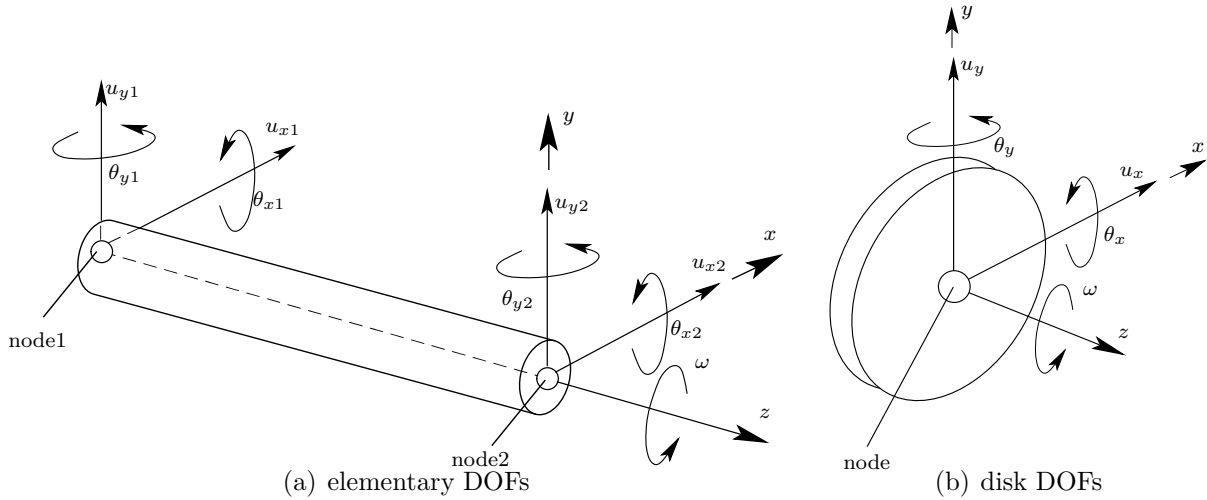


**Fig. 2.4** Elementary and disk DOFs

Bernoulli beam theory (Meirovitch, 2001), the shear effects of the beam are ignored, and plane sections are normal to the longitudinal axis. The translational and rotational DOFs

<sup>1</sup> $\alpha$  and  $\beta$  are proportional damping coefficients,  $\alpha = 0.005$ ,  $\beta = 0.01$ .

have the following relationship:

$$\theta_y = -\frac{\partial u_y}{\partial y}, \quad \theta_x = \frac{\partial u_x}{\partial x} \quad (2.5)$$

Following Papadopoulos et al. (2007), the elementary mass matrix is:

$$[M]^e = [M]_T^e + [M]_R^e \quad (2.6)$$

where  $[M]_T^e$  and  $[M]_R^e$  are the elementary translational and rotational mass matrices, which are defined as:

$$\begin{aligned} [M]_T^e &= \int_0^l \mu [\Psi]^T [\Psi] ds, \\ [M]_R^e &= \int_0^l \xi [\Phi]^T [\Phi] ds \end{aligned} \quad (2.7)$$

In Eq. (2.7),  $[\Psi]$  and  $[\Phi]$  are the translational and rotational function matrices, respectively. They are expressed as:

$$\begin{aligned} [\Psi] &= \begin{bmatrix} \psi_1 & 0 & 0 & \psi_2 & \psi_3 & 0 & 0 & \psi_4 \\ 0 & \psi_1 & -\psi_2 & 0 & 0 & \psi_3 & -\psi_4 & 0 \end{bmatrix}, \\ [\Phi] &= \begin{bmatrix} 0 & -\psi'_1 & \psi'_2 & 0 & 0 & -\psi'_3 & \psi'_4 & 0 \\ \psi'_1 & 0 & 0 & \psi'_2 & \psi'_3 & 0 & 0 & \psi'_4 \end{bmatrix} \end{aligned} \quad (2.8)$$

with

$$\begin{aligned} \psi_1 &= 1 - 3(s/l)^2 + 2(s/l)^3, \\ \psi_2 &= s[1 - 2(s/l) + (s/l)^2], \\ \psi_3 &= 3(s/l)^2 - 2(s/l)^3, \\ \psi_4 &= l[-(s/l)^2 + (s/l)^3] \end{aligned} \quad (2.9)$$

Similarly, the elementary stiffness matrix is defined by using the translational functions:

$$[K]^e = \int_0^l EI [\Psi'']^T [\Psi''] ds \quad (2.10)$$

and the elementary gyroscopic matrix is:

$$[G]^e = [N]^e - ([N]^e)^T \quad (2.11)$$

where

$$[N]^e = \int_0^l J_p [\Psi]^T [\Phi] ds \quad (2.12)$$

and  $J_p$  is the polar moment of the shaft element, which is defined as  $J_p = 1/2m_e r^2$ , where  $m_e$  is the mass of the shaft element, and  $r$  is the element radius.

The explicit form of the elementary mass, stiffness and gyroscopic matrices are given in Appendix A.

For the concentrated disk attached to the shaft, the mass and gyroscopic matrices are given by Papadopoulos et al. (2007):

$$[M_D]^n = \begin{bmatrix} m_d & & & \text{sym} \\ 0 & m_d & & \\ 0 & 0 & I_D & \\ 0 & 0 & 0 & I_D \end{bmatrix}, \quad [C_G]^n = \begin{bmatrix} 0 & \text{skew} & \text{sym} \\ 0 & 0 & \\ 0 & 0 & 0 \\ 0 & 0 & -I_P & 0 \end{bmatrix} \quad (2.13)$$

where  $I_D$  and  $I_P$  are the diametral and polar moments of the disk, which are expressed as:

$$\begin{aligned} I_D &= \frac{m_d}{12} (3R^2 + b^2), \\ I_P &= \frac{1}{2} m_d R^2 \cong 2I_D \end{aligned} \quad (2.14)$$

where  $m_d$ ,  $R$  and  $b$  are the mass, radius and width of the disk, respectively.

## 2.2 Linear Model and Modal Analysis

Generally, in linear rotor-bearing model analysis, supporting bearings are simplified as a set of springs and dampers as shown in Fig. 2.5 ( $C$  is the damping coefficient of the dampers,  $K$  is the stiffness coefficient of the springs). In this approach, the simplified bearing model is often used as constraints of the rotating shaft, which is the so-called *linear rotor-bearing system*. As illustrated in Fig. 2.6, instead of bearings, two sets of springs are used as the constraints at two ends of the shaft. In our model, each end of the shaft is attached with eight springs, in which every two are separated by  $\pi/4$ . The nodal linearized

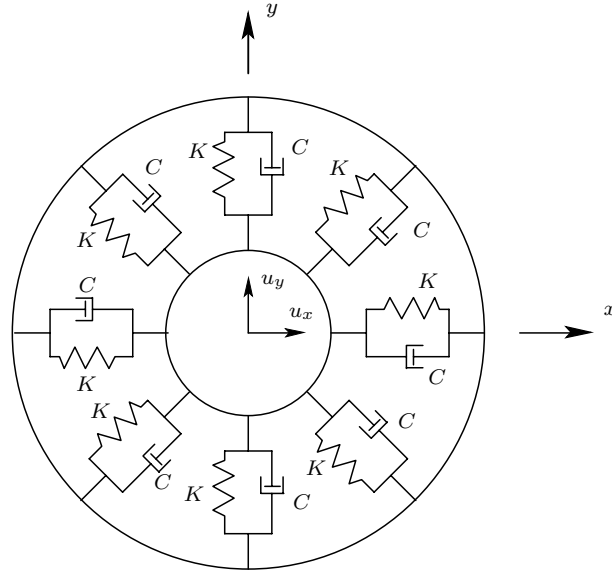


**Fig. 2.5** Linearized bearing model (Lalanne and Ferraris, 1998)

bearing stiffness matrix is:

$$\mathbf{K}_{linear} = \begin{bmatrix} K_{u_y u_y} & K_{u_y u_x} & K_{u_y \theta_y} & K_{u_y \theta_x} \\ K_{u_x u_y} & K_{u_x u_x} & K_{u_x \theta_y} & K_{u_x \theta_x} \\ K_{\theta_y u_y} & K_{\theta_y u_x} & K_{\theta_y \theta_y} & K_{\theta_y \theta_x} \\ K_{\theta_x u_y} & K_{\theta_x u_x} & K_{\theta_x \theta_y} & K_{\theta_x \theta_x} \end{bmatrix} \quad (2.15)$$

In  $\mathbf{K}_{linear}$ , each element is the partial derivative of the potential energy of the spring with respect to the corresponding generalized coordinates. The potential energy is expressed as:

$$E_p = \frac{1}{2} K \Delta l_s^2 \quad (2.16)$$

where  $\Delta l_s$  is the spring deformation. Assuming that the original length of each spring is  $l_s$ , and the angular position of the  $j^{\text{th}}$  spring is  $\theta_j$ , which is:

$$\theta_j = \frac{2\pi}{N_s} (j - 1) \quad (2.17)$$

where  $N_s$  is the number of springs (in our case,  $N_s = 8$ ), the corresponding deformation  $\Delta l_{sj}$  is expressed as:

$$\Delta l_{sj} = \sqrt{(l_s \cos \theta_j + u_x)^2 + (l_s \sin \theta_j + u_y)^2} - l_s \quad (2.18)$$

Then, elements in the linearized bearing stiffness matrix are obtained:

$$K_{u_y u_y} = \frac{\partial E_p}{\partial u_y}, \quad K_{u_x u_x} = \frac{\partial E_p}{\partial u_x}, \quad K_{\theta_y \theta_y} = \frac{\partial E_p}{\partial \theta_y}, \quad K_{\theta_x \theta_x} = \frac{\partial E_p}{\partial \theta_x} \quad (2.19)$$

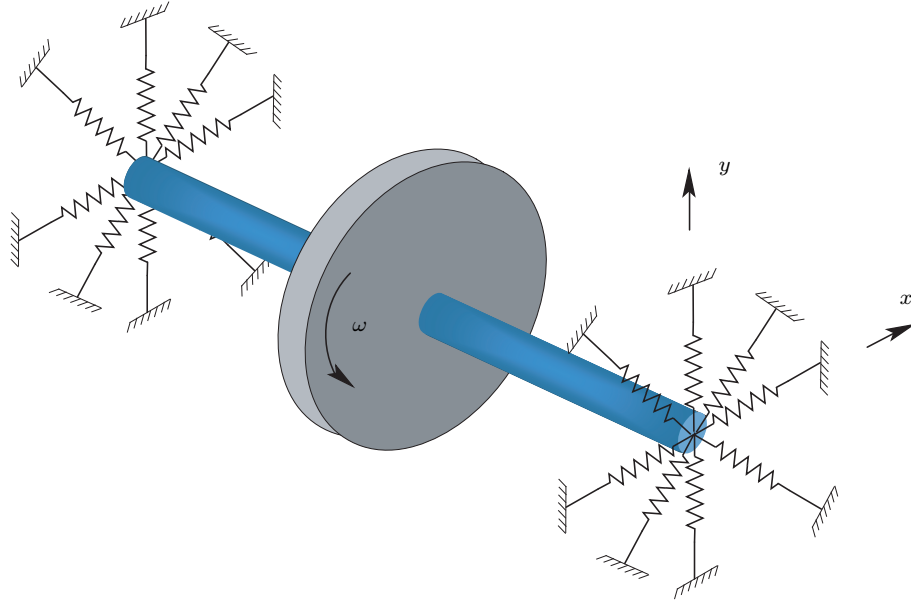


**Fig. 2.6** Linear model of the system

As a result, the nodal linearized bearing stiffness matrix for each end of the shaft is obtained in an explicit form as:

$$\mathbf{K}_{linear} = \begin{bmatrix} 4K & 2K & 0 & 0 \\ 2K & 4K & 0 & 0 \\ 0 & 0 & 0 & 0 \\ 0 & 0 & 0 & 0 \end{bmatrix} \quad (2.20)$$

For the linear model, the total stiffness matrix must include the stiffness matrix  $\mathbf{K}$  which is expressed in Eq. (2.4) and the nodal linearized bearing stiffness matrix  $\mathbf{K}_{linear}$  (Eq. (2.15))

at two ends of the shaft.

In general rotor dynamics modal analysis, natural frequencies and corresponding mode shapes must be entailed (Nelson and McVaugh, 1976). With finite element methods, most structures in rotor-bearing systems can be well modeled insofar as inertia and elastic characteristics are concerned. That is to say, mass and stiffness matrices adequate for rotor-bearing vibration modeling are often obtainable. However, the task of characterizing the system's damping properties is usually difficult, which relies more on experience and sometimes rough approximation (Adams, 1999). Hence, modal analysis usually makes use of the undamped model.

**Table 2.1** Natural frequencies of the system

Order	Natural Frequency (Hz)	Order	Natural Frequencies (Hz)
1	50	7	4809
2	251	8	4845
3	752	9	8220
4	788	10	8260
5	2323	11	12565
6	2344	12	12608

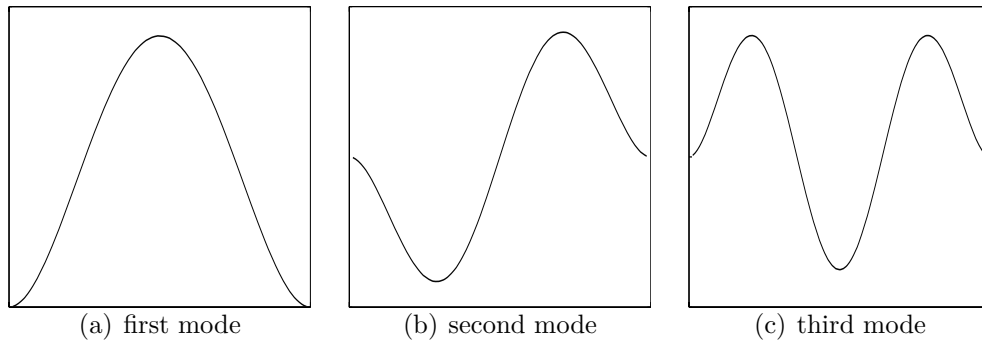


**Fig. 2.7** Mode shapes of the Jeffcott rotor

Through modal analysis, the first 12 natural frequencies of the system are listed in Table 2.1, the first three mode shapes of the system are shown in Fig. 2.7. Besides, through calculating the first 40 natural frequencies with respect to element numbers, the convergence of the finite element discretization is illustrated in Fig. 2.8. Based on the invariance of natural frequencies with respect to the mesh density, it is seen from the abscissa that the shaft can be divided into 20 elements.

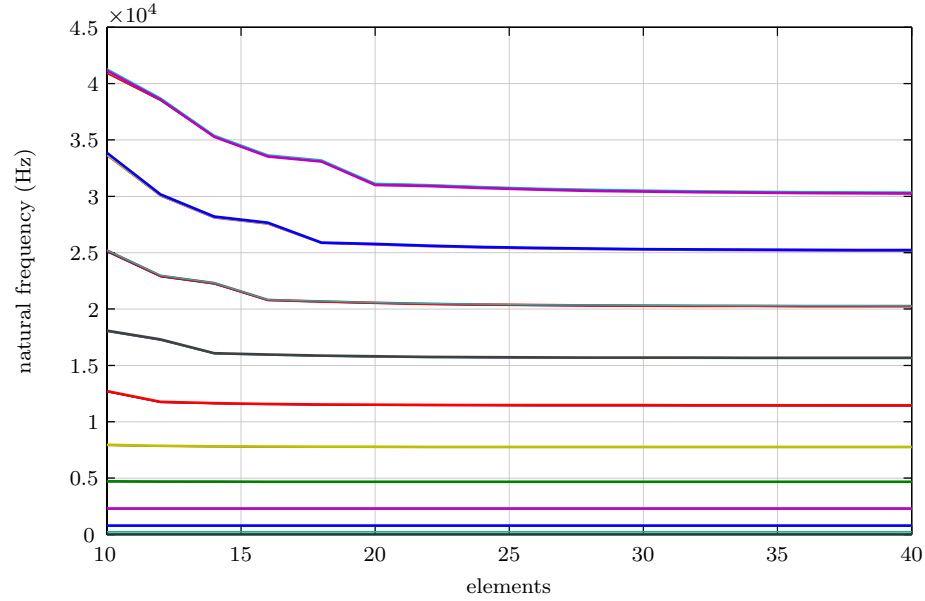


**Fig. 2.8** Convergence of finite element discretization

According to Meirovitch (2001), for an unforced multi-DOF linear rotor-bearing model, if damping is considered, the eigenvalues are more complicated than the case without damping. For rotor dynamic vibration analysis, focus is on machine operating conditions which lead to the dynamic instability, and this is related to complex eigenvalue problems (Adams, 1999).

For the case of the unforced linear system with damping, the governing equation is written as:

$$\mathbf{M}\ddot{\mathbf{q}} + \mathbf{D}\dot{\mathbf{q}} + \mathbf{K}\mathbf{q} = \mathbf{0} \quad (2.21)$$

where the damping matrix  $\mathbf{D}$  includes gyroscopic effects. For the complex modal analysis, the general approach is to transfer the second-order differential equation expressed in Eq. (2.21) into an equivalent set of first-order equations.

A velocity vector  $\mathbf{v}$  is introduced as:

$$\mathbf{v} = \dot{\mathbf{q}}, \quad \text{and} \quad \dot{\mathbf{v}} = \ddot{\mathbf{q}} \quad (2.22)$$

Rearranging the velocity and displacement vectors leads to:

$$\mathbf{z} = \begin{pmatrix} \mathbf{v} \\ \mathbf{q} \end{pmatrix}, \quad \text{and} \quad \dot{\mathbf{z}} = \begin{pmatrix} \dot{\mathbf{v}} \\ \dot{\mathbf{q}} \end{pmatrix} \quad (2.23)$$

Substituting Eq. (2.23) into Eq. (2.21) yields:

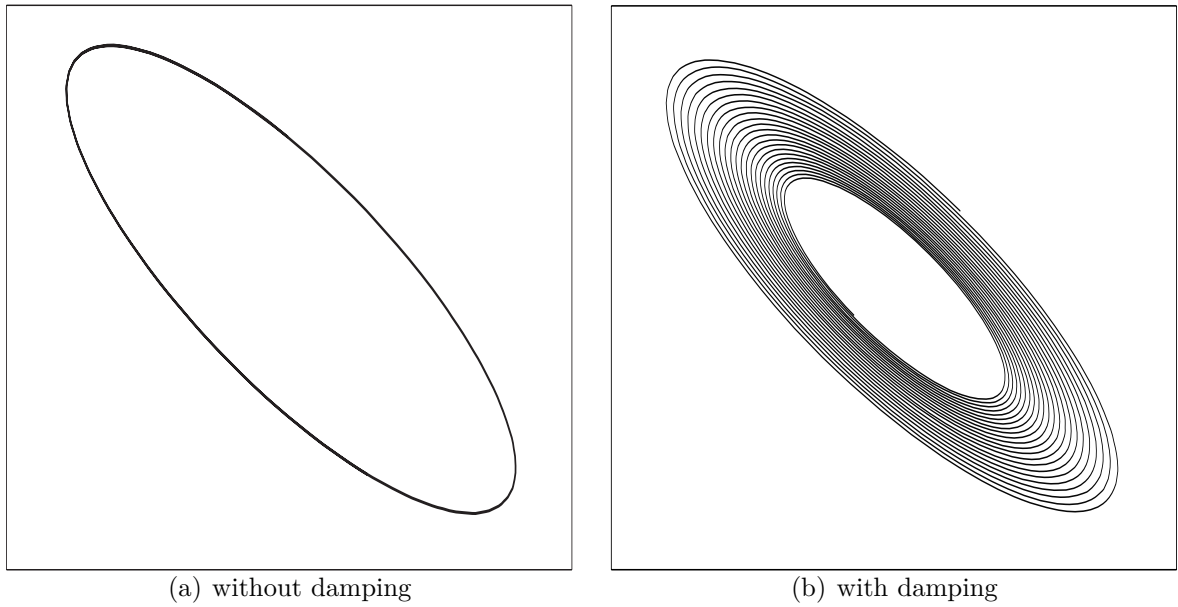


**Fig. 2.9** Orbit at shaft end 1 of the first linear mode

$$\begin{bmatrix} \mathbf{0} & \mathbf{M} \\ \mathbf{M} & \mathbf{D} \end{bmatrix} \dot{\mathbf{z}} + \begin{bmatrix} -\mathbf{M} & \mathbf{0} \\ \mathbf{0} & \mathbf{K} \end{bmatrix} \mathbf{z} = \mathbf{0} \quad (2.24)$$

Also, Eq. (2.24) can be written in a simple form, which is:

$$\dot{\mathbf{z}} + \mathbf{B}\mathbf{z} = \mathbf{0}, \quad \text{where} \quad \mathbf{B} = \begin{bmatrix} \mathbf{0} & \mathbf{M} \\ \mathbf{M} & \mathbf{D} \end{bmatrix}^{-1} \begin{bmatrix} -\mathbf{M} & \mathbf{0} \\ \mathbf{0} & \mathbf{K} \end{bmatrix} \quad (2.25)$$

Eq. (2.25) is the *state space* formulation of the system, which has solutions of the form as:

$$\mathbf{z} = \mathbf{Z}e^{\zeta t}, \quad \text{and} \quad \zeta = a \pm ib \quad (2.26)$$



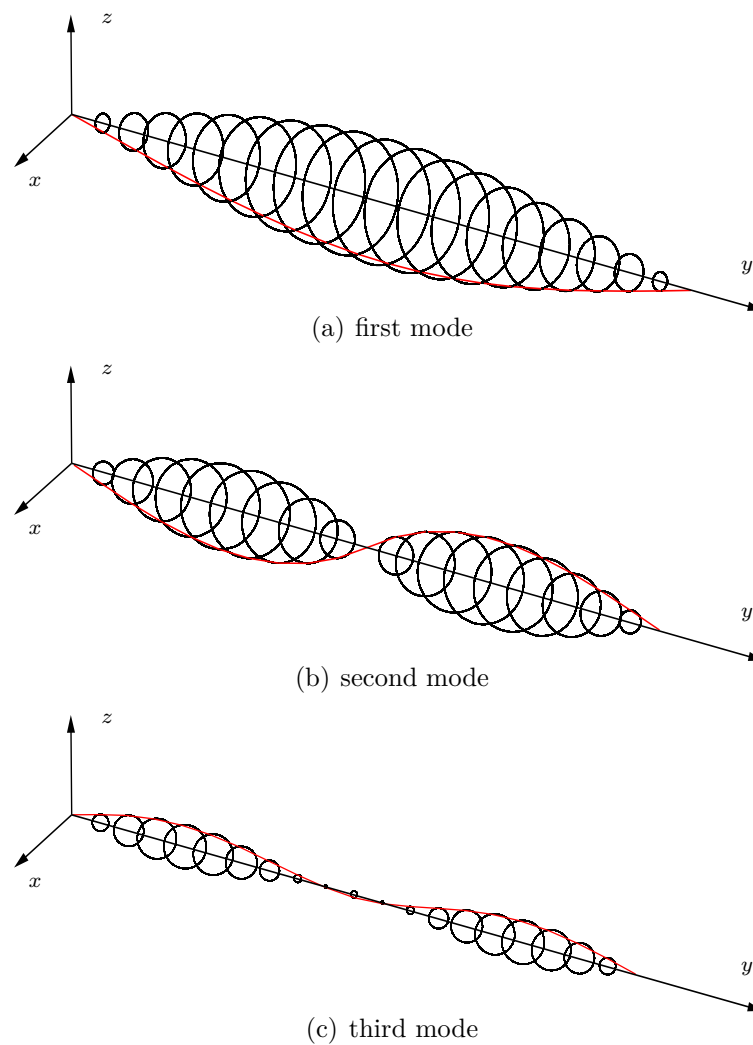


**Fig. 2.10** Linear modes of the system

obtained in terms of modal coordinates. The orbit at the shaft end 1 without and with damping through the transformation method are depicted in Figs. 2.9(a) and 2.9(b), respectively.

By means of the transformation method, the first three mode shapes of the system are illustrated in Fig. 2.10. The black circles represent the orbit of each node, and the red curve denotes the initial relative magnitude of all nodes.

According to Dimarogonas and Paipetis (1983), in rotordynamic systems, the natural frequency is relevant to rotation rates due to the induced gyroscopic effects. In rotordynamic analysis, the Campbell diagram is often employed to check for coincidence of

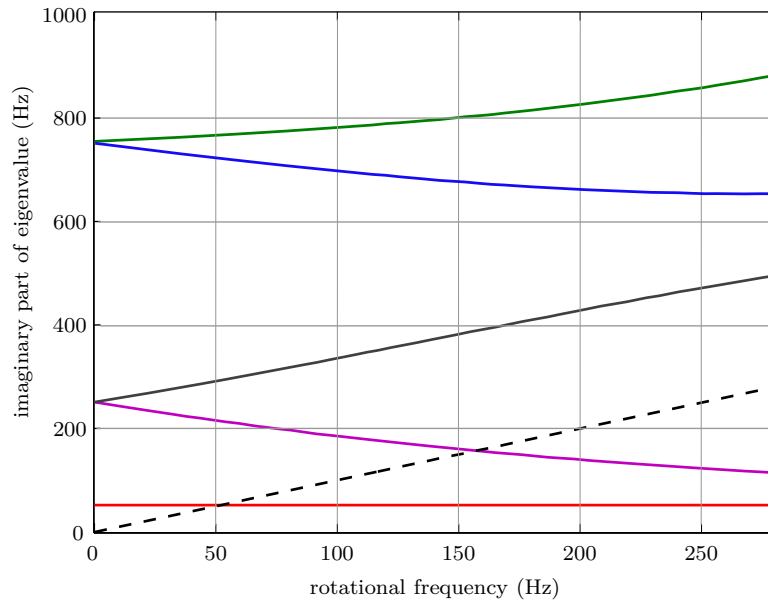


**Fig. 2.11** Campbell diagram

vibration sources with natural resonances. The Campbell diagram is a mathematically constructed diagram whose abscissa axis is the rotational frequency while the ordinate axis is natural frequency. In the Campbell diagram as shown in Fig. 2.11, the purple and blue curves represent the backward motion of the shaft, while the red, black and green curves illustrate the forward motion. The dashed line denotes the synchronous motion. It is apparent that the first forward critical speed is 50 Hz.

### 2.3 Modal Reduction: Craig-Bampton Method

Based on the full-order finite element model of the Jeffcott rotor, the simplest way to solve the dynamic equations is to use direct integration with iteration in time domain. However, this method is very computational expensive (Harris and Kotzalas, 2006a). In general, rotor-bearing systems usually have a very large number of DOFs while the nonlinear components are spatially localized. Although the nonlinear DOFs only constitute a small part of the whole system, the rotor-bearing system still behaves in a nonlinear fashion (Qu, 2002). In order to improve the computational efficiency, modal reduction techniques are proposed to reduce the system size.

Direct modal reduction of large mechanical systems can be used to reduce the number

of equations of motion by limiting the frequency content of the structure response in a narrow range (Guyan, 1965). Unfortunately, the direct access to physical quantities such as displacement will be lost then making the treatment of the unilateral contact conditions tedious. Accordingly, the chosen strategy is to select a component mode synthesis method that keeps a part of the displacement unknowns (where contact is anticipated and later called nonlinear DOFs) in the reduced-order model.

With its high modal accuracy and capability to reduce the size of dynamic systems, the Craig-Bampton modal reduction technique is chosen in this work. In this method, the whole DOFs are divided into boundary components and internal components (Craig and Bampton, 1968). Hence, partition of the stiffness matrix is denoted as:

$$\begin{pmatrix} \mathbf{F}_B \\ \mathbf{F}_I \end{pmatrix} = \begin{bmatrix} \mathbf{K}_{BB} & \mathbf{K}_{BI} \\ \mathbf{K}_{IB} & \mathbf{K}_{II} \end{bmatrix} \begin{pmatrix} \mathbf{q}_B \\ \mathbf{q}_I \end{pmatrix} \quad (2.32)$$

where the subscripts  $B$  and  $I$  denote boundary and internal DOFs,  $\mathbf{q}_B$  and  $\mathbf{q}_I$  are the boundary and internal displacement vectors. According to Craig and Bampton (1968), the constraint modes are defined as the mode shapes of the internal DOFs due to successive unit displacement of the boundary points, with all other boundary points totally constrained. Hence, the constraint modes are obtained by the assumption that forces add on the internal DOFs are equivalent to 0, i.e.,

$$[\mathbf{0}] = [\mathbf{K}_{IB}] [\mathbf{q}_B] + [\mathbf{K}_{II}] [\mathbf{q}_I] \quad (2.33)$$

Eq. (2.33) can be written in a simple form as:

$$[\mathbf{q}_I] = -[\mathbf{K}_{II}]^{-1} [\mathbf{K}_{IB}] [\mathbf{q}_B] = [\mathbf{\Phi}_c] [\mathbf{q}_B] \quad (2.34)$$

where  $[\mathbf{\Phi}_c]$  is the so-called matrix of constraint modes.

Similarly, the mass matrix is partitioned as:

$$[\bar{\mathbf{M}}] = \begin{bmatrix} \mathbf{M}_{BB} & \mathbf{M}_{BI} \\ \mathbf{M}_{IB} & \mathbf{M}_{II} \end{bmatrix} \quad (2.35)$$

The eigenvectors of the internal DOFs are the normal modes of the constraint substructure.

Therefore, the following equation is obtained:

$$\omega^2 [\mathbf{M}_{II}] [\phi_I] = [\mathbf{K}_{II}] [\phi_I] \quad (2.36)$$

in which each column of the eigenvector  $\phi_I$  forms the respective column of normal modes matrix  $\Phi_N$ . Let the reduction matrix be partitioned as:

$$[\Phi] = [\Phi_C \Phi_N] \quad (2.37)$$

Defining a set of modal coordinates  $\mathbf{u}$  which includes the constraint and fixed-interface modes of the system, and it is divided as:

$$\mathbf{u} = \begin{pmatrix} \mathbf{u}_\eta \\ \mathbf{u}_I \end{pmatrix} \quad (2.38)$$

where the subscript  $\eta$  refers to constraint modes.

With reference to Craig and Bampton (1968), the coordinate transformation matrix  $\Psi$  is written as:

$$\Psi = \begin{bmatrix} \mathbf{I} & \mathbf{0} \\ \Phi_c & \Phi_N \end{bmatrix} \quad (2.39)$$

It is apparent that the relationship between  $\mathbf{q}$  and  $\mathbf{u}$  is:

$$\mathbf{q} = \Psi \mathbf{u} \quad (2.40)$$

With  $[\Psi]$ , the mass, damping and stiffness matrices of the reduced-order model are denoted as:

$$[\tilde{\mathbf{M}}] = \Psi^T [\bar{\mathbf{M}}] \Psi, \quad [\tilde{\mathbf{K}}] = \Psi^T [\bar{\mathbf{K}}] \Psi \quad (2.41)$$

Also, the reduced-order proportional damping matrix  $[\tilde{\mathbf{D}}]$  is:

$$[\tilde{\mathbf{D}}] = \alpha [\tilde{\mathbf{M}}] + \beta [\tilde{\mathbf{K}}] \quad (2.42)$$

The responses obtained with the reduced-order and full-order model will be studied and compared in Chapter 4 for case studies.

## 2.4 Summary

In this chapter, the Jeffcott rotor model is introduced and investigated. As a mathematical approach to construct the model, the finite element method is adopted. Then, modal analysis is conducted to analyze the system's natural frequencies and mode shapes. Moreover, the convergence of finite element discretization is studied on the basis of invariance of natural frequencies with respect to the mesh density. Besides, the Campbell diagram is employed to study the critical speeds of the system. Finally, for the purpose of reducing computational efforts, the Craig-Bampton modal reduction method is also used. In next chapter, the supporting element (roller bearing) in the Jeffcott rotor system and its contact mechanics will be discussed.



## Chapter 3

# Roller Bearings and Contact Mechanics

### 3.1 Rolling Element Bearing Introduction

Rolling-element bearings are frequently used in aerospace applications with high precision positioning such as modern aircraft turbine engines (Harris, 2001). The main reason is that they can operate for sustained period of time when the normal lubrication supply fails, while journal bearings fail catastrophically if their lubrication supply is interrupted (Harris and Kotzalas, 2006b). Moreover, they are also known to achieve high stiffness and usually feature very low inherent damping capacity (Adams, 1999).

Rolling-element bearings are categorized as follows: ball bearings and roller bearings. Ball bearings can be subdivided into specific groups of *radial contact ball bearing*, *angular contact ball bearing*, and *axial contact ball bearing*. Roller bearings include categories as *cylindrical roller bearing*, *crowned cylindrical roller bearing*, and *tapered roller bearing* (Harris, 2001). Both ball and roller bearings are used in applications with high rotational speeds and act as stiff structural supports.

The main difference between roller and ball bearings lies in the load capacity and maximum speed limits (Harris and Kotzalas, 2006a). Roller bearings can support higher external loads because the support of the reaction contact forces is a *line* which reduces to a single *point* for ball bearings (Adams, 1999). In contrast to their high load capacity, at high speeds, the dynamic skewing of rollers will impose a maximum usable rotational

velocity for roller bearings. However, for ball bearings, the balls do not have the skewing problems at high speeds, thereby making the maximum allowable rotational velocity much higher.

Typical ball and roller bearings are illustrated in Figs. 3.1(a) and 3.1(b), respectively.

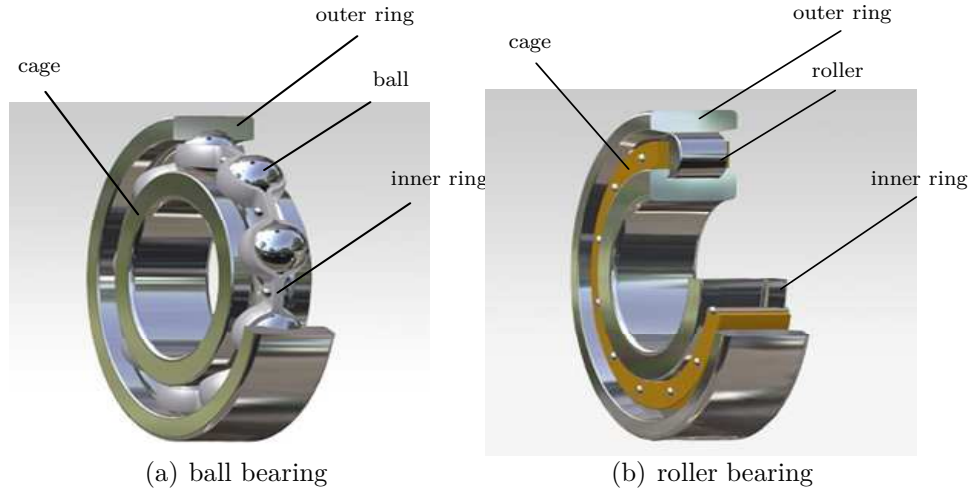
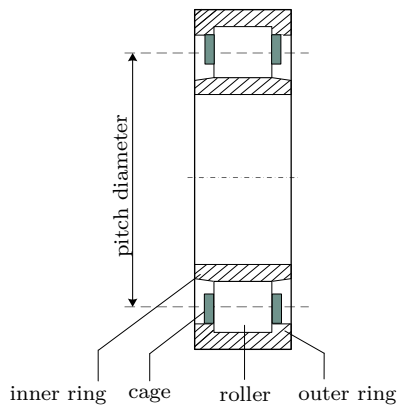


Fig. 3.1 Rolling element bearings (Palmgren, 1945)

In our study, the cylindrical roller bearing involves an initial configuration of eight rollers, in which the inner ring is rigidly fixed to the rotor and rotates at the same velocity, while the outer ring is rigidly fixed to a steady support. Fig. 3.2 shows a typical roller bearing model.



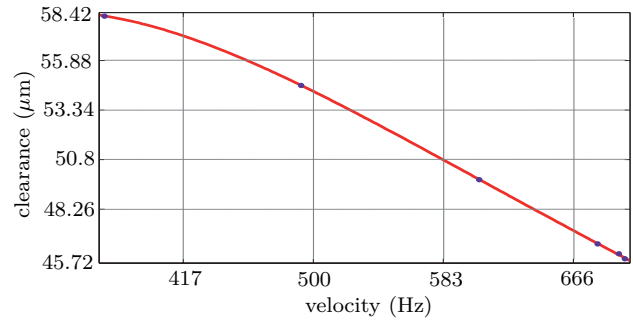
Components	Dimension	Value
inner ring	inner diameter	0.0559 m
	outer diameter	0.0665 m
outer ring	inner diameter	0.0787 m
	Outer diameter	0.0820 m
roller	length/height	0.0070 m
bearing	pitch diameter	0.0696 m
	internal radial clearance	10 $\mu\text{m}$ -120 $\mu\text{m}$
	speed range	1-750 Hz

Fig. 3.2 Roller bearing model and its geometry

### 3.2 Internal Radial Clearance and Bearing Contacts

In the past years, the *internal radial clearance* in roller bearings has drawn researchers' attentions due to its importance in subsequent nonlinear behaviors, in compensating thermal expansion and affecting the equivalent stiffness (Harsha, 2006a; Tiwari and Gupta, 2000). This internal radial clearance is the gap between rollers/balls and the outer ring. Usually, the internal radial clearance is independent of operating conditions. However, at very high speeds (above 350 Hz), the centrifugal forces acting on the rollers expand the internal radial clearance (Fleming et al., 2006). Moreover, at high speeds, the effects of oil-flow and thermal expansion on the internal radial clearance become significant (Harris, 2001). In the present study, experimental data of internal radial clearances with respect to rotational velocity  $\omega$  are provided by Pratt & Whitney (2008) and are depicted in Fig. 3.3.

$\omega$ (Hz)	clearance ( $\mu\text{m}$ )
366.18	58.17
492.20	54.61
606.36	49.78
682.26	46.48
695.83	45.97
699.92	45.72



**Fig. 3.3** Internal radial clearance with respect to rotational velocity (— fit; ● measurement points)

Similar to the procedure in the work of Fleming et al. (2006), the internal radial clearance  $\gamma_0$  with respect to rotational velocity is obtained using the curve fitting

$$\gamma_0 = a_0 + a_1\omega + a_2\omega^2 + a_3\omega^3 + a_4\omega^4 \quad (3.1)$$

where  $a_i$  ( $i = 0, \dots, 4$ ) are the fitted coefficients, which are listed in Table B.1 of Appendix B.

#### 3.2.1 Contact Solution Methods

There are a lot of interests in the modeling of unilateral contact in roller bearings. In fact, the physical modeling of the contact conditions is a complex task which depends on the

rotational velocity, contact geometry, materials of contact surface, internal radial clearance, etc (Harris and Kotzalas, 2006a). As illustrated in Fig. 3.4, when the radial displacement of the  $j^{\text{th}}$  roller is greater than the internal radial clearance, the roller participates in contacts with the outer ring.

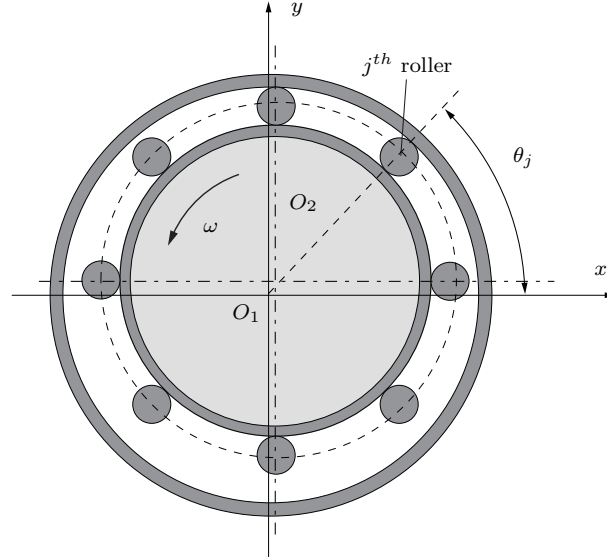


**Fig. 3.4** Bearing contact model (Harris and Kotzalas, 2006a)

Two approaches are widely used to handle the contacts in roller bearings: the Hertz theory and the Lagrange multipliers technique. The Hertz theory treats the contacts as external forces while the Lagrange multipliers technique handles the contacts as constraint conditions on the displacement field (Harsha, 2006a; Mijar and Arora, 2000).

### Hertz Theory

In the classical Hertz theory, the solution strategy involves an estimation of the contact forces as a function of the penetration depth of the rollers into the outer ring (Tiwari and Gupta, 2000). The penetration depth  $h_j$  of the  $j^{\text{th}}$  roller which contacts the outer ring is expressed as:

$$h_j = u_y \sin \theta_j + u_x \cos \theta_j - \gamma_0 \quad (3.2)$$

where  $u_y$  and  $u_x$  are the vertical and horizontal displacements of the rotor, and  $\theta_j$  is the angular position of the  $j^{\text{th}}$  roller at time  $t$ , which is expressed as (Tiwari and Gupta, 2000):

$$\theta_j = \frac{2\pi}{N_b} (j - 1) + \omega_c t \quad (3.3)$$

where  $N_b$  is the number of rollers, and  $\omega_c$  is the cage velocity, which is:

$$\omega_c = \left(1 - \frac{D_b}{D_p}\right) \frac{\omega}{2} \quad (3.4)$$

where  $D_b$  is the roller diameter, and  $D_p$  is the pitch diameter.

Hence, the contact force is estimated as follows (Harris and Kotzalas, 2006a):

$$\mathbf{F}_{\text{NL}} = \begin{cases} Kh_j^{1.11} + C\dot{h}_j, & \text{if } h_j \geq 0 \\ 0, & \text{if } h_j < 0 \end{cases} \quad (3.5)$$

in which  $C$  is the contact damping coefficient,  $K$  is the overall contact stiffness coefficient and is expressed as (Leontiev et al., 2007):

$$K = \left( \frac{1}{\frac{1}{K_i^{2/3}} + \frac{1}{K_o^{2/3}}} \right) \quad (3.6)$$

where  $K_i$  and  $K_o$  are the elastic stiffness coefficients of the inner ring and outer ring, respectively.

Based on the Hertz theory, the system responses and contact forces through time-marching technique will be investigated in Chapter 4.

### Lagrange Multipliers Technique

The classical Hertz theory is commonly employed to handle bearing contacts. Unfortunately, the estimation of the contact stiffness/damping coefficients and the penetration depth is very difficult in some specific working conditions (Harris, 2001). Another approach which is based on the Lagrange multipliers technique is developed to handle the contacts. This Lagrange multipliers approach avoids direct modeling of the contact forces and its respective limitations such as, for instance, a residual penetration between the contact

components. In the Lagrange multipliers technique, the contacts are treated as constraints on the displacement and are automatically calculated at each time step (Mijar and Arora, 2000).

For the Jeffcott rotor model, the rotor is supported by the nonlinear contact forces in roller bearings at its ends and its motion is constrained by the non-penetration conditions for each roller bearing as:

$$\begin{aligned} h_{1j} &= u_{y1} \sin \theta_j + u_{x1} \cos \theta_j - \gamma_0 \leq 0 \\ h_{2j} &= u_{y2} \sin \theta_j + u_{x1} \cos \theta_j - \gamma_0 \leq 0 \end{aligned} \quad (3.7)$$

where  $u_{y1}$ ,  $u_{x1}$  and  $u_{y2}$ ,  $u_{x2}$  are the vertical and horizontal displacements of the rotor at each bearing location, respectively.

By incorporating Eq. (3.7) into Eq. (2.4), we obtain (Sahinkaya et al., 2007):

$$\mathbf{M}\ddot{\mathbf{q}} + \mathbf{J}^T \boldsymbol{\lambda} + \mathbf{D}\dot{\mathbf{q}} + \mathbf{K}\mathbf{q} = \mathbf{F} \quad (3.8)$$

where  $\mathbf{F}$  is the external force vector, which includes unbalanced forces and gravity. The Lagrange multipliers vector  $\boldsymbol{\lambda}$ , which physically stores the restoring contact forces, is written as:

$$\boldsymbol{\lambda} = \left( \lambda_{1_1} \quad \lambda_{1_2} \quad \dots \quad \lambda_{1_{N_b}} \quad \lambda_{2_1} \quad \lambda_{2_2} \quad \dots \quad \lambda_{2_{N_b}} \right)^T \quad (3.9)$$

where  $\lambda_{1_j}$  and  $\lambda_{2_j}$  ( $j = 1, \dots, N_b$ ) stand for the Lagrange multipliers arising from the  $j^{\text{th}}$  constraint conditions (Eq. (3.7)) at each roller bearing, respectively. In Eq. (3.8),  $\mathbf{J}$  is the contact matrix (Jacobian matrix) whose  $j^{\text{th}}$  row is the partial derivative of the  $j^{\text{th}}$  constraint equation with respect to the generalized coordinates. The number of constraint equations is obviously equivalent to the number of rollers. Hence, the contact matrix is

expressed as:

$$\mathbf{J} = \begin{bmatrix} \sin \theta_1 & \cos \theta_1 & 0 & 0 & \dots & 0 & 0 & 0 & 0 \\ \sin \theta_2 & \cos \theta_2 & 0 & 0 & \dots & 0 & 0 & 0 & 0 \\ \vdots & & & & & & & & \vdots \\ \sin \theta_{N_b} & \cos \theta_{N_b} & 0 & \dots & 0 & 0 & 0 & 0 & 0 \\ 0 & 0 & 0 & \dots & 0 & \sin \theta_1 & \cos \theta_1 & 0 & 0 \\ 0 & 0 & 0 & \dots & 0 & \sin \theta_2 & \cos \theta_2 & 0 & 0 \\ \vdots & & & & & & & & \vdots \\ 0 & 0 & 0 & \dots & 0 & \sin \theta_{N_b} & \cos \theta_{N_b} & 0 & 0 \end{bmatrix} \quad (3.10)$$

which yields the nonlinear force vector as:

$$\mathbf{F}_{NL} = -\mathbf{J}^T \lambda \quad (3.11)$$

The contact forces should be negative during each contact period to maintain the motion of rotor on the inner surface of the outer ring. If a penetration is detected, the displacement of the rotor has to be corrected in such a way that the non-penetration conditions (Eq. (3.7)) are satisfied. The process of Lagrange multipliers technique is illustrated in Fig. 3.5. It is worth nothing that within a rigid body framework, the Lagrange multipliers may lead to mathematical constraints since no residual penetration is allowed between the contacting components. It is more appropriate to use this technique with flexible structures. Moreover, it yields the definition of an extra unknown, namely the contact force.

The system responses with the Lagrange multipliers technique through time-marching technique will be investigated in Chapter 4.

### 3.2.2 Forcing Functions

In some industrial applications, it is of great interest to engineers to relate bearing radial contact forces and deflections with rotational velocity (Pratt & Whitney, 2008). In such situations, for a specific operating condition, the focus is on constructing a direct relationship between bearing contact forces, rotor's displacements at the bearing location and the rotational velocity. This process can be accomplished with the framework of Hertz contact theory. Based on the Hertz theory, the contact forces are calculated for several

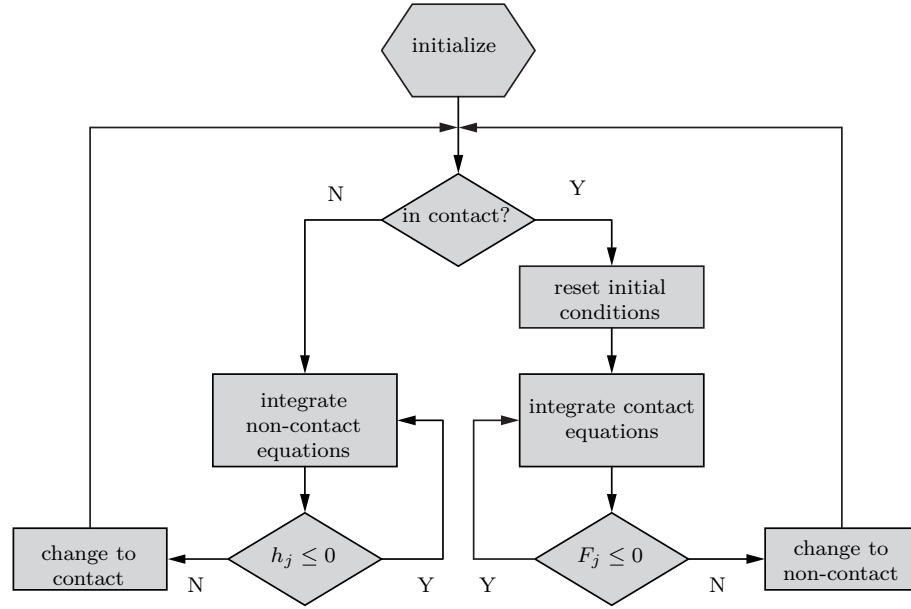


**Fig. 3.5** Flowchart of the Lagrange multipliers technique

rotational velocities. Then, according to Fleming and Poplawski (2005), forcing functions are extracted with respect to rotational velocity through curve fitting. Therefore, the forcing function is sought as:

$$\mathbf{F}_{\text{NL}} = (a_0 + a_1\omega) (u_r - \gamma_0)_+^{(b_0 + b_1\omega)} \quad (3.12)$$

where  $\mathbf{F}_{\text{NL}}$  is the nonlinear bearing contact force,  $u_r$  is the radial displacement of the rotor at the bearing location,  $a_i$  and  $b_i$  ( $i = 0, 1$ ) are the fitting coefficients. The subscript “+” in Eq. (3.12) denotes a piecewise function, which means that this equation is adopted only if the bearing deflection is greater than the internal radial clearance.

In our analysis, the cases of mass eccentricities of  $4 \times 10^{-5}$  m and  $2 \times 10^{-5}$  m applied on the disk are included in the forcing functions extraction. The responses obtained through the forcing functions will be illustrated in Chapter 4. The curve fitting coefficients in Eq. (3.12) are listed in Table B.2 of Appendix B.

### 3.3 Roller Rotation and Ring Waviness

With the rapid development of high-speed rotating machines, the roller rotation (bending/skewing) has drawn more attentions recently (Wang et al., 2007). However, in order to simplify the bearing model, many works adopt assumptions such as neglecting roller rotation and ring waviness (Tiwari and Gupta, 2000). Under complex loading conditions, this simplified model may be too limited. In this section, the roller rotation and ring waviness are studied within the framework of Hertz contact theory.

The bearing model with roller rotation is illustrated in Fig. 3.6, in which  $r_j$  is the radial displacement of the  $j^{\text{th}}$  roller,  $\beta_j$  and  $\alpha_j$  are the declining and skewing angles, respectively. The rollers decline under the bending moment  $M_x$ , and simultaneously skew under the skewing moment  $M_y$ . In cylindrical roller bearings, rollers are not perfectly cylindrical, but with round corners at each end (Pratt & Whitney, 2008). For computational accuracy, the round corners are divided into many pieces. As illustrated in Fig. 3.6, let  $l_e$  be the length

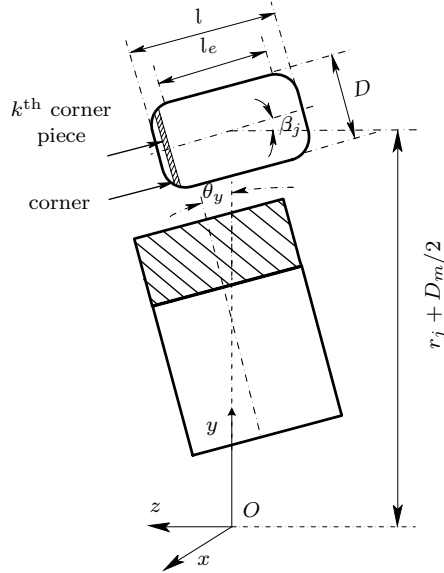


**Fig. 3.6** Roller rotation

of linear part of each roller, and  $l$  be the total length, the position of the  $k^{\text{th}}$  round piece along the abscissa axis is expressed as (Wang et al., 2007):

$$z_k = -\frac{l_e}{2} + (k-1)w \quad (3.13)$$

where  $w$  is the thickness of the roller. The moments  $M_x$  and  $M_y$  will cause additional deformation of the  $k^{\text{th}}$  round piece of the corner which stays in contact with the outer ring. Hence, the bending deformation of the  $k^{\text{th}}$  corner piece for the  $j^{\text{th}}$  roller is:

$$h_{jk\beta} = \left[ z_k + \frac{D_2}{2} \tan \left( \frac{\theta_y \cos \theta_j}{2} \right) \right] \tan \beta_j \quad (3.14)$$

where  $D_2$  is the average diameter of the outer surface of inner ring, and  $\theta_y \cong \beta_j$ . Therefore, the total bending deformation of the  $j^{\text{th}}$  roller is expressed as:

$$h_{j\beta} = \sum_{k=1}^{\infty} h_{jk\beta} \quad (3.15)$$

Similarly, the skewing deformation of the  $k^{\text{th}}$  corner piece is:

$$h_{jk\alpha} = \left[ \frac{D_1^2}{2} - (z_k \sin(\theta_z \sin \theta_j) - \alpha_j)^2 \right]^{0.5} - \frac{D_1}{2} \quad (3.16)$$

where  $D_1$  is the average diameter of the inner surface of outer ring, and  $\theta_z \cong \alpha_j$ . Then

$$h_{j\alpha} = \sum_{k=1}^{\infty} h_{jk\alpha} \quad (3.17)$$

In general, ring waviness is common in roller bearings. Waviness is used to describe the ring's local defects and can be an important source of the system's nonlinear vibration. Following Bai and Xu (2006), the waviness is described by a superposition of sinusoidal functions. For the  $j^{\text{th}}$  roller, the outer ring and inner ring waviness are:

$$\begin{aligned} P_o(j) &= \sum_{n=1}^{\infty} A_{1n} \cos \left[ n(\omega_c - \omega_1)t + \frac{2\pi j}{N_b} + \xi_{1n} \right] \\ P_i(j) &= \sum_{n=1}^{\infty} A_{2n} \cos \left[ n(\omega_c - \omega_2)t + \frac{2\pi j}{N_b} + \xi_{2n} \right] \end{aligned} \quad (3.18)$$

where  $n$  is the waviness order,  $A_{1n}$  and  $A_{2n}$  are the maximum amplitudes of the waviness in the radial direction of the outer and inner ring,  $\xi_{1n}$  and  $\xi_{2n}$  are the initial phase angles of the outer and inner ring waviness, and  $\omega_1$  and  $\omega_2$  are the rotational velocities of the outer and inner ring (in this work,  $A_{1n} = A_{2n} = 1 \mu\text{m}$ ,  $\omega_1 = 0$ ,  $\omega_2 = \omega$ ).

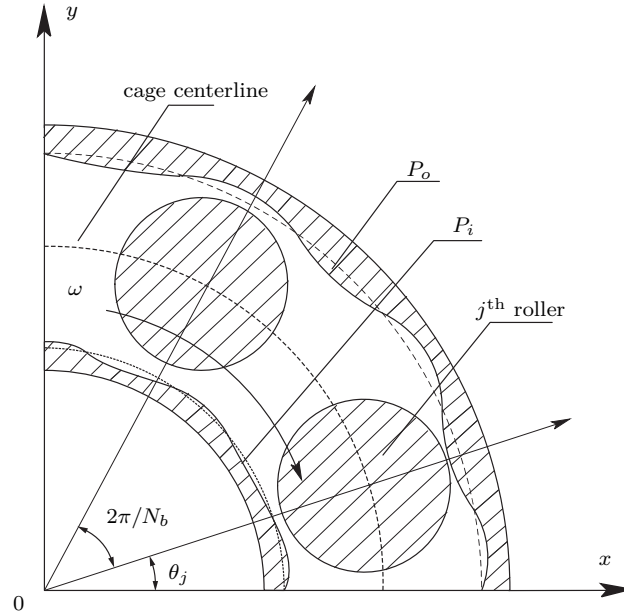


**Fig. 3.7** Ring waviness

Therefore, due to additional deformation of roller rotation and ring waviness, the elastic penetration of the  $j^{\text{th}}$  roller which stays in contact with the outer ring is represented by:

$$h_j = u_x \cos \theta_j + u_y \sin \theta_j - \gamma_0 + h_{j\beta} + h_{j\alpha} - P_o(j) - P_i(j) \quad (3.19)$$

From Eq. (3.5), the contact force for the  $j^{\text{th}}$  roller can be deduced from the Hertz contact theory. With roller rotation and ring waviness, the time responses and frequency responses of the rotor will be studied in Chapter 4 in details.

### 3.4 Roller Bearing Stiffness

On the basis of the Hertz contact theory, the equivalent stiffness of roller bearings are studied. The equivalent stiffness (or effective stiffness) is a common design parameter for roller bearing analysis (Harris and Kotzalas, 2006a). It depends on the number of rollers, the internal radial clearance, materials of contact surface, the contact angle and preloads (Harris, 2001). According to Lim and Singh (1989), the linearization method is often used to obtain the equivalent stiffness. This linearization method is strongly related to the Hertz theory and the equivalent stiffness is estimated through a linearization of the

contact forces with respect to displacements.

Following the Hertz theory, the contact forces of the  $j^{\text{th}}$  roller in the horizontal and vertical directions are expressed as:

$$\begin{pmatrix} F_y \\ F_x \end{pmatrix} = K \sum_{j=1}^{N_b} (u_x \cos \theta_j + u_y \sin \theta_j - \gamma_0)_+^{1.11} \begin{pmatrix} \sin \theta_j \\ \cos \theta_j \end{pmatrix} \quad (3.20)$$

Hence, the radial contact force for the  $j^{\text{th}}$  is:

$$F_r = \sqrt{F_x^2 + F_y^2} \quad (3.21)$$

According to Lim and Singh (1989), the lateral and angular displacements do not interact with each other. The bearing's equivalent stiffness matrix is written as:

$$[\mathbf{K}_e] = \begin{bmatrix} [\mathbf{K}_e]_{trans} & \mathbf{0} \\ \mathbf{0} & [\mathbf{K}_e]_{angular} \end{bmatrix} \quad (3.22)$$

where  $[\mathbf{K}_e]_{trans}$  and  $[\mathbf{K}_e]_{angular}$  are translational and angular stiffness matrices. For cylindrical roller bearings, the angular stiffness is often ignored, and only the translational stiffness matrix is taken into consideration, which is:

$$[\mathbf{K}_e]_{trans} = \begin{bmatrix} [K]_{u_y u_y} & [K]_{u_y u_x} \\ [K]_{u_x u_y} & [K]_{u_x u_x} \end{bmatrix} \quad (3.23)$$

For the horizontal and vertical contact forces  $F_x$  and  $F_y$ , the components of the stiffness matrix are expressed as the linearization of the contact forces over the rotor's displacements. Consequently, the stiffness matrix is expressed as:

$$[\mathbf{K}_e]_{trans} = \begin{bmatrix} \partial F_y / \partial u_y & \partial F_y / \partial u_x \\ \partial F_x / \partial u_y & \partial F_x / \partial u_x \end{bmatrix} \quad (3.24)$$

Following Tamura et al. (1985), we obtain:

$$\begin{pmatrix} \partial F_y / \partial u_y \\ \partial F_x / \partial u_x \\ \partial F_y / \partial u_x \\ \partial F_x / \partial u_y \end{pmatrix} = 1.11K \sum_{j=1}^{N_b} (u_x \cos \theta_j + u_y \sin \theta_j - \gamma_0)_+^{0.11} \begin{pmatrix} \sin^2 \theta_j \\ \cos^2 \theta_j \\ \cos \theta_j \sin \theta_j \\ \sin \theta_j \cos \theta_j \end{pmatrix} \quad (3.25)$$

From Eq. (3.25), it is noticeable that the horizontal and vertical stiffness are displacement-dependent. In general, the fluctuating parts of  $u_x$  and  $u_y$  are very small compared to the mean value of  $u_x$  and  $u_y$ . Moreover, the fluctuating parts of  $\partial F_x / \partial u_x$  and  $\partial F_y / \partial u_y$  are also small in comparison with the mean value of  $\partial F_x / \partial u_x$  and  $\partial F_y / \partial u_y$  (Tamura et al., 1985). Also, according to Eq. (3.25), it is apparent that  $\partial F_x / \partial u_y = \partial F_y / \partial u_x$ .

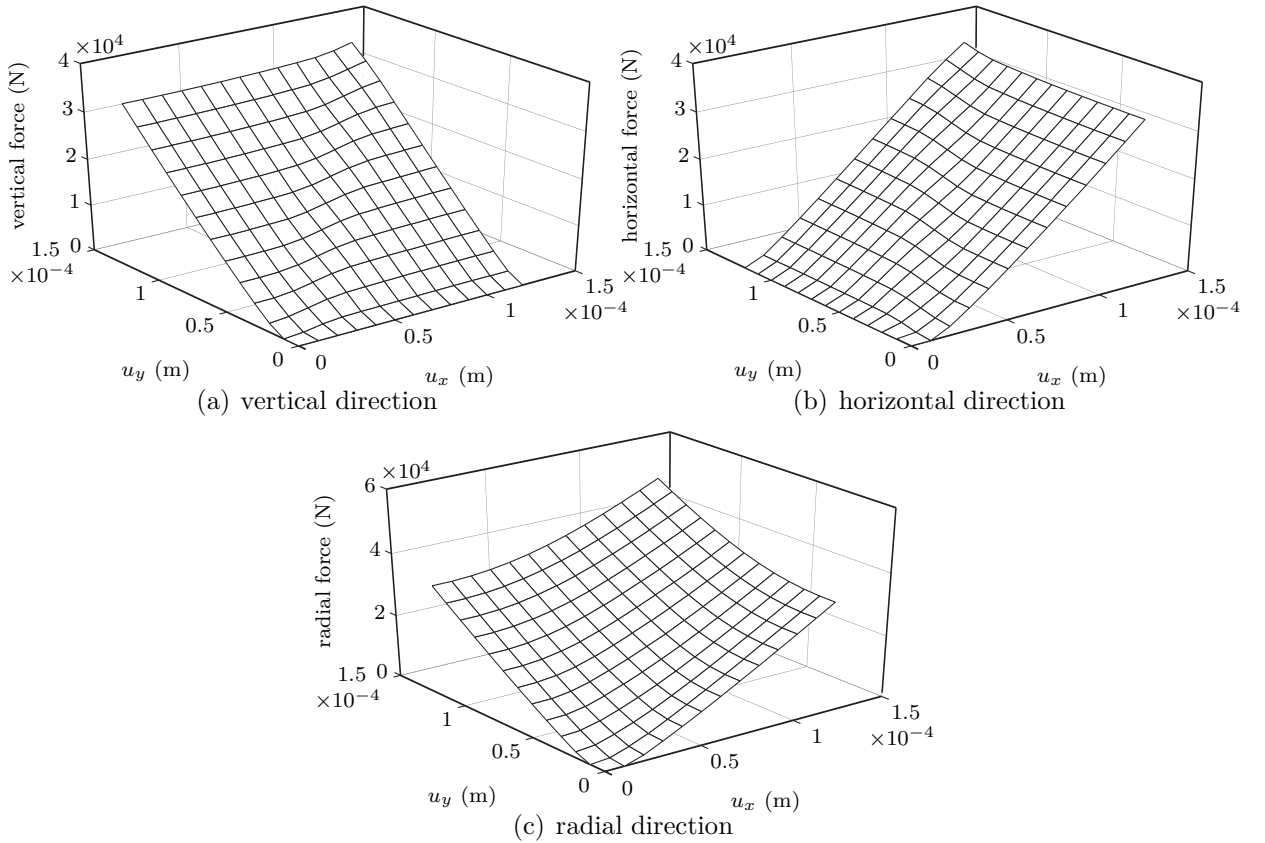


**Fig. 3.8** Force-deflection surface under radial clearance of  $10 \mu\text{m}$

Following Eq. (3.20) and Eq. (3.21), the horizontal, vertical and radial contact force

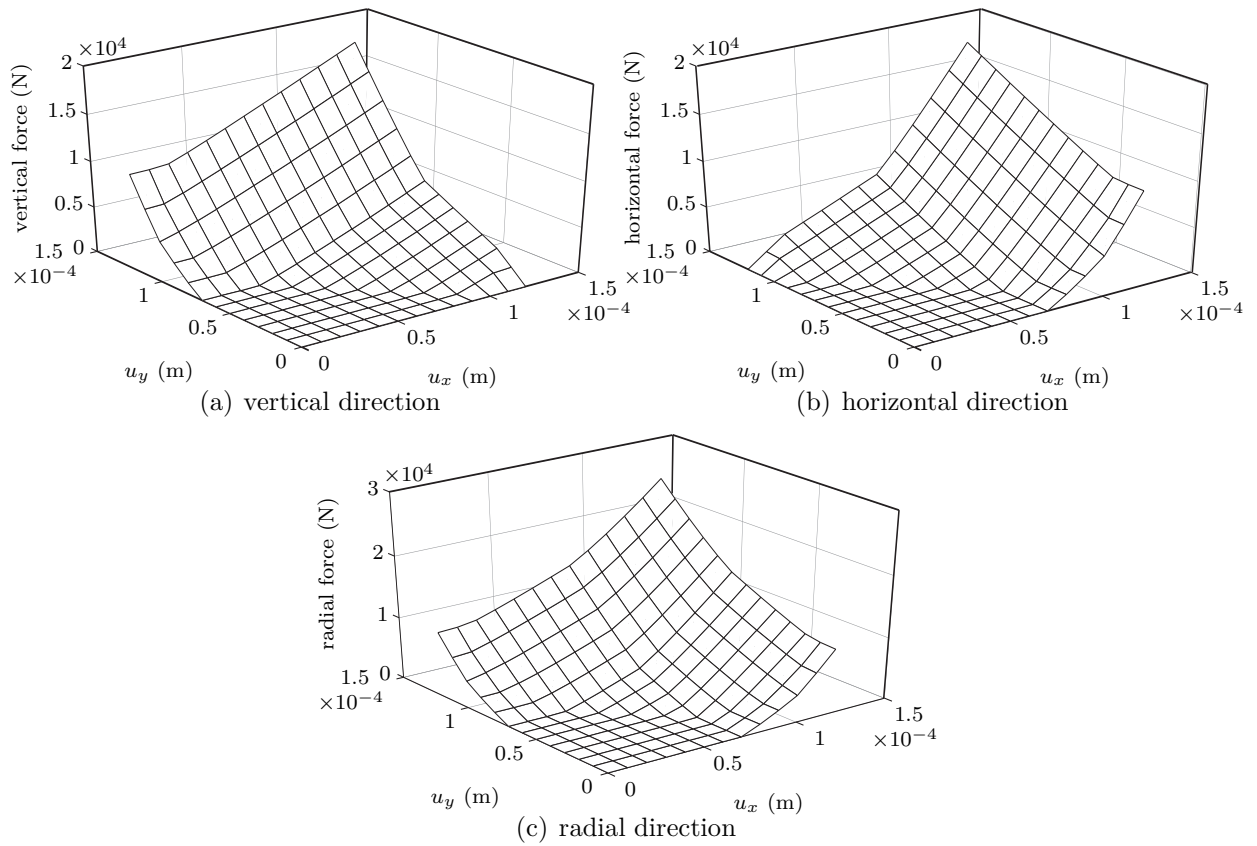


**Fig. 3.9** Force-deflection surface under radial clearance of  $60 \mu\text{m}$

surfaces with respect to displacements are plotted. Under internal clearance of  $10 \mu\text{m}$ , the vertical and horizontal contact force surfaces are shown in Figs. 3.8(a) and 3.8(b), respectively. Also, the radial contact force surface is depicted in Fig. 3.8(c). It is apparent that for the vertical case, when  $u_y > 10 \mu\text{m}$ , the contact force obeys a linear relationship with the vertical displacement. Similar conclusions can be drawn for the horizontal and radial cases.

When the internal radial clearance is increased to  $60 \mu\text{m}$ , the contact force surfaces are shown in Fig. 3.9. With the increase of internal clearance, both horizontal and vertical contact forces are linear with displacements in the corresponding directions when  $u_x > 60 \mu\text{m}$  or  $u_y > 60 \mu\text{m}$ . In comparison with the case of radial clearance of  $10 \mu\text{m}$ , the zero force zone expands due to the increase of internal clearance. Another phenomenon is that both the maximum horizontal and vertical contact forces decrease. Moreover, the maximum radial contact force is larger than the horizontal and vertical contact forces under

both internal clearances. This is always true in roller bearing analysis (Tiwari and Gupta, 2000).

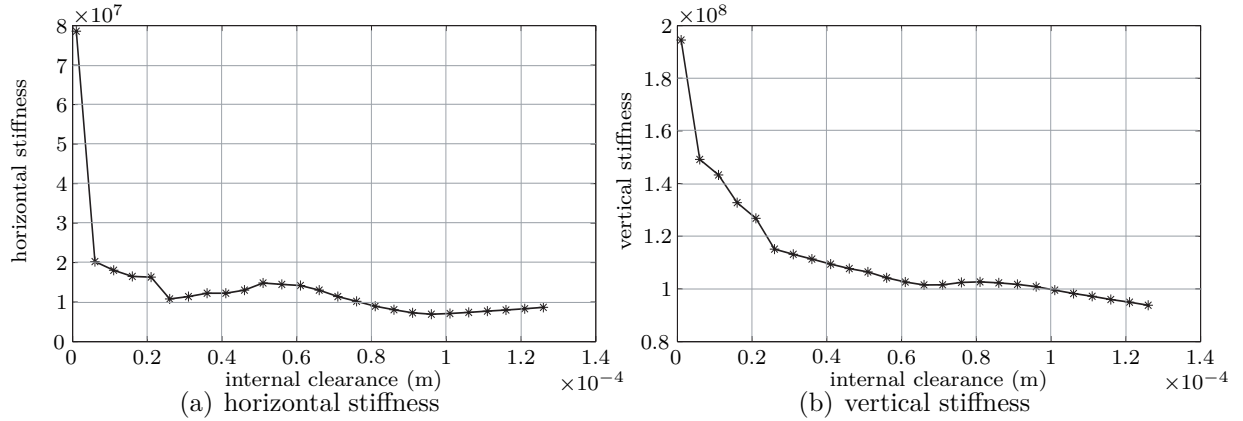


**Fig. 3.10** Bearing stiffness with respect to the internal radial clearance

Prediction of bearing equivalent stiffness with respect to the internal radial clearance is an important expectation in this project (Pratt & Whitney, 2008). Following Eq. (3.25), the equivalent stiffness is calculated in terms of displacements for each internal radial clearance.

The equivalent horizontal and vertical stiffness with respect to the internal radial clearance are illustrated in Figs. 3.10(a) and 3.10(b), respectively. It is noticeable to see that under small clearance, both the horizontal and vertical stiffness are large. However, with slight increase of clearance, both of them decrease quickly, and the horizontal stiffness decreases even faster. Further increase of clearance plays a much less significant role in decreasing the stiffness. Both the horizontal and vertical stiffness remain practically constant till the internal clearance reaches a certain value (for the horizontal case,  $\gamma_0 = 30 \mu\text{m}$ ; for the vertical case,  $\gamma_0 = 60 \mu\text{m}$ ). For the same clearance, the vertical stiffness is larger than its horizontal counterpart. Besides, the coupling stiffness is independent of the internal radial clearance; therefore, the coupling stiffness with respect to the internal clearance is not illustrated.

In general, the equivalent stiffness prediction is based on three assumptions:

- For cylindrical roller bearings, the angular stiffness is ignored.
- The roller bearing is assumed to be free of axial load, so the axial stiffness is not included in our analysis.

- At high speeds, effects of rollers' centrifugal forces and ring flexibility become significant, and more complex stiffness analysis will be included in the future work.

In rotordynamic analysis, the natural frequencies of the system are related to the bearing stiffness (Villa et al., 2005). Hence, they are dependent of the internal radial clearance in supporting roller bearings. Furthermore, the onset of the non-synchronous vibration is controlled by the natural frequencies of the system (Jing et al., 2004). Therefore, the investigation of the equivalent stiffness is significant in understanding the non-synchronous vibration. The relationship of system's natural frequencies with respect to the internal clearance will be studied by means of nonlinear normal modes in the future work.

### **3.5 Summary**

The contact in the cylindrical roller bearing is introduced in this chapter. Three approaches are proposed to study the bearing contact forces: the Hertz contact theory, the Lagrange multipliers technique and the forcing functions. Moreover, the roller rotation and ring waviness are also introduced. Due to the fact that the natural frequency of the rotor-bearing system is relevant to the bearing stiffness, a linearization method is proposed to calculate the bearing stiffness with respect to the internal radial clearance. All these concepts will be used in Chapter 4 for sensitivity studies.

# Chapter 4

## Numerical Methods

Several numerical methods are available to solve the second-order ordinary differential equations. In general, for rotor-bearing systems, the time-marching technique and harmonic balance method are often employed to solve the equations of motion. In this chapter, both of them will be adopted to investigate the system's nonlinear behaviors.

### 4.1 Time-marching Technique

In the time-marching technique, we start with an initial guess and march the equations in time domain while applying for boundary conditions (Qin et al., 2004). This procedure gives a mathematically *hyperbolic* characteristic, i.e., the solution at each time step is dependent on the solutions at previous time steps (White and Young, 1993). In the time-marching technique, several numerical tools are widely used, such as Runge-Kutta method, Wilson- $\theta$  algorithm and Newmark- $\beta$  method.

Among these numerical tools, the explicit Newmark- $\beta$  integration method is often chosen because it is a robust numerical tool to solve the equations of motion for large order systems. The procedure of this method is explained as following:

- In the explicit Newmark- $\beta$  method, both the acceleration vector  $\ddot{\mathbf{q}}$  and velocity vector  $\dot{\mathbf{q}}$  are represented in terms of the displacement vector  $\mathbf{q}$ . At the  $n^{\text{th}}$  time step, they are expressed as:

$$\begin{aligned}\ddot{\mathbf{q}}_n &= \frac{1}{h^2} (\mathbf{q}_{n-1} - 2\mathbf{q}_n + \mathbf{q}_{n+1}) \\ \dot{\mathbf{q}}_n &= \frac{1}{2h} (-\mathbf{q}_{n-1} + \mathbf{q}_{n+1})\end{aligned}\tag{4.1}$$

where  $h$  is the time step size, and  $\mathbf{q}_{-1}$  is expressed as:

$$\mathbf{q}_{-1} = \mathbf{q}_0 - h\dot{\mathbf{q}}_0 + \frac{h^2}{2}\ddot{\mathbf{q}}_0 \quad (4.2)$$

- Then, substituting Eq. (4.1) into the system governing equation Eq. (2.4) yields:

$$\left(\frac{1}{h^2}\mathbf{M} + \frac{1}{2h}\mathbf{D}\right)\mathbf{q}_{n+1} = \mathbf{F}_{LNn} + \mathbf{F}_{NLn} - \left(\mathbf{K} - \frac{2}{h^2}\mathbf{M}\right)\mathbf{q}_n - \left(\frac{1}{h^2}\mathbf{M} - \frac{1}{2h}\mathbf{D}\right)\mathbf{q}_{n-1} \quad (4.3)$$

Through this way, the displacement vector is calculated at each time step. Then, from Eq. (4.1), the acceleration and velocity vectors can be obtained.

#### 4.1.1 Time Step Size Convergence

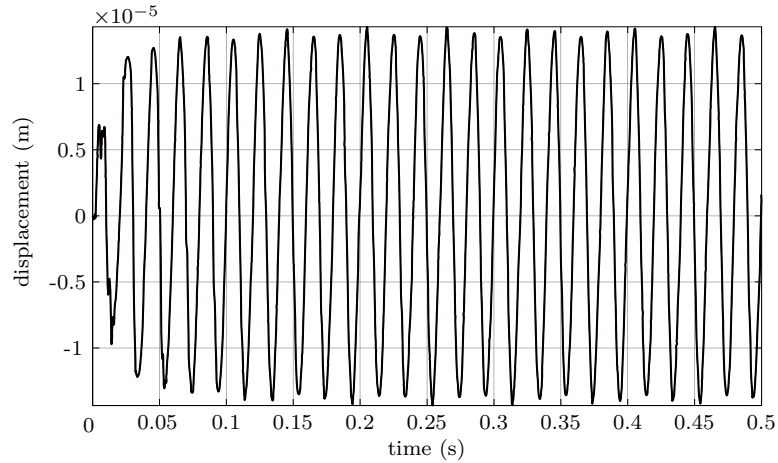


**Fig. 4.1** Time step size convergence (—  $h = 10^{-5}$  s; —  $h = 10^{-6}$  s; —  $h = 10^{-7}$  s)

For nonlinear ordinary equations, the time step size plays significant roles for the convergence of responses. Generally, the smaller the step size, the longer the solution is obtained; the larger the step size, the shorter the computation time will be. With the time step  $h = 10^{-4}$  s, the time responses diverge. As illustrated in Fig. 4.1,  $h = 10^{-5}$  s is chosen on the basis of the criteria of convergence and inexpensive computation. For the initial conditions, the displacement, velocity and acceleration vectors are all set as  $\mathbf{0}$ .

### 4.1.2 Runge-Kutta and Newmark- $\beta$ Method

It is noticeable that besides the explicit Newmark- $\beta$  method, the Runge-Kutta method is also commonly used to solve second-order ordinary differential equations. However, in comparison with the explicit Newmark- $\beta$  method, the Runge-Kutta method is computationally expensive. A summarization of the two numerical methods is listed in Table 4.1, and the responses are compared in Fig. 4.2. It is apparent that the responses do good jobs of

**Table 4.1** Runge-Kutta method and Newmark- $\beta$  method

	Runge-Kutta method	Newmark- $\beta$ algorithm
total DOFs	84	84
time step	automatical chosen	$10^{-5}s$
Simulation time	1 s	1 s
Calculation time	2 hours	8 mins

matching with each other.

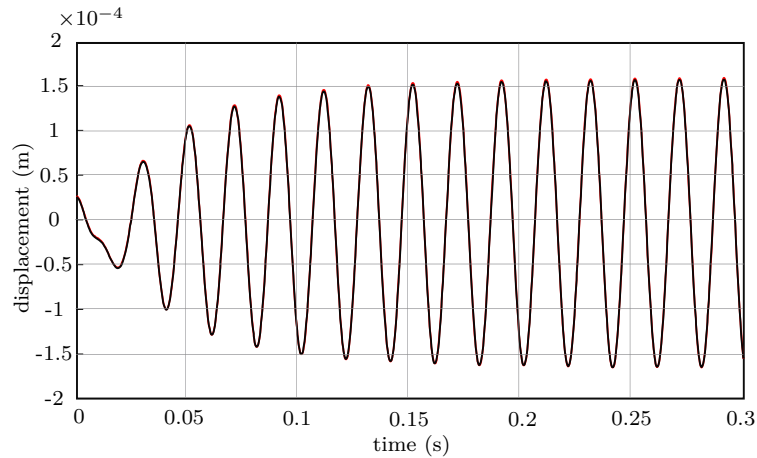


**Fig. 4.2** Responses through Runge-Kutta method and Newmark- $\beta$  method (— Runge-Kutta method; — Newmark- $\beta$  algorithm)

## 4.2 Time-marching with Reduced-order Model

As explained in Chapter 2, the system size is reduced through the Craig-Bampton modal reduction technique. In this section, within the framework of the Hertz contact theory, the time responses of the reduce-order model are compared with those of the full-order model.

Through the time-marching technique, the comparison is conducted with respect to the internal radial clearance and rotational velocity.

The rotor's responses of the reduced-order model with different internal DOFs are compared in Fig. 4.3. It can be seen that the reduced-order model with 12 internal DOFs is able to catch the full-order model's behaviors with high accuracy.

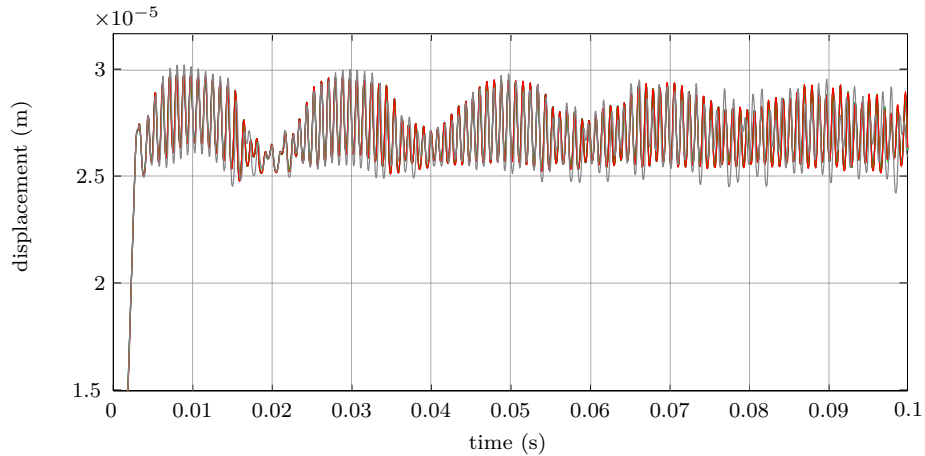


**Fig. 4.3** Internal DOFs convergence (— full-order model; — 20 internal DOFs; — 16 internal DOFs; — 12 internal DOFs; — 8 internal DOFs)

At  $\omega = 50$  Hz (the first critical speed), the rotor's time responses with respect to the internal clearance of the full-order and reduced-order model are compared (Fig. 4.4). It is apparent that the time responses of the two models match well under both low clearance ( $10 \mu\text{m}$ ) and the maximum allowable clearance ( $120 \mu\text{m}$ ).

At the maximum allowable speed (750 Hz), the time responses of the reduce-order and full-order models under internal clearance of  $10 \mu\text{m}$  and  $120 \mu\text{m}$  are depicted in Figs. 4.5(a) and 4.5(b), respectively. Similar to the case of  $\omega = 50$  Hz, the time responses of the reduced-order model do good jobs in matching with that of the full-order model.

<b>Table 4.2</b> Full-order model and reduced-order model		
	Full-order model	Reduced-order model
boundary DOFs	8	8
internal DOFs	76	12
simulation time	1 s	1 s
calculation time	8 mins	40 s

A summarization of the full-order and reduced-order model is listed in Table 4.2. From

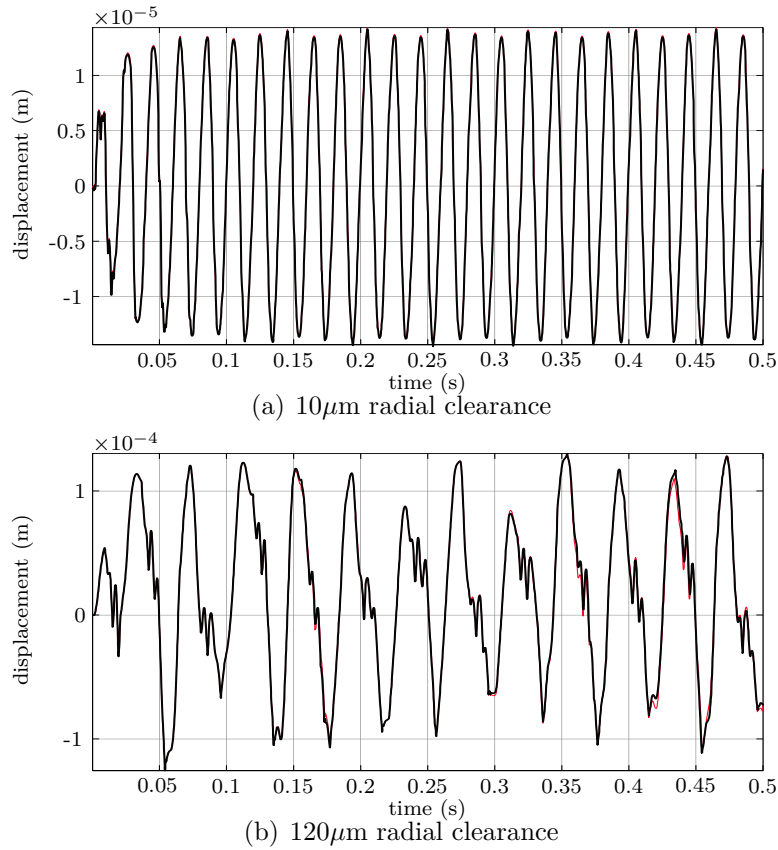


**Fig. 4.4** Time responses of reduced-order and full-order model at  $\omega = 50$  Hz (— full-order model; — reduced-order model)

above analysis, we can conclude that the Craig-Bampton modal reduction technique can reduce the computational efforts substantially with good modal accuracy.

#### 4.2.1 Hertz Approach

Within the framework of the Hertz contact theory, the system responses are obtained through the explicit Newmark- $\beta$  method based on the reduced-order model. Time response, frequency response and rotor's orbit are chosen as the criteria in analyzing the responses, while the contact conditions are investigated via contact zone and contact line. In this work, the responses and contacts are studied with respect to the effects of the internal radial clearance  $\gamma_0$ , the rotational velocity  $\omega$  and the mass imbalance  $me$ .

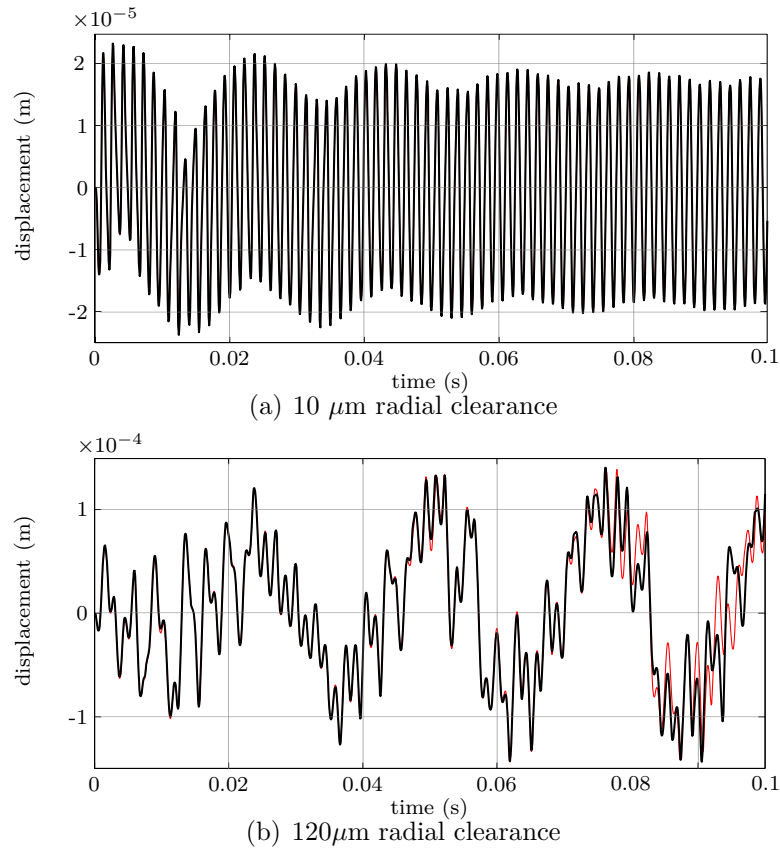


**Fig. 4.5** Time responses of reduced-order and full-order model at  $\omega = 750$  Hz (— full-order model; — reduced-order model)

### Effects of Internal Radial Clearance

First, effects of the internal radial clearance on the responses and contacts are analyzed. Under  $\gamma_0 = 10 \mu\text{m}$ , the vertical time response, vertical frequency response and rotor orbit are illustrated in Fig. 4.6 ( $\omega = 50$  Hz and  $m_e = 4 \times 10^{-5}$  m). Periodic behavior is found in the time response (Fig. 4.6(a)). In the frequency response depicted in Fig. 4.6(b), peak amplitudes of vibration appear at  $\omega$  and  $2\omega$ . The periodic motion is also validated in the rotor's orbit at the bearing location as shown in Fig. 4.6(c). The rotor rotates periodically in the inner surface of the outer ring and the internal radial clearance in the fixed coordinate is completely consumed. With reference to the contact zone in Fig. 4.7(a), it is noticeable that the rotor is supported by uniformly distributed contact forces in the roller bearing. The contact conditions of each roller are studied in the contact line in Fig. 4.7(b). If we

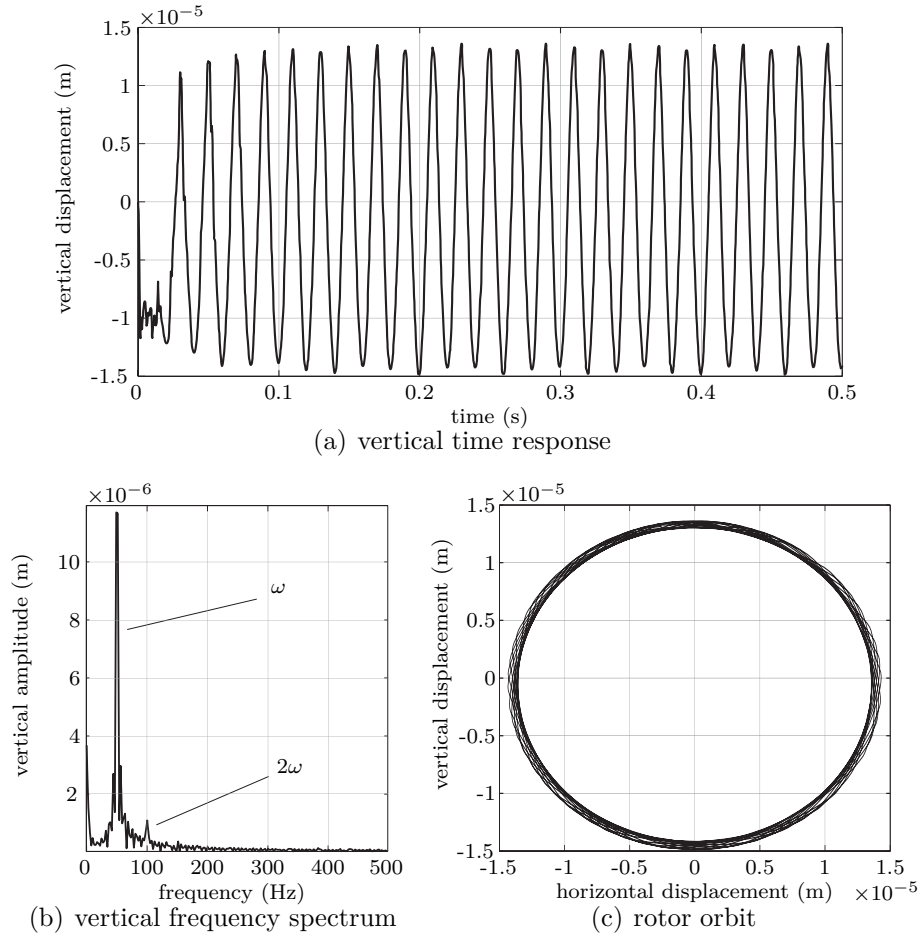


**Fig. 4.6** Responses under  $\gamma_0 = 10 \mu\text{m}$  ( $\omega = 50 \text{ Hz}$  and  $m_e = 4 \times 10^{-5} \text{ m}$ )

look at the third roller, the red horizontal line demonstrates that the roller participates in contact with the outer ring during the time period 0.251–0.26 s. The same idea also holds for other rollers. It is of interest to see that each roller has almost the same amount of contact time, and for any instant, three rollers are in contacts with the outer ring.

For the case of  $\gamma_0 = 30 \mu\text{m}$ , the responses and contact conditions are shown in Figs. 4.8 and 4.9, respectively. In comparison with the case of  $\gamma_0 = 10 \mu\text{m}$ , the time response increases due to the growth of internal radial clearance. Also, quasi-periodic behavior is illustrated (Fig. 4.8(a)). From the frequency response, peaks appear not only at  $\omega$  and  $2\omega$ , but also at  $\omega_{vc}$ , which is the so-called *varying compliance frequency* (*ball passage frequency*).

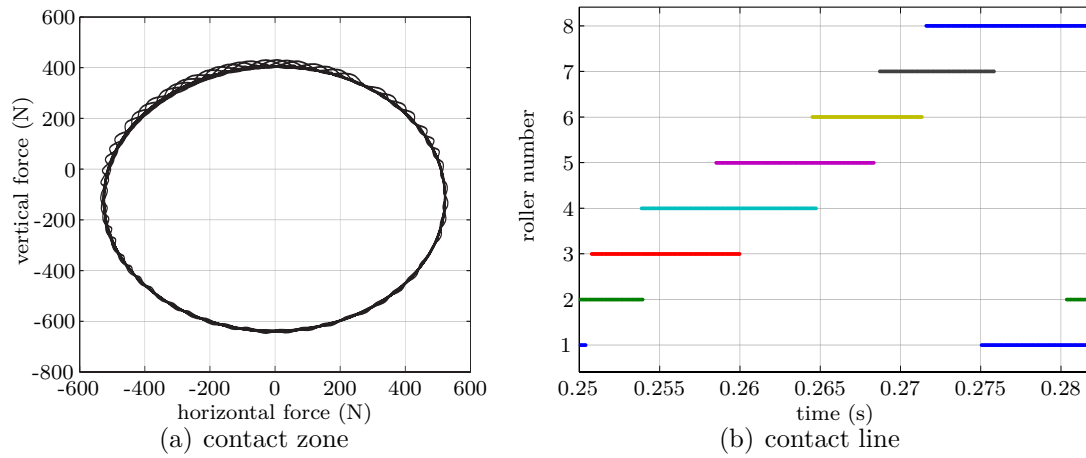


**Fig. 4.7** Contact evaluations under  $\gamma_0 = 10 \mu\text{m}$  ( $\omega = 50 \text{ Hz}$  and  $m_e = 4 \times 10^{-5} \text{ m}$ )

This varying compliance frequency is defined as (Tiwari and Gupta, 2000):

$$\omega_{vc} = \omega_c \times N_b \quad (4.4)$$

i.e., the cage velocity times the roller numbers. Also, with the increase of internal clearance, more peak amplitudes of vibration appear in the frequency spectrum. Besides, the magnitude of the rotor's orbit increases as illustrated in Fig. 4.8(c). In the contact zone (Fig. 4.9(a)), the maximum negative contact forces are higher than the maximum positive forces, indicating that the contacts at the lower part of the bearing are more significant than that at the upper part. This also demonstrates that the contact conditions vary with different rollers, which is validated in the contact line as depicted in Fig. 4.9(b). The contact line illustrates that the amount of contact time for each roller is not the same, and for any instant, only two rollers participate in contacts.

When  $\gamma_0 = 60 \mu\text{m}$ , the negative time responses are significant due to the increase of clearance (Fig. 4.10(a)). In the frequency spectrum, more peaks of small amplitude appear below  $\omega$  (Fig. 4.10(b)). Periodic motion of the rotor is lost, and it shows chaotic behaviors as illustrated in Fig. 4.10(c). Moreover, due to the weight, the motion of the rotor at the lower part of the bearing is dominant. The response is further validated in the contact zone as shown in Fig. 4.11(a). From the contact zone, it is apparent to see that the negative contact forces are more significant, which indicates that the rollers at the lower part of

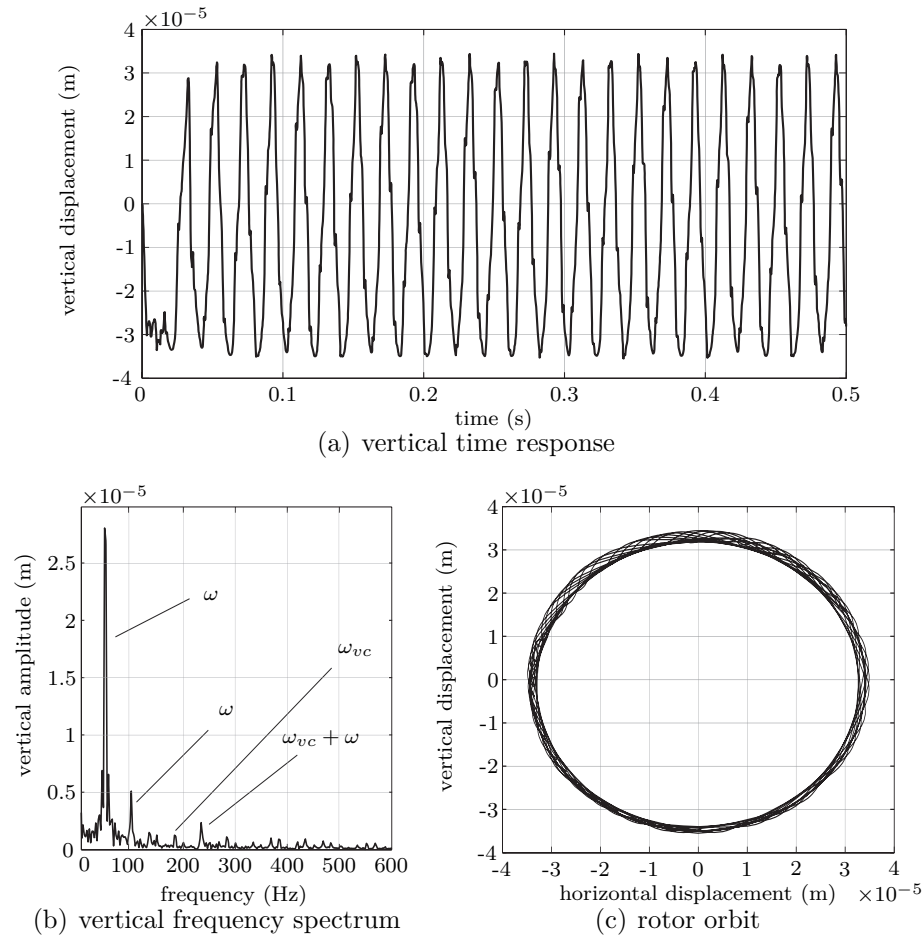


**Fig. 4.8** Responses under  $\gamma_0 = 30 \mu\text{m}$  ( $\omega = 50 \text{ Hz}$  and  $me = 4 \times 10^{-5} \text{ m}$ )

the bearing mainly participate in contacts. Also, this phenomenon can be illustrated in the contact line (Fig. 4.11(b)). For ten revolution periods, different rollers have different contact time; for the period 0.25–0.254 s and 0.272–0.276 s, even no rollers participate in contacts.

### Effects of Rotational Velocity

In this part, effects of the rotational velocity on responses and contacts are studied. The responses at  $\omega = 160 \text{ Hz}$  are illustrated in Fig. 4.12 ( $\gamma_0 = 10 \mu\text{m}$  and  $me = 4 \times 10^{-5} \text{ m}$ ). In comparison with the case of  $\omega = 50 \text{ Hz}$  (Fig. 4.6(a)), it is apparent that the amplitude of the response does not increase or decrease significantly (Fig. 4.12(a)). In the frequency

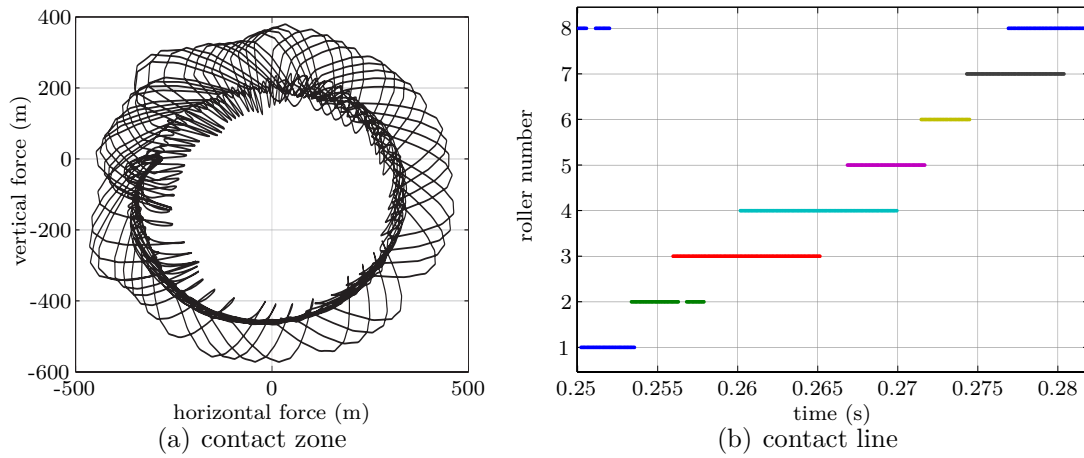


**Fig. 4.9** Contact evaluations under  $\gamma_0 = 30 \mu\text{m}$  ( $\omega = 50 \text{ Hz}$  and  $m_e = 4 \times 10^{-5} \text{ m}$ )

spectrum as depicted in Fig. 4.12(b), it is interesting to see that the vibration is dominated by  $\omega$  and its components. With reference to the rotor's orbit as shown in Fig. 4.12(c), it can be seen that the motion loses periodicity. In addition, it is also noticeable that magnitude of the orbit does not change in comparison with the case of lower velocity (e.g., 50 Hz). In the contact zone (Fig. 4.13(a)), it is apparent that the negative contact forces are dominant, which means that the contacts at the lower part of the bearing are more significant. The contact zone is also validated in the contact line as shown in Fig. 4.13(b). It is noticeable to see that the amount of contact time for each roller is not the same, and during the period 0.25–0.2513 s and 0.2562–0.2574 s, no rollers participate in contacts.

Afterwards, when the rotational velocity reaches the maximum allowable value ( $\omega = 750 \text{ Hz}$ ), the responses and contact conditions are illustrated in Figs. 4.14 and 4.15, respectively. Periodic motion is found in the vertical displacement response as shown in Fig. 4.14(a).  $\omega$  and its components dominate in the frequency spectrum (Fig. 4.14(b)). With reference to the rotor's orbit as illustrated in Fig. 4.14(c), the rotor rotates symmetrically and periodically in the inner surface of the outer ring, and the internal radial clearance is completely consumed. The behaviors of the motion can be demonstrated further in the contact zone as shown in Fig. 4.15(a). From the contact zone, it is apparent that the rotor is supported by uniformly distributed contact forces. Moreover, compared to the case of  $\omega = 50 \text{ Hz}$ , the contact forces increase significantly. In general, uniformly distributed contact force illustrates that the contact conditions for different rollers are the

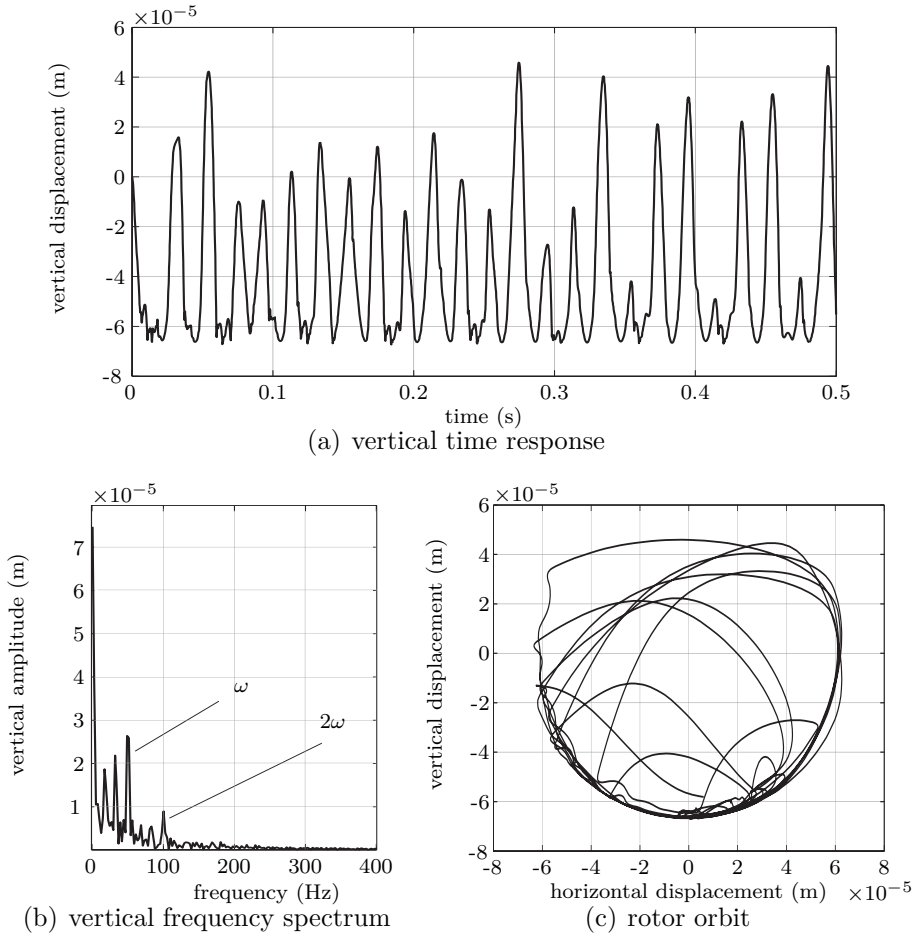


**Fig. 4.10** Responses under  $\gamma_0 = 60 \mu\text{m}$  ( $\omega = 50 \text{ Hz}$  and  $m_e = 4 \times 10^{-5} \text{ m}$ )

same. Hence, all rollers have the same amount of contact time, and for any instant, three rollers participate in contacts (Fig. 4.15(b)).

### Effects of Mass Imbalance

Then, effects of the mass imbalance are studied in this part. With  $m_e = 8 \times 10^{-5} \text{ m}$ , the responses are illustrated in Fig. 4.16 ( $\gamma_0 = 10 \mu\text{m}$  and  $\omega = 50 \text{ Hz}$ ). In comparison with the case of  $m_e = 4 \times 10^{-5} \text{ m}$ , the amplitude of the displacement response does not increase (Fig. 4.16(a)). In the frequency spectrum, peak amplitude of vibration appears at  $\omega$ , and other peaks of small amplitude appear at  $\omega_{vc}$  and  $\omega_{vc} + \omega$  (Fig. 4.16(b)). Besides, the rotor's orbit shows periodic behaviors and the internal radial clearance is completely

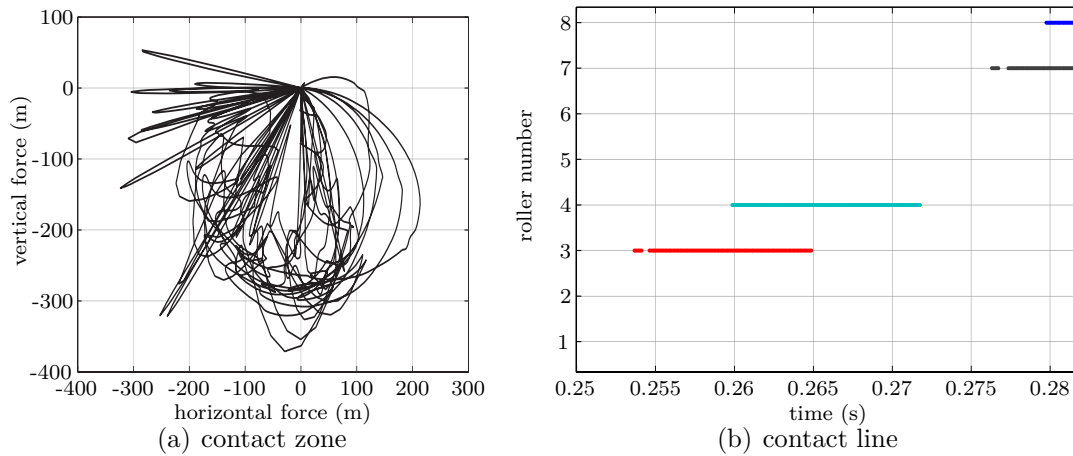


**Fig. 4.11** Contact evaluations under  $\gamma_0 = 60 \mu\text{m}$  ( $\omega = 50 \text{ Hz}$  and  $m_e = 4 \times 10^{-5} \text{ m}$ )

consumed in the fixed coordinates. Similar to the case of  $m_e = 4 \times 10^{-5} \text{ m}$ , uniformly distributed contact forces are illustrated in the contact zone (Fig. 4.16(c)). Moreover, the contact forces increase significantly. If we look at the contact line (Fig. 4.17(b)), all rollers have the same amount of contact time, and three rollers participate in contacts with the outer ring for any instant.

For all the cases under investigation, similar results can be obtained for the horizontal time and frequency responses.

In general, compared to the effects of the mass imbalance, the internal clearance plays a more important role in controlling the responses. Nevertheless, effects of the mass imbalance on the contact forces are dominant. The rotational velocity plays significant roles in the nature of both responses and contacts, and the motion behaves quite differently at different rotational velocities.

### Effects of Roller Rotation and Waviness

Effects of the roller rotation (bending/skewing) and ring waviness on rotor's responses are studied in this part. As explained in Chapter 3, the influences of the roller rotation and ring waviness have to be included in the bearing analysis in some specific working conditions. The rotor's responses at the bearing location due to the roller rotation under radial clearance of  $10 \mu\text{m}$  and  $30 \mu\text{m}$  are illustrated in Figs. 4.18(a) and 4.18(b), respectively. It is apparent that for both cases, effects of the roller rotation on the response are not

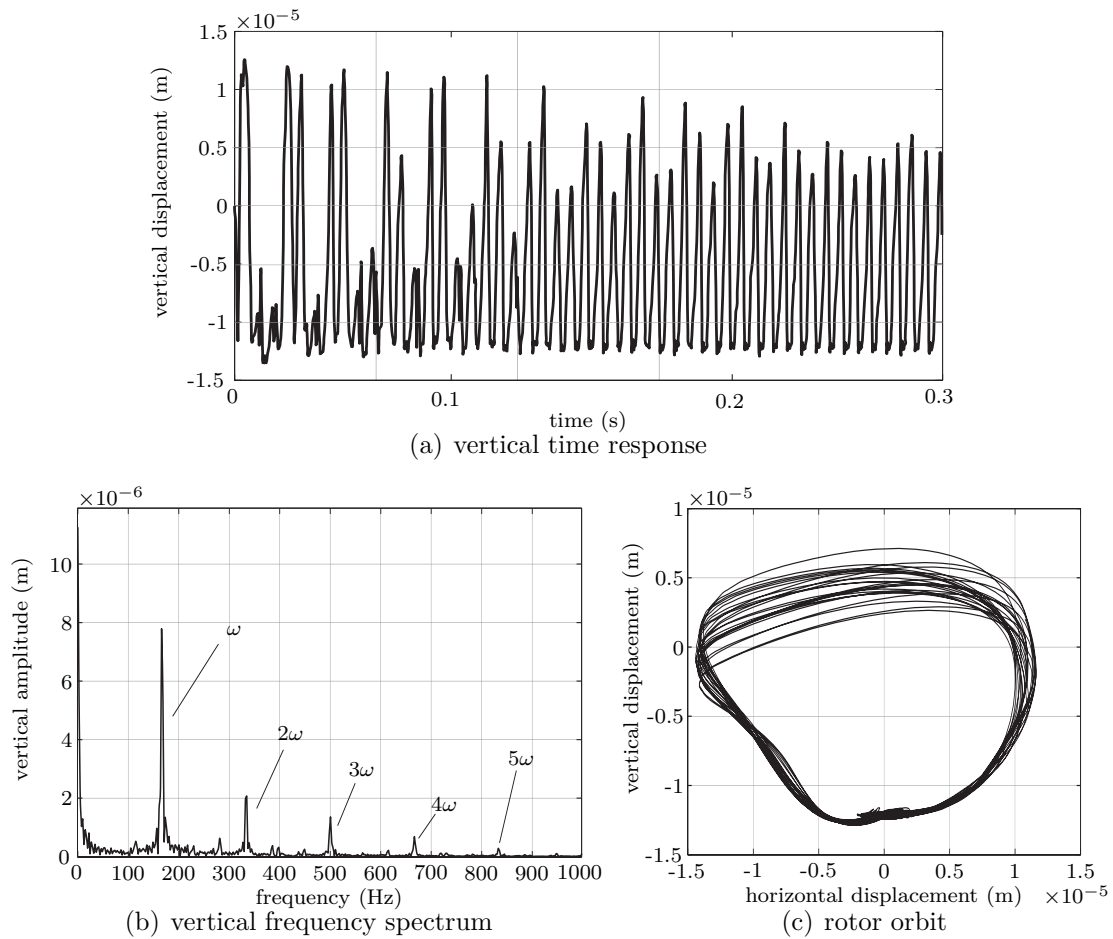


**Fig. 4.12** Responses at  $\omega = 160$  Hz ( $\gamma_0 = 10 \mu\text{m}$  and  $me = 4 \times 10^{-5}$  m)

significant.

At  $\omega = 330$  Hz, the rotor's displacement response under  $\gamma_0 = 10 \mu\text{m}$  with waviness is shown in Fig. 4.19(a). It is noticeable that with waviness, the amplitude of the response increases greatly. Although the magnitude of the waviness ( $1 \mu\text{m}$ ) is very small in comparison with the internal clearance, the effects of waviness on the responses are significant. In Fig. 4.19(b), it is apparent that without waviness, the varying compliance frequency ( $\omega_{vc} = 1103$  Hz) and its components ( $0.5\omega_{vc} = 551$  Hz) dominate in the frequency spectrum.

In addition, as explained in Chapter 3, the roles of waviness orders in controlling the system's nonlinear response are important (Wang et al., 2007). In our analysis, the frequency spectrum is chosen as the criteria in analyzing the rotor's response with respect to different

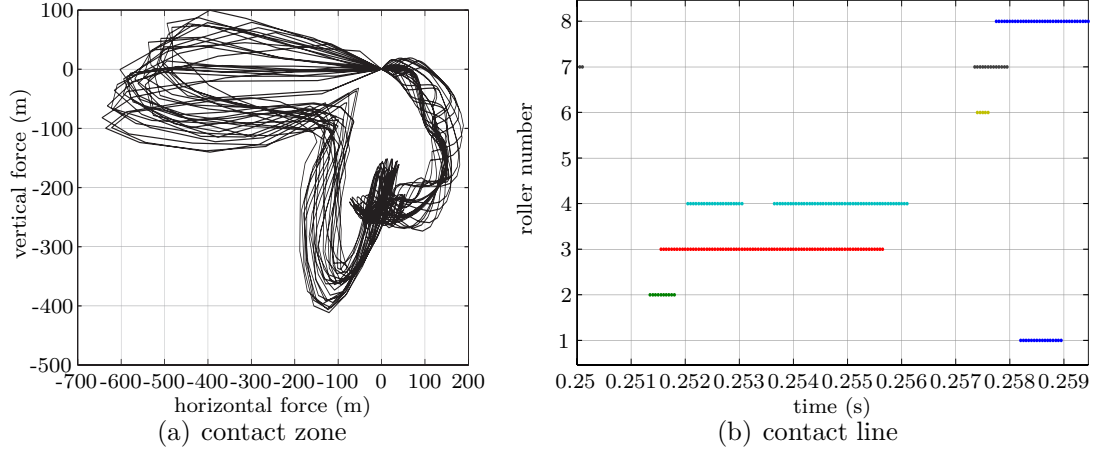


**Fig. 4.13** Contact evaluations at  $\omega = 160$  Hz ( $\gamma_0 = 10 \mu\text{m}$  and  $me = 4 \times 10^{-5}$  m)

waviness orders. Four cases of waviness are investigated, and the frequency responses are illustrated in Fig. 4.20. When the waviness order is 5 (Fig. 4.20(a)), peak amplitudes of vibration appear at 551 Hz, 137 Hz, 275 Hz and 1102 Hz, which correspond to  $(N_w\omega_c - \omega_c)$ ,  $0.25(N_w\omega_c - \omega_c)$ ,  $0.5(N_w\omega_c - \omega_c)$  and  $2(N_w\omega_c - \omega_c)$ <sup>1</sup>. From the frequency spectrum, it is of interest to see that the amplitudes of vibration peaks increase significantly with waviness. For example, the amplitude of the response at 413 Hz with waviness reaches almost 3 times of the largest frequency response without waviness. Similarly, with 10 waviness orders (Fig. 4.20(b)), peaks appear at 1241 Hz, 620 Hz, 310 Hz and 1552 Hz, corresponding to  $(N_w\omega_c - \omega_c)$ ,  $(0.5N_w\omega_c - \omega_c)$ ,  $(0.25N_w\omega_c - \omega_c)$  and  $(1.25N_w\omega_c - \omega_c)$ . With 20 waviness orders (Fig. 4.20(c)), peaks appear at 2611 Hz, 1310 Hz, 872 Hz and 430 Hz in the frequency spectrum, corresponding to  $(N_w\omega_c - \omega_c)$ ,  $(0.5N_w\omega_c - \omega_c)$ ,  $(0.3N_w\omega_c - \omega_c)$  and  $(0.15N_w\omega_c - \omega_c)$ . When the waviness order increases to 40 (Fig. 4.20(d)), peak amplitudes of vibration appear at 5380 Hz, 2691 Hz, 1076 Hz and 538 Hz, which are  $(N_w\omega_c - \omega_c)$ ,  $(0.5N_w\omega_c - \omega_c)$ ,  $(0.2N_w\omega_c - \omega_c)$  and  $(0.1N_w\omega_c - \omega_c)$ . Based on above analysis, it is noticeable that with waviness, the dominant frequencies are relevant to waviness orders and the varying compliance frequency, which are defined as:

$$\omega_P = (\omega_c N_w - \omega_c) \quad (4.5)$$

<sup>1</sup> $N_w$  is the waviness order.

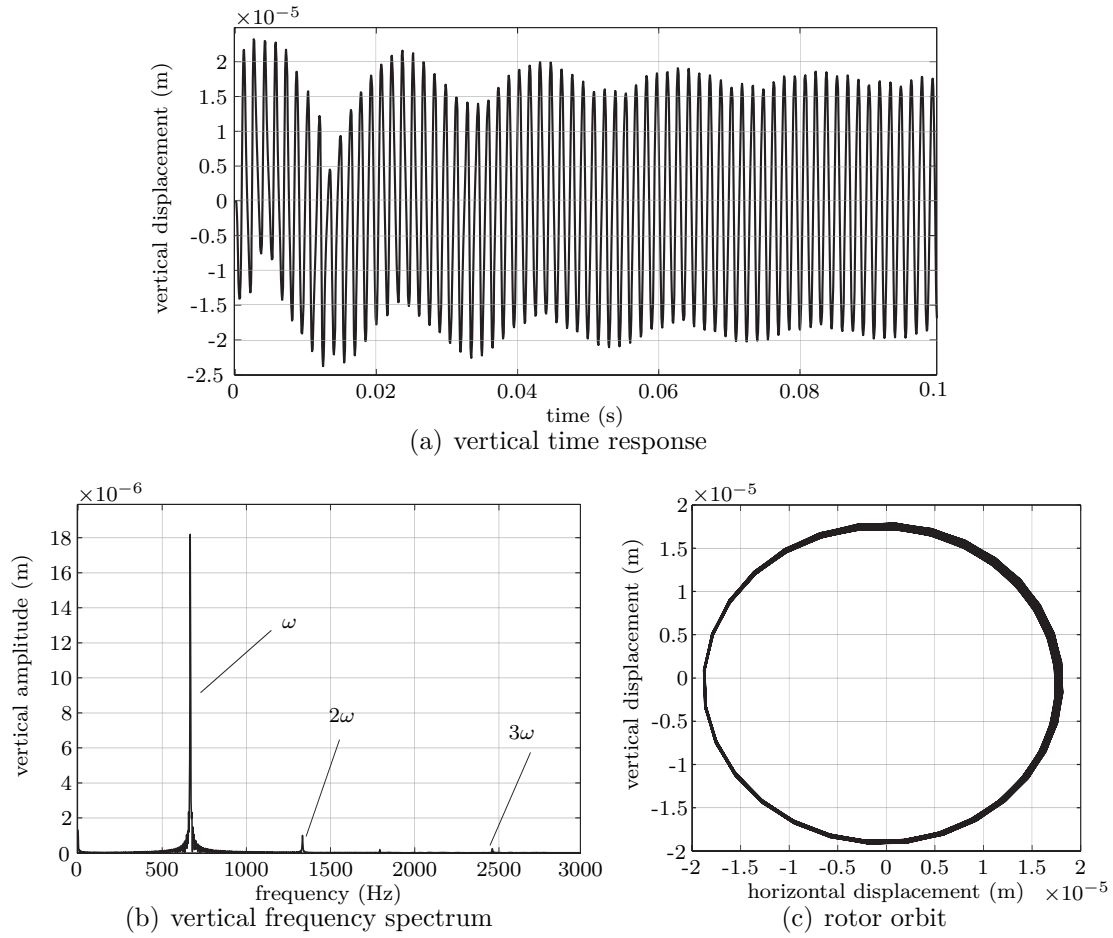


**Fig. 4.14** Responses at  $\omega = 750$  Hz ( $\gamma_0 = 10 \mu\text{m}$  and  $me = 4 \times 10^{-5}$  m)

where  $\omega_P$  is sometimes called *waviness vibration frequency* (Wang et al., 2007).

Generally, with waviness, the amplitude of the displacement responses increases significantly and the dominant frequency response is no longer the varying compliance frequency, but the waviness vibration frequency.

#### 4.2.2 Lagrange Multipliers Approach

In this part, the Lagrange multipliers technique compatible with the central difference method is employed to handle the contact constraints. This method includes three parts as follows (Carpenter et al., 1991):

1. **Resetting initial conditions** The initial conditions are firstly set for the time step

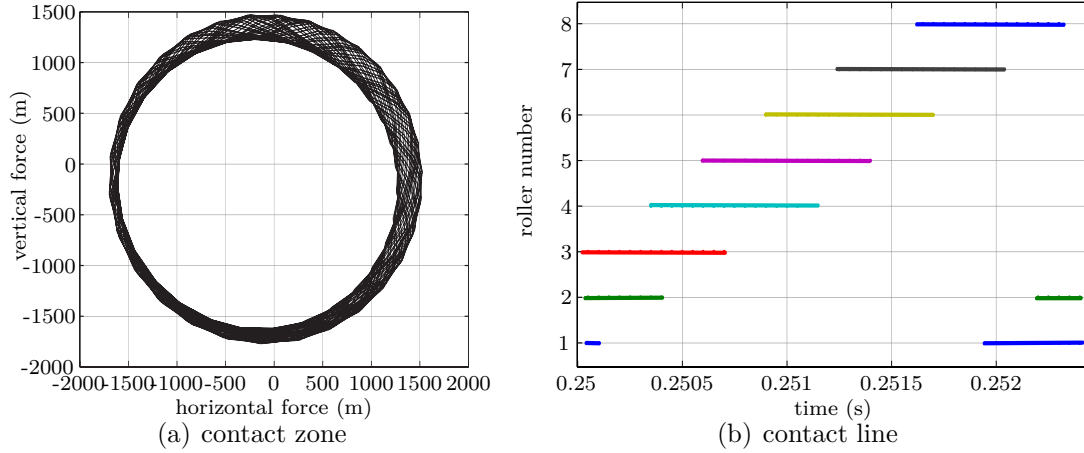


**Fig. 4.15** Contact evaluations at  $\omega = 750$  Hz ( $\gamma_0 = 10 \mu\text{m}$  and  $me = 4 \times 10^{-5}$  m)

$n + 1$ . Involving mass, damping and stiffness matrices  $\mathbf{M}$ ,  $\mathbf{D}$  and  $\mathbf{K}$ , the resetting of the initial displacement vector is (with subscript  $r$  for resetting):

$$\mathbf{q}_{n+1,r} = \left[ \frac{\mathbf{M}}{h^2} + \frac{\mathbf{D}}{2h} \right]^{-1} \left( \left( \frac{2\mathbf{M}}{h^2} - \mathbf{K} \right) \mathbf{q}_n + \left( \frac{\mathbf{D}}{2h} - \frac{\mathbf{M}}{h^2} \right) \mathbf{q}_{n-1} + \mathbf{F}_n \right) \quad (4.6)$$

- Determination of contacts** The key step is the determination of contacts. On the basis of the contact matrix  $\mathbf{J}$ , the determination term is written as:

$$\mathbf{g}_{n+1} = \mathbf{J}\mathbf{q} - \gamma_0 \quad (4.7)$$

where  $\mathbf{g}_{n+1}$  is the clearance vector of the contacts.

- Correction** The correction should be considered for each time step. For the determination term  $g_{n+1}$ , only the positive terms are chosen, and the negative terms are treated as 0. It means that the determination terms are kept only when the contact occurs. The correction term yields the additional equations for the unknown Lagrange multipliers vector  $\lambda$

$$\mathbf{q}_{n+1} = \mathbf{q}_{n+1,r} - \left[ \frac{\mathbf{M}}{h^2} + \frac{\mathbf{D}}{2h} \right]^{-1} \mathbf{J}^T \lambda \quad (4.8)$$

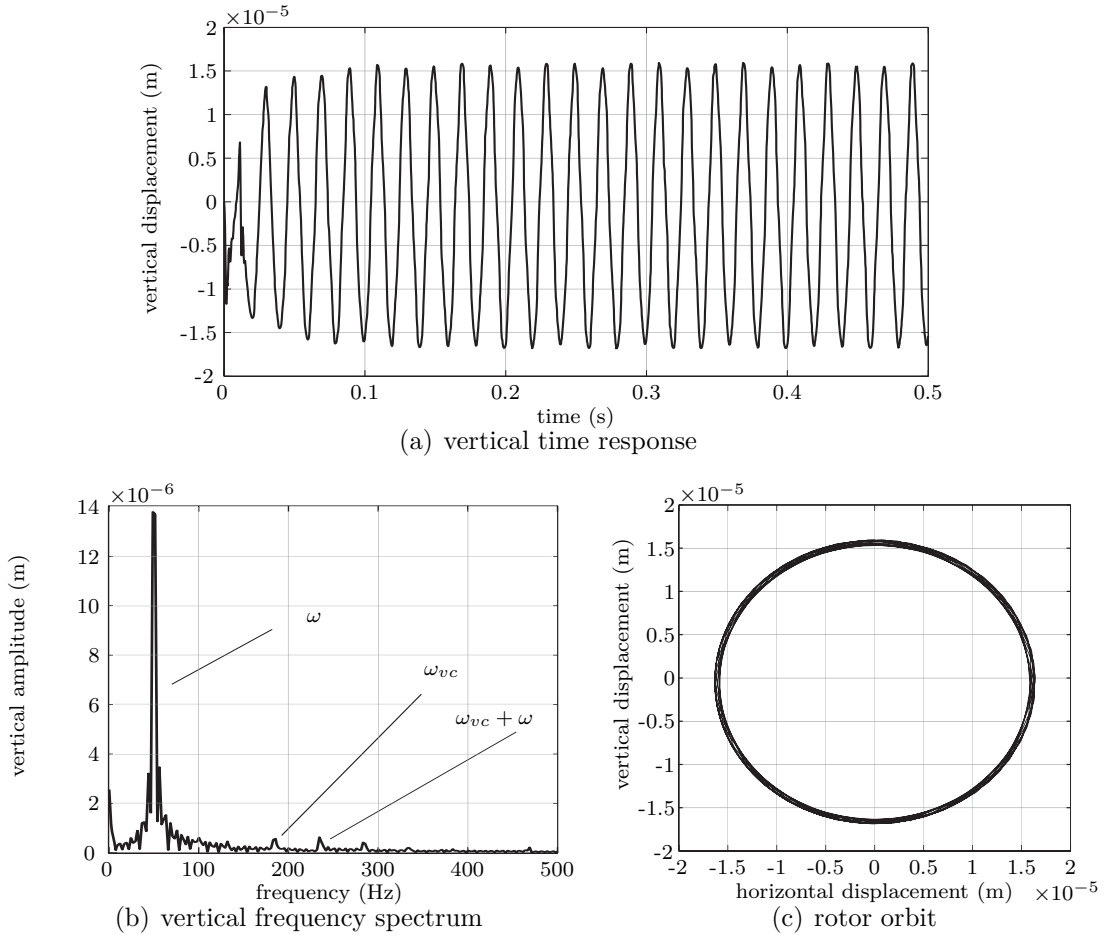
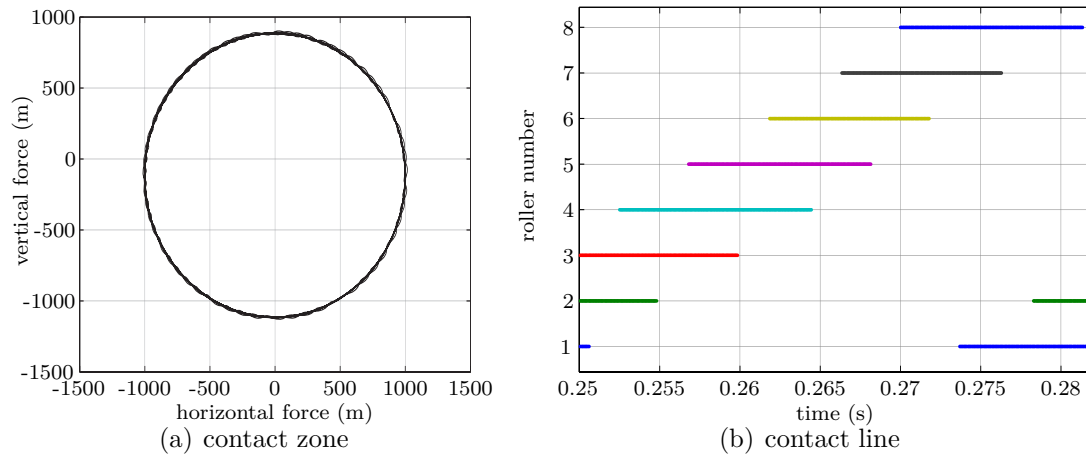


**Fig. 4.16** Responses with  $me = 8 \times 10^{-5}$  m ( $\gamma_0 = 10 \mu\text{m}$  and  $\omega = 50$  Hz)

From Eq. (4.6), (4.7) and (4.8), the Lagrange multiplier vector is obtained as:

$$\lambda = \left( \mathbf{J} \left[ \frac{\mathbf{M}}{h^2} + \frac{\mathbf{D}}{2h} \right]^{-1} \mathbf{J}^T \right)^{-1} \mathbf{g}_{n+1} \quad (4.9)$$

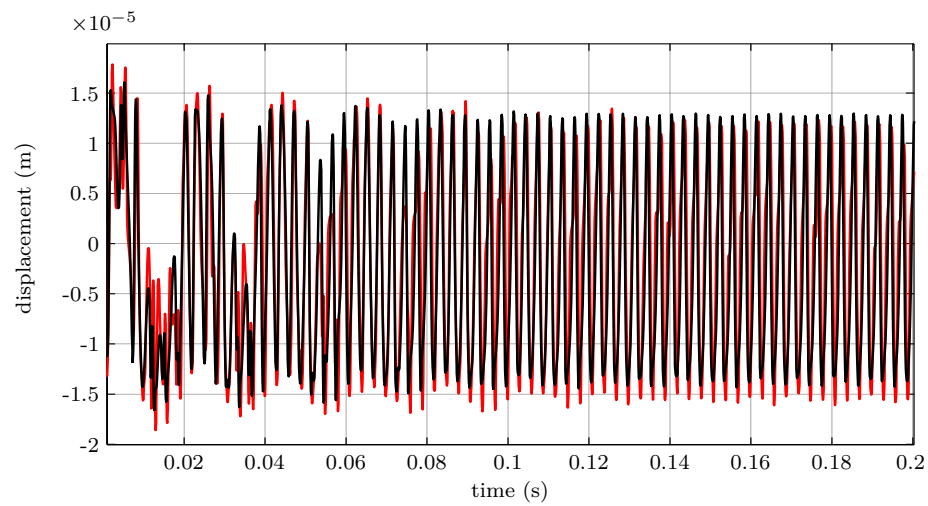
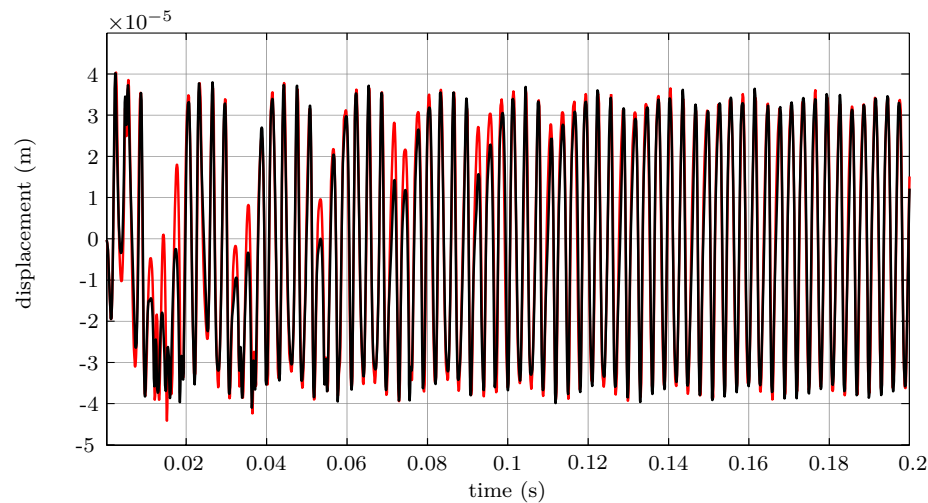
Through the time-marching technique, the rotor's responses within the framework of Lagrange multipliers technique are investigated. Three cases are simulated via this constraint Lagrange multipliers approach. For all cases, the rotor's radial displacement responses are compared with that using Hertz approach. Also, the bearing's contact force for each case is analyzed.



**Fig. 4.17** Contact evaluations with  $me = 8 \times 10^{-5}$  m ( $\gamma_0 = 10 \mu\text{m}$  and  $\omega = 50$  Hz)

Fig. 4.21 illustrates the rotor's displacement response at the bearing location and the bearing radial contact force ( $\omega = 50$  Hz and  $\gamma_0 = 10 \mu\text{m}$ ). Under low radial clearance ( $10 \mu\text{m}$ ), the radial displacement responses obtained via the Hertz approach and Lagrange multipliers technique are shown in Fig. 4.21(a). The red line illustrates the internal radial clearance. It is apparent that for Lagrange multipliers approach, rollers move back simultaneously when they consume the internal radial clearance. At the same time, contact occurs. No penetration is detected. This is due to the fact that, in the Lagrange multipliers approach, the contact is treated as infinitely stiff contact. Conversely, for the case of Hertz contact, rollers continue to move into the outer ring even though they consume the internal radial clearance completely. In Fig. 4.21(a), the penetration for the Hertz approach is illustrated as the blue curve above the red line. It is also noticeable that the penetration depth is very small compared to the internal radial clearance. If we look at the contact force shown in Fig. 4.21(b), it is interesting to see that peaks appear when the rollers contact the outer ring.

As the internal radial clearance is increased to  $30 \mu\text{m}$ , the rotor's response and bearing radial contact force are shown in Figs. 4.22(a) and 4.22(b), respectively. Similarly, penetration is detected through the Hertz approach; while for the Lagrange multipliers technique, the rotor's maximum radial displacement is equivalent to the internal radial clearance. With the increase of internal clearance, both the radial displacement and contact force increase.

(a) radial clearance of  $10 \mu\text{m}$ (b) radial clearance of  $30 \mu\text{m}$ 

**Fig. 4.18** Time responses with roller rotation (— with roller rotation; — without roller rotation)

Then, effects of the rotational velocity on the system responses via the Lagrange multipliers technique are illustrated in Figs. 4.23(a) and 4.23(b). Still, contact occurs when rollers reach the outer ring. It is apparent that with the increase of rotational velocity, there is a corresponding significant growth of the radial contact force.

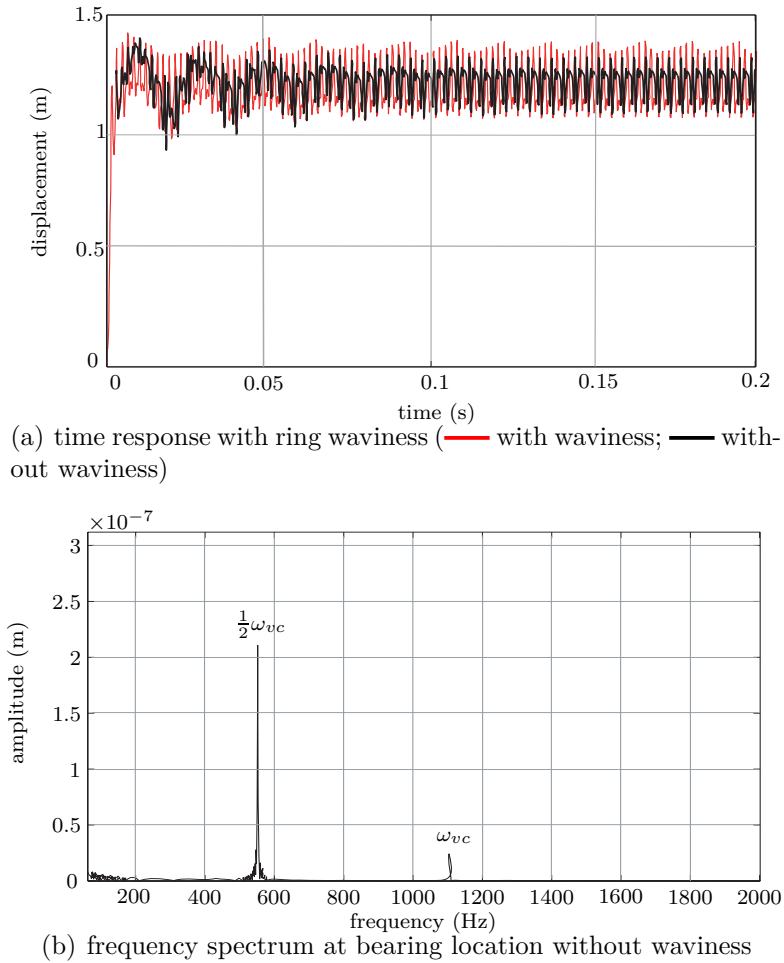
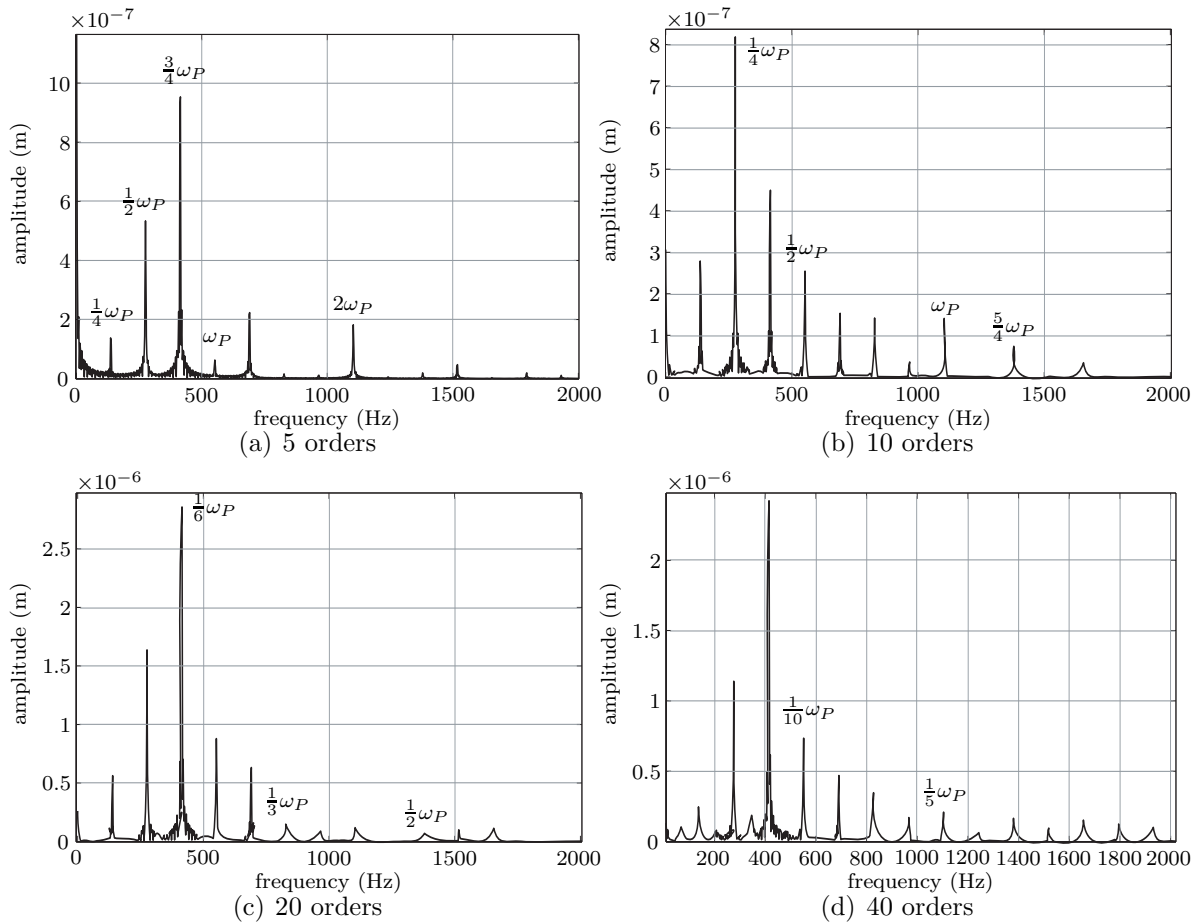


**Fig. 4.19** Time response with ring waviness and varying compliance frequency

### 4.2.3 Forcing Functions Approach

Based on forcing functions, the responses through the time-marching technique are studied in this part. As explained in Chapter 3, in some specific working conditions, it is of interest to construct a direct relationship between bearing contact forces and deflections with rotational velocity (Fleming and Poplawski, 2005). In our analysis, two cases are simulated and analyzed, whose responses are compared with that obtained by the classical Hertz approach.

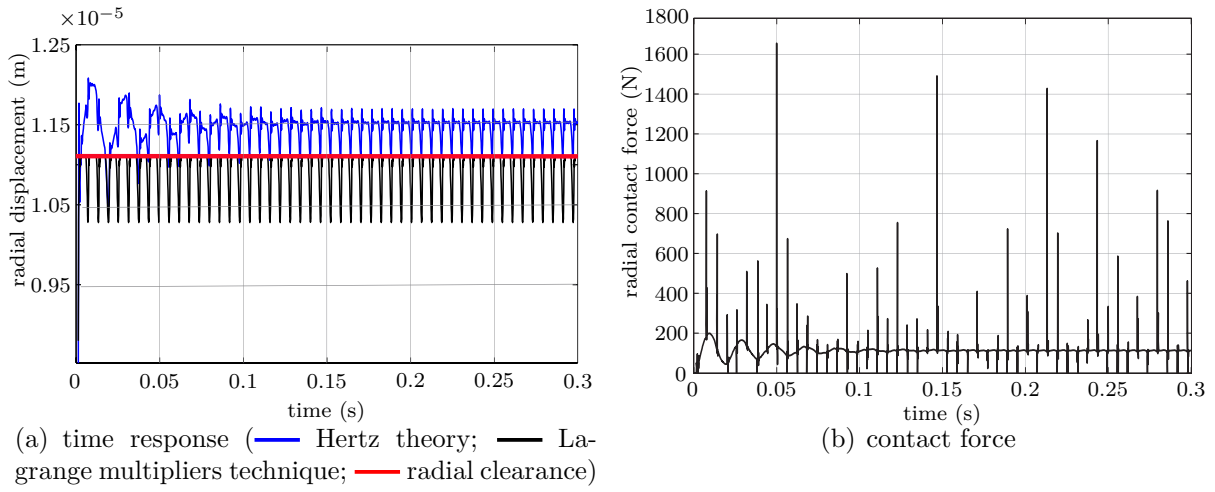
For the case in which  $me = 2 \times 10^{-5}$  m is applied on the central disk, the contact force surface with respect to rotational velocity and penetration depth is shown in Fig. 4.24(a).



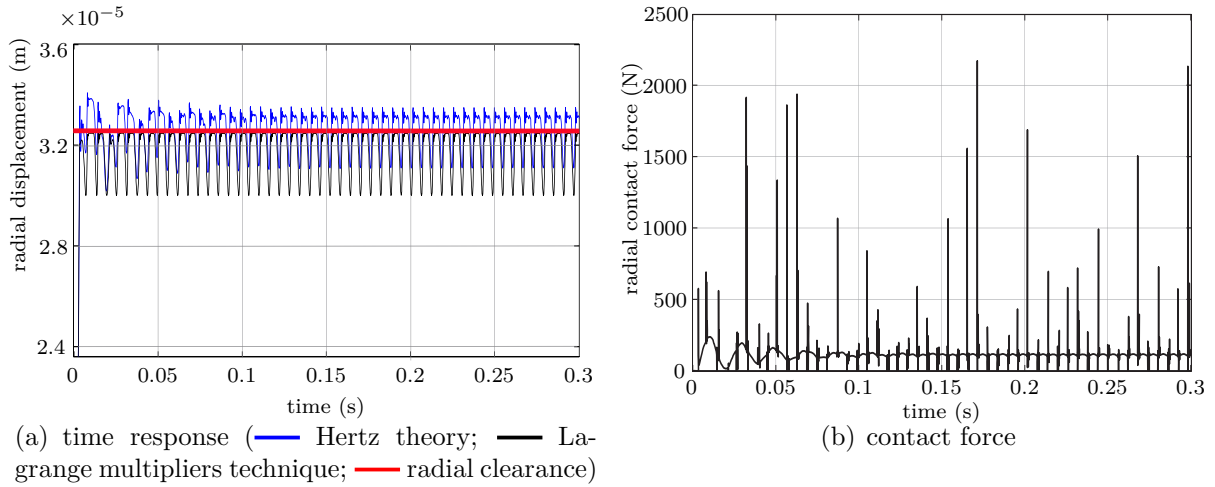
**Fig. 4.20** Frequency responses with respect to waviness orders

Fig. 4.24(b) demonstrates the responses obtained through the forcing function and Hertz contact theory. The responses match well with each other.

As for the case of  $me = 4 \times 10^{-5}$  m, the contact force surface with respect to rotational velocity and penetration depth is depicted in Fig. 4.25(a). Similarly, comparison of the responses obtained via the Hertz theory and forcing functions are shown in Fig. 4.25(b). Both the contact force surface and comparison results illustrate that the curve fitting does a good job of matching the data points and the Hertz contact model.



**Fig. 4.21** Responses through Lagrange multipliers technique at  $\omega = 50$  Hz and  $\gamma_0 = 10 \mu\text{m}$



**Fig. 4.22** Responses through Lagrange multipliers technique at  $\omega = 50$  Hz and  $\gamma_0 = 30 \mu\text{m}$

### 4.3 Harmonic Balance Method

In this section, the harmonic balance method (HBM) is adopted to solve equations of motion of the system. The main principle of the HBM is to transform the displacement responses and nonlinear forces from time domain to frequency domain. Through this way, the second order differential equations are transformed into a set of nonlinear algebraic equations, which are solved using nonlinear equations solver, such as Newton-Raphson

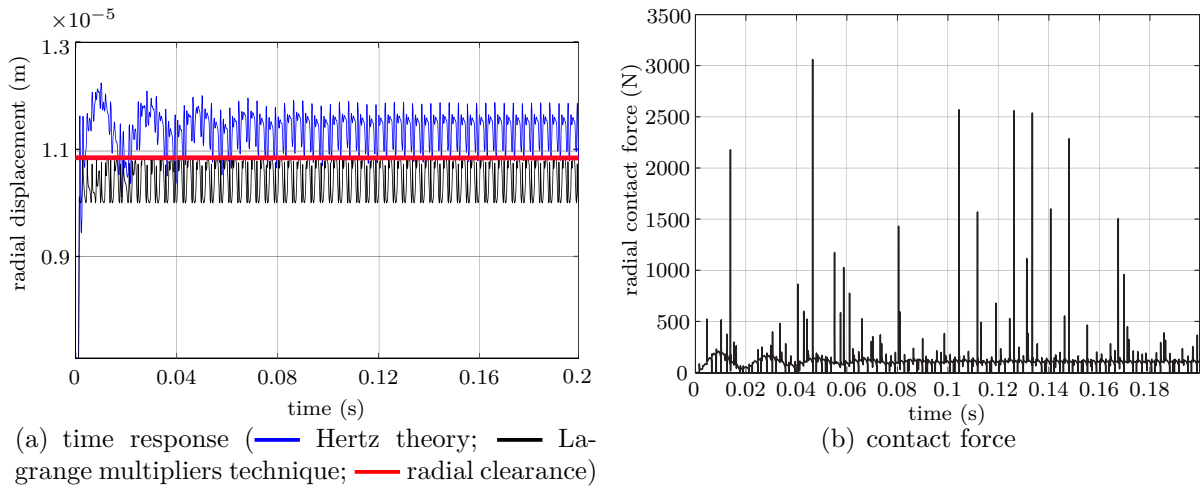


**Fig. 4.23** Responses through Lagrange multipliers technique at  $\omega = 160$  Hz and  $\gamma_0 = 10 \mu\text{m}$

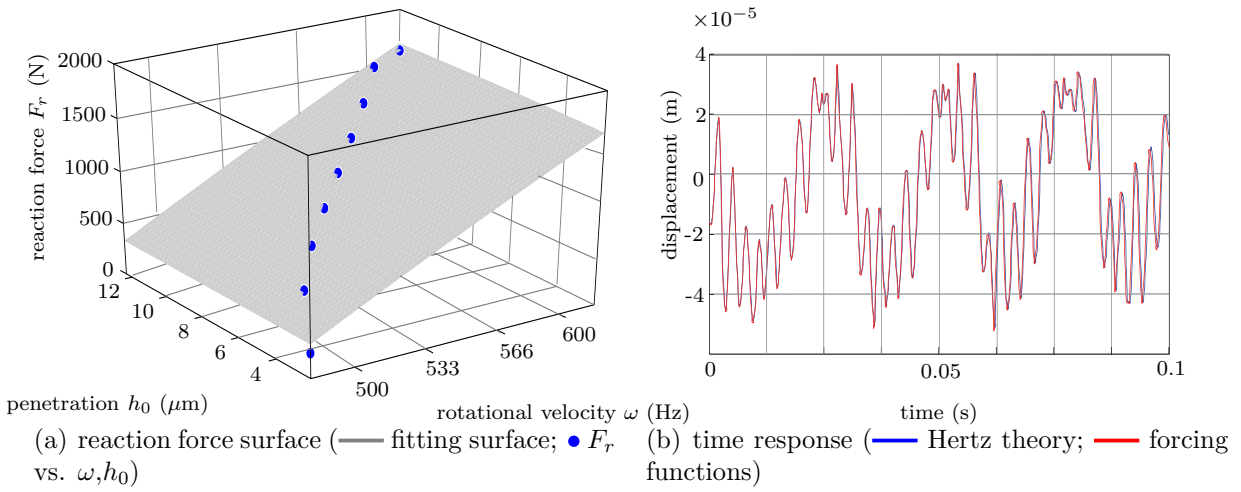


**Fig. 4.24** Response through forcing functions with  $me = 2 \times 10^{-5}$  m

method. Fig. 4.26 illustrates the principle of the HBM. Assuming that we have the unknowns  $\mathbf{q}_t$  and  $\mathbf{F}_{NL}$  in time domain, they are transformed into  $\mathbf{B}_0, \mathbf{B}_k, \mathbf{A}_k,$  and  $\mathbf{C}_0, \mathbf{C}_k, \mathbf{S}_k$  in frequency domain through FFT (fast Fourier transform). Then, the equation of motion is built in frequency domain with a set of nonlinear algebraic equations  $H(Z, \omega)$ . By means of the Newton-Raphson method, the nonlinear equations are solved iteratively; afterwards, through IFFT (inverse fast Fourier transform), the solutions are transformed back into time domain.

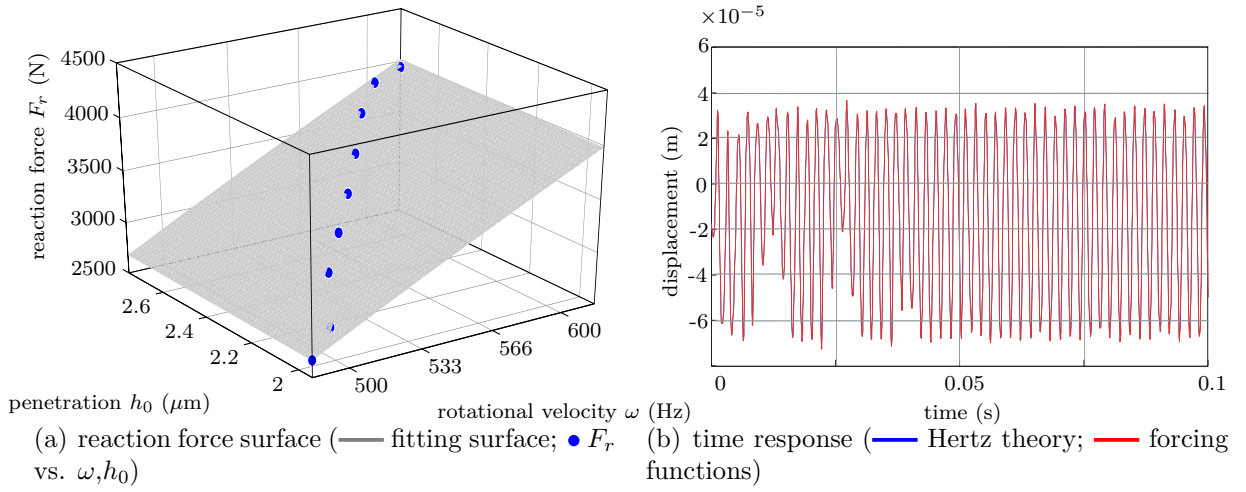


**Fig. 4.25** Response through forcing functions with  $me = 4 \times 10^{-5}$  m

Following the HBM, the displacement vector is written in the following form:

$$\mathbf{q}_t = \mathbf{B}\cos(\omega t) + \mathbf{A}\sin(\omega t) \quad (4.10)$$

where  $\mathbf{B}$  and  $\mathbf{A}$  are Fourier coefficients in frequency domain. Similarly, the force vector is written as:

$$\mathbf{F} = \mathbf{C}\cos(\omega t) + \mathbf{S}\sin(\omega t) \quad (4.11)$$

where  $\mathbf{C}$  and  $\mathbf{D}$  are finite Fourier series. By substituting Eq. (4.10) and Eq. (4.11) into the system's equation of motion, and selecting the terms of  $\cos(\omega t)$  and  $\sin(\omega t)$  together, the equation of motion becomes:

$$\begin{bmatrix} \mathbf{K} - \omega^2\mathbf{M} & -\omega\mathbf{C} \\ \omega\mathbf{C} & \mathbf{K} - \omega^2\mathbf{M} \end{bmatrix} \begin{pmatrix} \mathbf{A} \\ \mathbf{B} \end{pmatrix} = \begin{pmatrix} \mathbf{S} \\ \mathbf{C} \end{pmatrix} \quad (4.12)$$

In order to capture the nonlinear response of the rotor-bearing system, more harmonics are required in the frequency domain to estimate the Fourier coefficients (Sinou, 2009). Assuming that the nonlinear dynamic response of the system is approximated by finite Fourier series with period  $T = 2\pi/\omega$ , the displacement vector is expressed as:

$$\mathbf{q}_t = \mathbf{B}_0 + \sum_{k=1}^m [\mathbf{B}_k\cos(k\omega t) + \mathbf{A}_k\sin(k\omega t)] \quad (4.13)$$

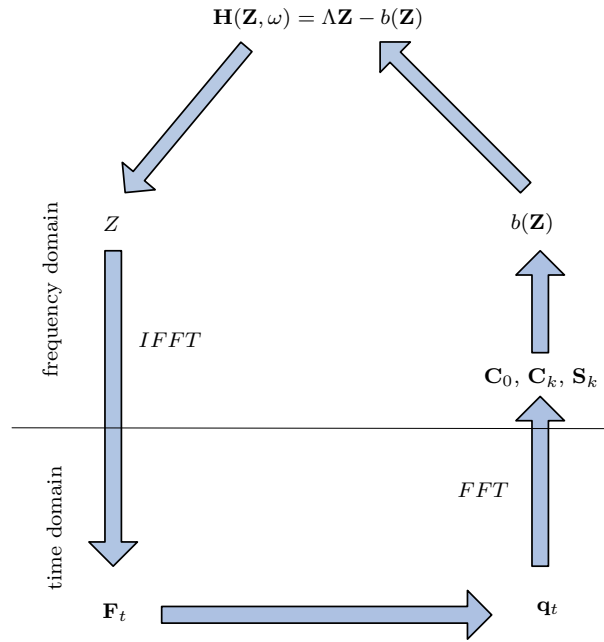


**Fig. 4.26** Harmonic balance method introduction (Sinou, 2009)

where  $m$  is the number of harmonics,  $\mathbf{B}_0$  is the constant Fourier coefficient,  $\mathbf{B}_k$  and  $\mathbf{A}_k$  are the Fourier coefficients for the  $k^{\text{th}}$  cosine and sine term. The force vector  $\mathbf{F}$  is also expressed in terms of Fourier coefficients. In our system, the force vector contains nonlinear contact forces, unbalanced forces and the weight. Similarly, the force vector is expressed as:

$$\mathbf{F} = \mathbf{C}_0 + \sum_{k=1}^m [\mathbf{C}_k \cos(k\omega t) + \mathbf{S}_k \sin(k\omega t)] \quad (4.14)$$

Substituting the Fourier representation of the displacement vector in Eq. (4.13) and force vector in Eq. (4.14) into the system equation of motion yields  $(2m + 1) \times n$  nonlinear algebraic equations ( $n$  is the number of system's DOFs). Then, the cosine, sine and constant terms are balanced respectively. Consequently, the balanced equation for the constant terms is:

$$\mathbf{K}\mathbf{B}_0 = \mathbf{C}_0 \quad (4.15)$$

For the  $k^{\text{th}}$  cosine term, the balanced equation is:

$$(\mathbf{K} - (k\omega)^2\mathbf{M})\mathbf{B}_k + (k\omega)\mathbf{D}\mathbf{A}_k = \mathbf{C}_k \quad (4.16)$$



The  $k^{\text{th}}$  cosine and sine Fourier coefficients of the force vector are:

$$\begin{aligned} \mathbf{C}_k &= \frac{2}{T} \int_0^T \mathbf{F} \cos(k\omega t) dt \\ \mathbf{S}_k &= \frac{2}{T} \int_0^T \mathbf{F} \sin(k\omega t) dt \end{aligned} \quad (4.22)$$

where  $T$  is the period of FFT, and  $T = 2\pi/\omega$ .

By the initial estimation of the  $\mathbf{Z}$  vector, whose components are the Fourier coefficients of the DOFs, the nonlinear algebraic equations are constructed. With the help of the Newton-Raphson method, the nonlinear algebraic equations are solved iteratively.

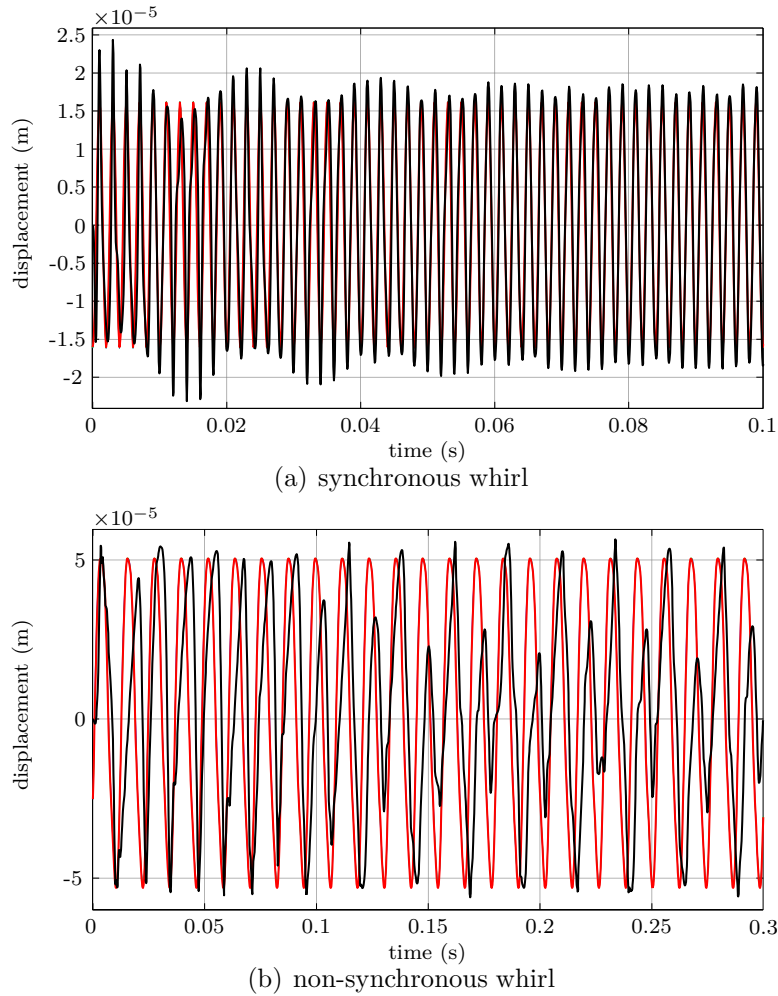


**Fig. 4.27** Comparison of HBM and time-marching technique (— 1 harmonic; — 2 harmonics; — 3 harmonics; — Newmark- $\beta$  method)

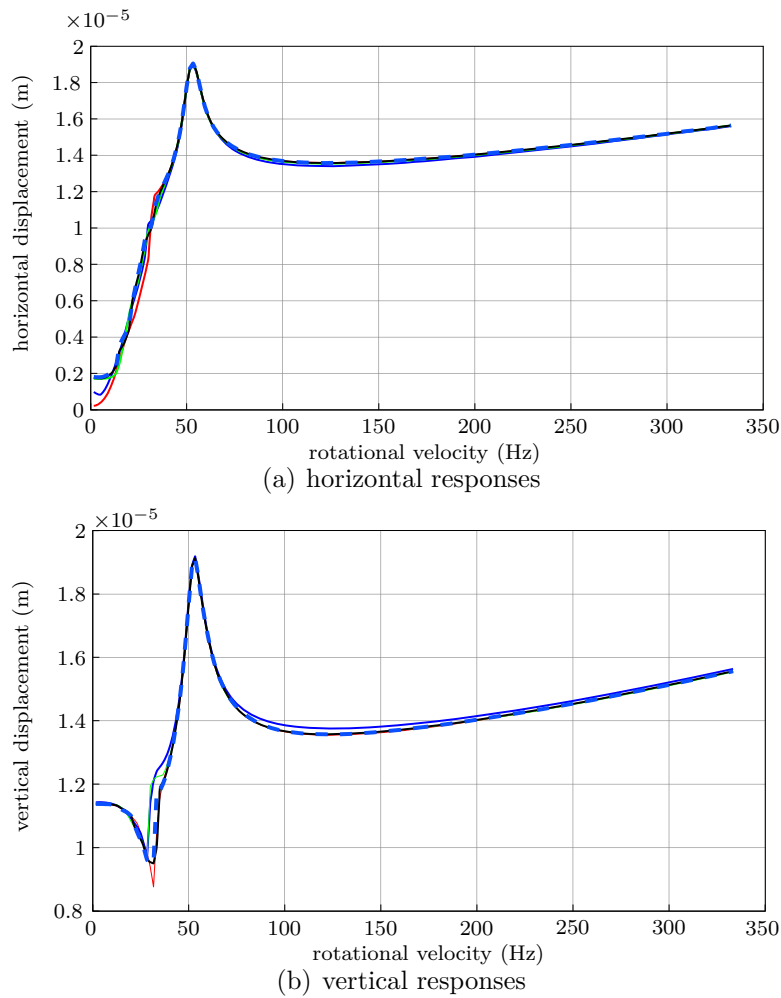


**Fig. 4.28** Nonlinear responses under  $\gamma_0 = 10 \mu\text{m}$  (— 1 harmonic; — 2 harmonics; — 3 harmonics; — 4 harmonics; - - - 5 harmonics)

The rotor's responses at the bearing location obtained through time-marching technique and the HBM are compared in Fig. 4.27. At  $\omega = 330 \text{ Hz}$  under  $\gamma_0 = 10 \mu\text{m}$ , the rotor's motion is periodic. Only synchronous whirl is found. With reference to Fig. 4.27(a), it is noticeable that the responses obtained through the HBM and time-marching technique match well. However, for the non-synchronous whirl illustrated in Fig. 4.27(b) ( $\omega = 160 \text{ Hz}$  and  $\gamma_0 = 30 \mu\text{m}$ ), the response through the HBM does not do a good job in matching with that through the time-marching technique. Actually, the HBM is capable of capturing synchronous vibration, while it is not applicable for non-synchronous whirl (Hu and Tang, 2006).

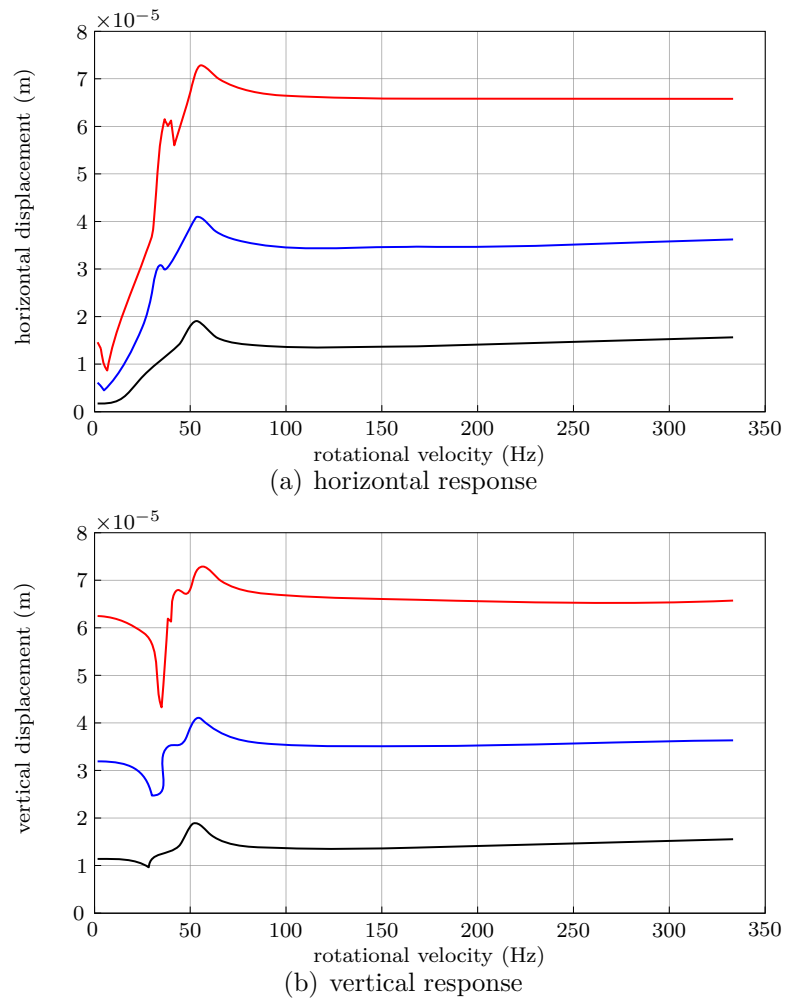


**Fig. 4.29** Effects of internal radial clearance on nonlinear responses (—  $\gamma_0 = 10 \mu\text{m}$ ; —  $\gamma_0 = 30 \mu\text{m}$ ; —  $\gamma_0 = 60 \mu\text{m}$ )

In order to study the importance of harmonic orders in capturing the nonlinear behaviors of the system, the nonlinear responses of the system with five harmonics are investigated as illustrated in Fig.4.28. It is difficult to conclude how many harmonics are enough to capture the nonlinear behaviors of rotor-bearing system. However, for strong nonlinear problems, one harmonic is too limited (Sinou, 2009). Consequently, it is of great interest to investigate the influence of harmonic orders on the system's response. The criterion in choosing the number of harmonics is on the basis of number of significant harmonics expected in the system's nonlinear dynamic response. In this study, five harmonics are included in our analysis due to the fact that, with more harmonics, the computational

efforts increase significantly. Moreover, for upper harmonic orders, harmonic components become much less significant. As shown in Figs. 4.28(a) and 4.28(b), it is noticeable that in both horizontal and vertical directions, resonance appears close to the first critical speed. Also, harmonics play less important roles with the increase of their orders.

Then, the effects of internal radial clearance on the nonlinear response of the system are analyzed in Fig. 4.29. In our study, three internal radial clearances are included in the investigation: 10  $\mu\text{m}$ , 30  $\mu\text{m}$  and 60  $\mu\text{m}$ . It is apparent that with the increase of internal clearance, there are corresponding growth of the nonlinear responses both in the horizontal and vertical directions (Figs. 4.29(a) and 4.29(b)). Nevertheless, the appearance of the peak resonance (close to 50 Hz) is independent of the internal radial clearance. It is also found that with the increase of internal radial clearance, the HBM becomes more difficult to converge. In general, nonlinearities in rolling element bearings become higher with the growth of internal radial clearance, thereby making the HBM difficult to converge (Villa et al., 2008).

#### 4.4 Summary

In this chapter, responses obtained via different numerical methods are investigated. Two numerical techniques are studied: the time-marching technique and harmonic balance method. Among existing methods in time-marching technique, the widely used Runge-Kutta and explicit Newmark- $\beta$  method are adopted and compared. The explicit Newmark- $\beta$  method is chosen because it is able to capture the system nonlinear behaviors while the computation is cheap. The responses and contacts within the framework the Hertz contact theory are analyzed through the time-marching technique. The internal radial clearance plays the most significant role in controlling the displacement response while the effects of mass imbalance are more important on the contact conditions. Moreover, considering the roller rotation and the ring waviness, the responses are analyzed with respect to different waviness orders. Besides, system responses through time-marching technique with Lagrange multipliers technique and forcing functions are also obtained. Then, the harmonic balance method is adopted to obtain the nonlinear response of the system and results are compared with that using the time-marching technique. The harmonic balance method is proven to be able to capture the synchronous vibration of the system.

## Chapter 5

# Non-synchronous Vibration Analysis

Analysis of the non-synchronous vibration sensitivity to roller's parameters is the main objective of the project. In the introduced roller bearing model, the frequency range of the non-synchronous vibration lies in the region causing cabin comfort issues for mid size business jets (50–200 Hz) (Pratt & Whitney, 2008). Accordingly, it is of primary interest to determine the key parameters controlling the non-synchronous vibration. The effects of the internal radial clearance, the number of rollers and the mass imbalance threshold are investigated within the frameworks of the Hertz theory and the Lagrange multipliers technique. The Cascade diagram is adopted to observe the dynamic behaviors of the rotor due to nonlinear contact forces in the frequency domain. This Cascade diagram is constructed through fast Fourier transform of periodic responses of the disk at different rotational velocities. It can correlate the signal magnitude, rotational velocity and frequency spectrum, in order to illustrate whether synchronous vibration, non-synchronous vibration or even both dominate the precessional vibration (Jing et al., 2005). Moreover, the largest non-synchronous vibration with respect to the internal radial clearance is also studied.

### 5.1 Hertz Approach

Through the Hertz approach, the non-synchronous vibration of the disk is investigated with respect to the internal radial clearance  $\gamma_0$ , the number of rollers  $N_b$  and the mass imbalance  $me$ .

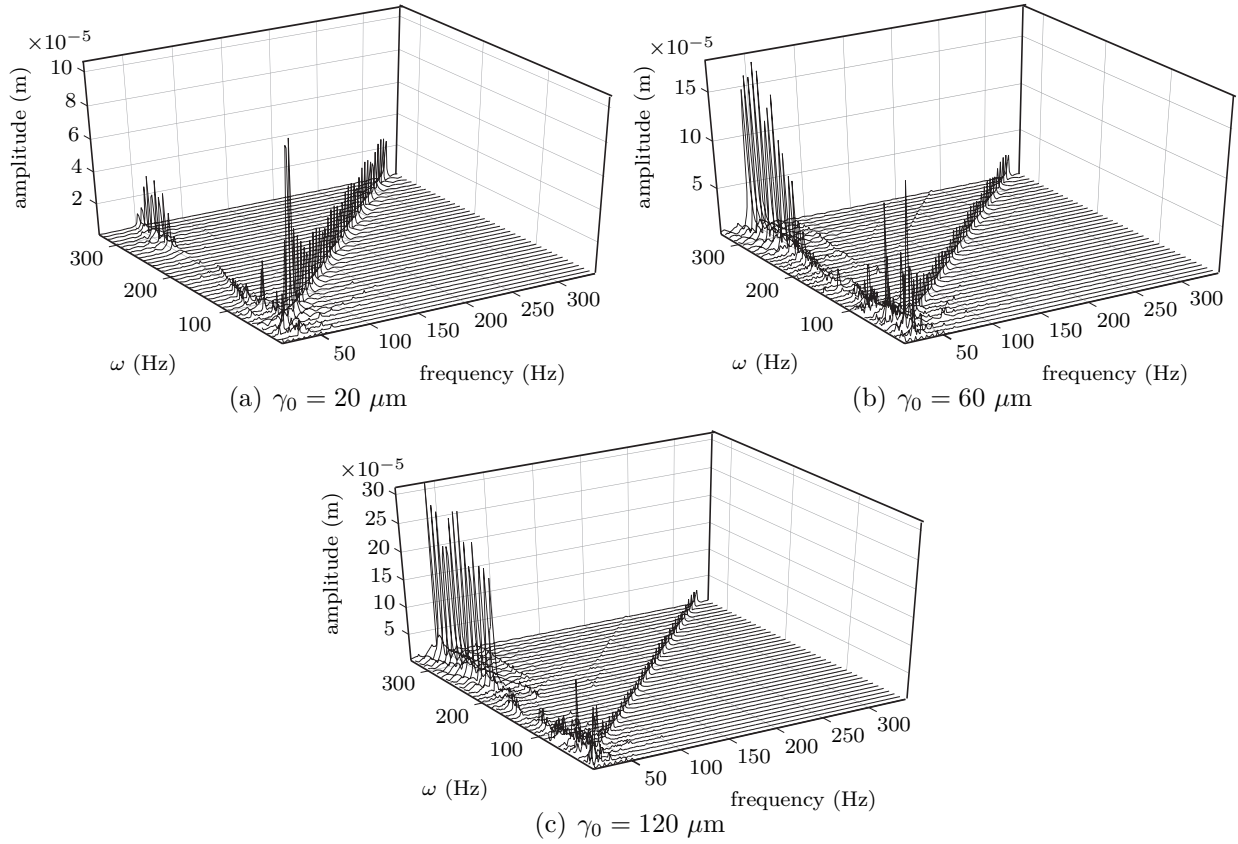


**Fig. 5.1** Cascade diagram under effects of the internal radial clearance through Hertz approach ( $N_b = 8$  and  $me = 4 \times 10^{-5}$  m)

### 5.1.1 Sensitivity to Internal Radial Clearance

First, the rotor's frequency responses under the effect of the internal radial clearance ( $\gamma_0 = 20 \mu\text{m}$ ;  $\gamma_0 = 60 \mu\text{m}$ ; and  $\gamma_0 = 120 \mu\text{m}$ ) are investigated.

With  $N_b = 8$  and  $me = 4 \times 10^{-5}$  m, the frequency responses in the framework of Cascade diagrams are illustrated in Fig. 5.1. As shown in Fig. 5.1(a), the synchronous vibration dominates in the frequency response. At  $\omega = 50$  Hz, which is also the first critical speed, the resonance appears in the synchronous vibration. At higher velocity ( $\omega = 100$  Hz), the sub-synchronous vibration appears. This sub-synchronous vibration is called whirl phenomenon which appears at twice the first critical speed (Castro et al., 2008). Compared to the resonance response, the sub-synchronous vibration is small. As the velocity keeps growing close to the second critical speed ( $\omega = 251$  Hz), the whip phenomenon appears.

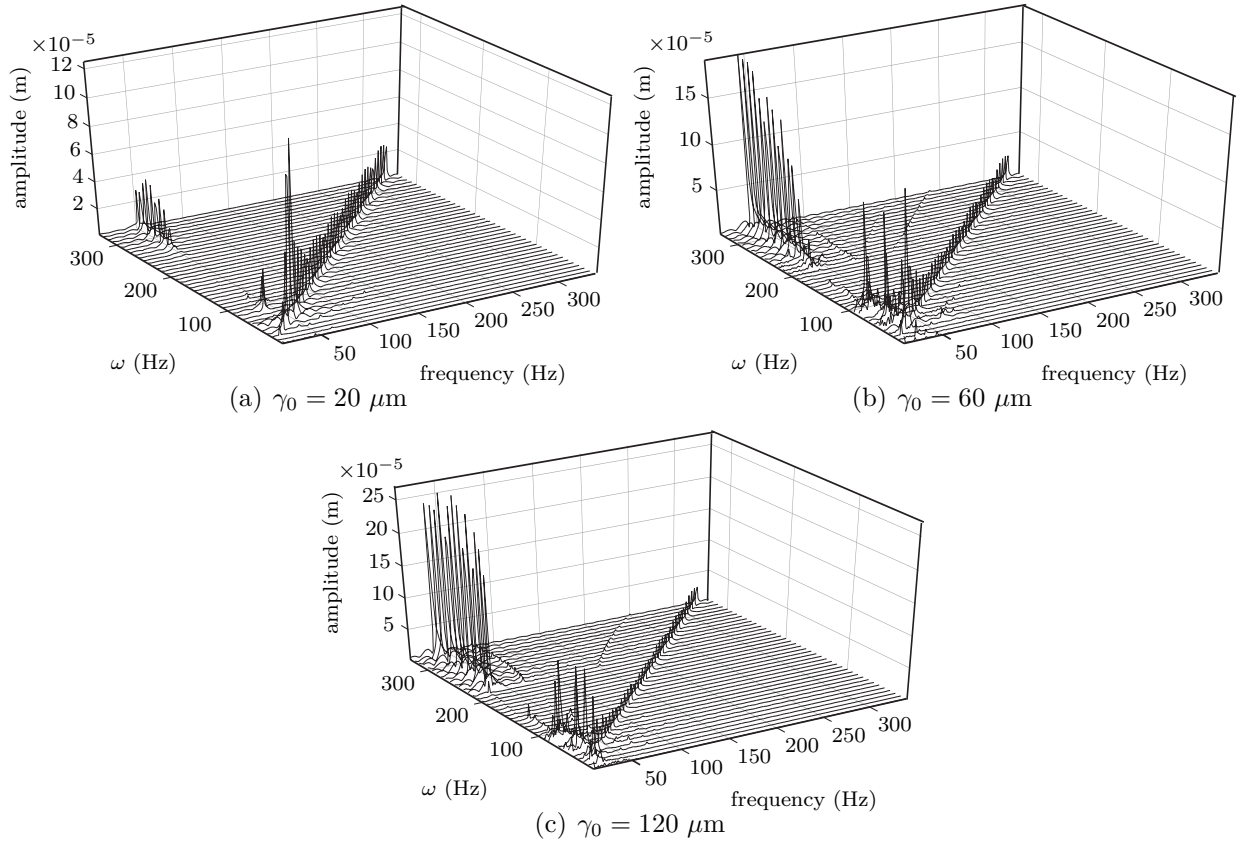


**Fig. 5.2** Cascade diagram under effects of the internal radial clearance through Hertz approach ( $N_b = 16$  and  $me = 4 \times 10^{-5}$  m)

This whip phenomenon is related to the rotor lateral forward precessional subharmonic vibration around the bearing center (Jing et al., 2005). The whip has a constant frequency which is independent of the rotational velocity. Moreover, in the frequency axis, the whip phenomenon occurs close to the first natural frequency of the rotor-bearing system, which is the so-called *frequency-locked phenomenon* (Muszynska, 1986). In general, the whip does not vary with the rotational velocity and locks close to the first resonance of the rotor (Jing et al., 2004). The amplitude of the whip is higher than that of the whirl; however, in comparison with the synchronous vibration, the whip is not dominant.

With the increase of the internal clearance, the Cascade diagrams under  $\gamma_0 = 60 \mu\text{m}$  and  $\gamma_0 = 120 \mu\text{m}$  are shown in Figs. 5.1(b) and 5.1(c), respectively. In comparison with the results under  $\gamma_0 = 20 \mu\text{m}$ , both the whirl and whip vibration grow significantly. If we look at the Cascade diagram under  $\gamma_0 = 60 \mu\text{m}$  (Fig. 5.1(b)), it is apparent that instead of only

synchronous vibration, a combination of the synchronous and non-synchronous vibration begins to dominate in the precessional vibration. If the internal radial clearance keeps increasing, the non-synchronous vibration becomes dominant (Fig. 5.1(c)). The largest amplitude of the non-synchronous vibration is close to ten times of that under  $\gamma_0 = 20 \mu\text{m}$ . Resonance still occurs close to the first natural frequency in the synchronous vibration; however, the synchronous vibration does not increase with the internal radial clearance. It is also noticeable to see that with larger internal radial clearance, the onset of the non-synchronous vibration moves towards lower rotational velocity.

The non-synchronous vibration is now analyzed with respect to the internal radial clearance for the case of  $N_b = 16$  ( $me = 4 \times 10^{-5}$  m). The corresponding Cascade diagrams under  $\gamma_0 = 20 \mu\text{m}$  are shown in Fig. 5.2(a). It can be seen that with 16 rollers, the sub-synchronous whirl vibration appears at twice of the first critical speed, and the whip phenomenon appears at the second critical speed. If the internal radial clearance is increased to  $\gamma_0 = 60 \mu\text{m}$ , similar to the case of 8 rollers, a combination of the non-synchronous and synchronous vibration dominates in the precessional vibration as depicted in Fig. 5.2(b). Moreover, the amplitude of the whip vibration is much higher than that of the whirl. If the internal radial clearance is increased further ( $\gamma_0 = 120 \mu\text{m}$ ), the non-synchronous vibration grows significantly (Fig. 5.2(c)). Also, the non-synchronous vibration begins to dominate. For all cases, the onset of the non-synchronous vibration stays close to the second critical speed ( $\omega = 251$  Hz) which is independent of internal radial clearance.

### 5.1.2 Sensitivity to Mass Imbalance

After the analysis of the effect of the internal radial clearance, numerous simulations are conducted to study the effect of the mass imbalance ( $me = 1 \times 10^{-5}$  m;  $me = 2 \times 10^{-5}$  m; and  $me = 4 \times 10^{-5}$  m) on the non-synchronous vibration.

With  $N_b = 8$  and  $\gamma_0 = 20 \mu\text{m}$ , the frequency responses with respect to the mass imbalance are illustrated in Fig. 5.3. For a low mass eccentricity ( $me = 1 \times 10^{-5}$  m), it is apparent that only the synchronous vibration dominates in the precessional vibration and the non-synchronous vibration is negligible (Fig. 5.3(a)). If the mass eccentricity is increased to  $2 \times 10^{-5}$  m, the synchronous vibration increases, and the non-synchronous vibration is still negligible (Fig. 5.3(b)). Nevertheless, the non-synchronous vibration increases significantly with a further increase of the mass eccentricity (Fig. 5.3(c)). With  $me = 4 \times 10^{-5}$  m, the

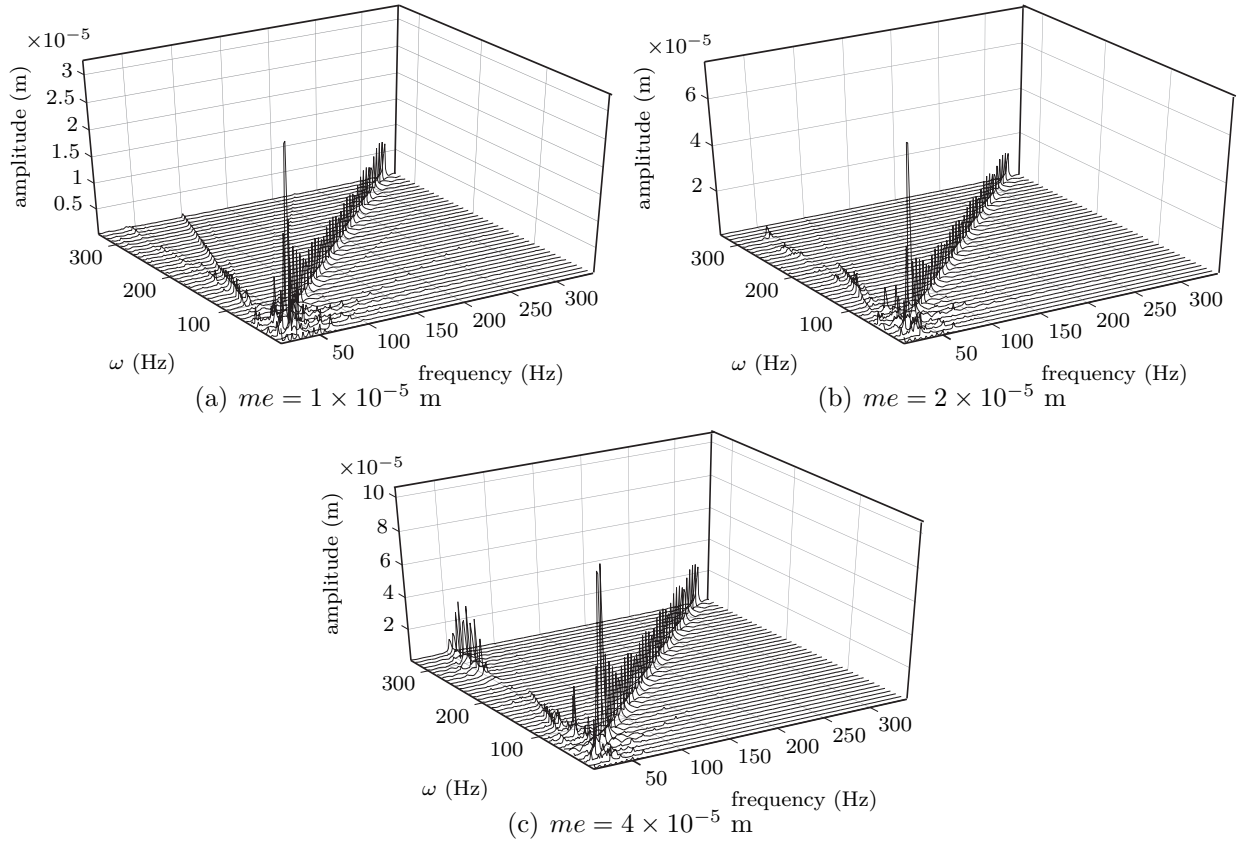


**Fig. 5.3** Cascade diagram under effects of the mass imbalance through Hertz approach ( $N_b = 8$  and  $\gamma_0 = 20 \mu\text{m}$ )

synchronous vibration is no longer the only vibration in the Cascade diagram. Although the non-synchronous vibration is still small in comparison with the synchronous vibration, it is not negligible. It is also noticeable to see that the sub-synchronous whirl phenomenon appears at  $\omega = 100$  Hz, and its amplitude is the same as that of the whip phenomenon.

Similar conclusions can be drawn from the frequency responses under  $\gamma_0 = 60 \mu\text{m}$  as shown in Fig. 5.4. Both the synchronous and non-synchronous vibrations grow with the increase of the mass imbalance, and non-synchronous vibration grows even faster. Also, the non-synchronous vibration becomes more dominant due to the increase of the mass imbalance.

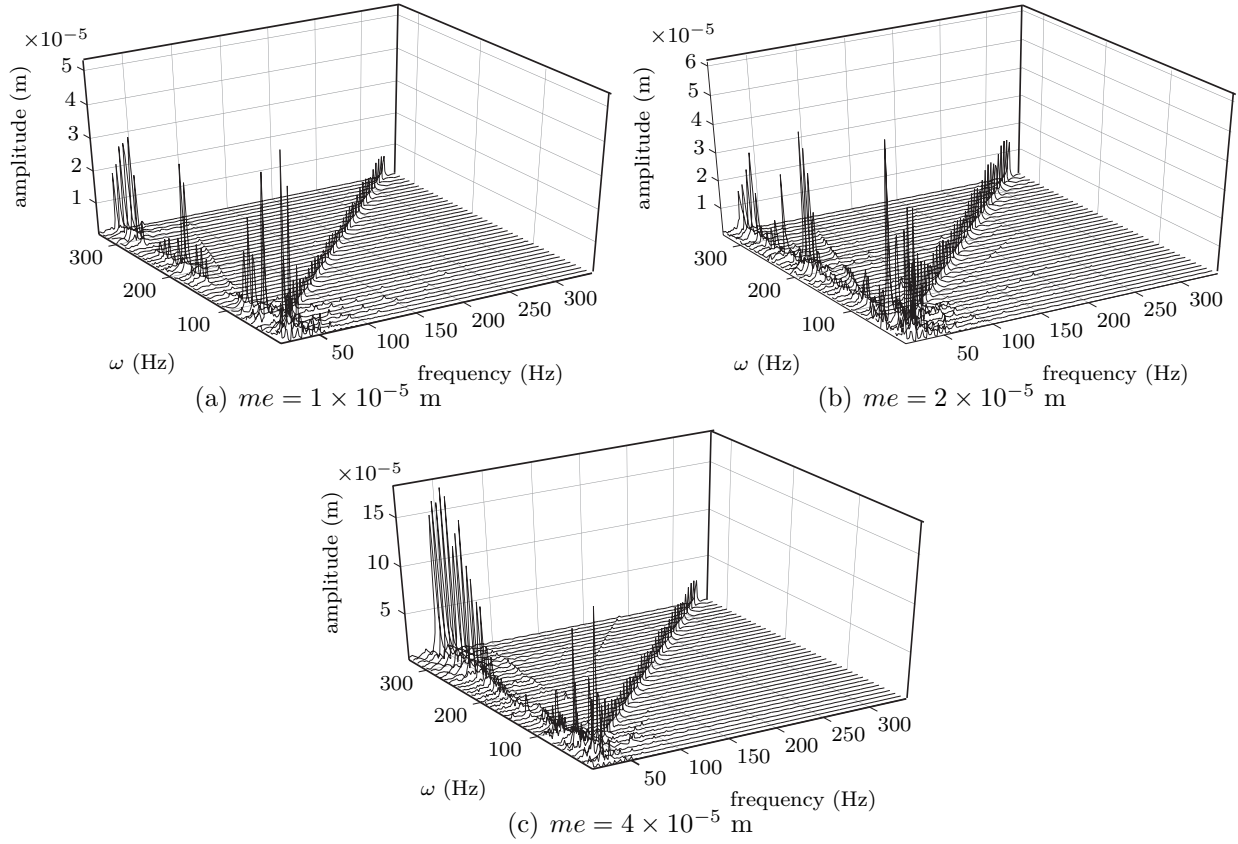


**Fig. 5.4** Cascade diagram under effects of the mass imbalance through Hertz approach ( $N_b = 8$  and  $\gamma_0 = 60 \mu\text{m}$ )

### 5.1.3 Sensitivity to Number of Rollers

Afterwards, the non-synchronous vibration with respect to the number of rollers ( $N_b = 8$ ;  $N_b = 16$ ; and  $N_b = 32$ ) is studied.

For the case of  $\gamma_0 = 20 \mu\text{m}$  and  $me = 4 \times 10^{-5}$  m, the frequency responses of the disk with respect to the number of rollers are illustrated in the Cascade diagrams in Fig. 5.5. It is apparent that the number of rollers does not have an important effect on the non-synchronous vibration. For all cases, the onset of the non-synchronous whip is close to  $\omega = 250$  Hz, and the amplitude is close to  $3 \times 10^{-5}$  m. Besides, the sub-synchronous whirl also appears at twice the first critical speed. It is noticeable that for all cases, the synchronous vibration dominates in the frequency response. Similarly, with  $\gamma_0 = 120 \mu\text{m}$  and  $me = 4 \times 10^{-5}$  m, the effect of the number of rollers on the non-synchronous vibration

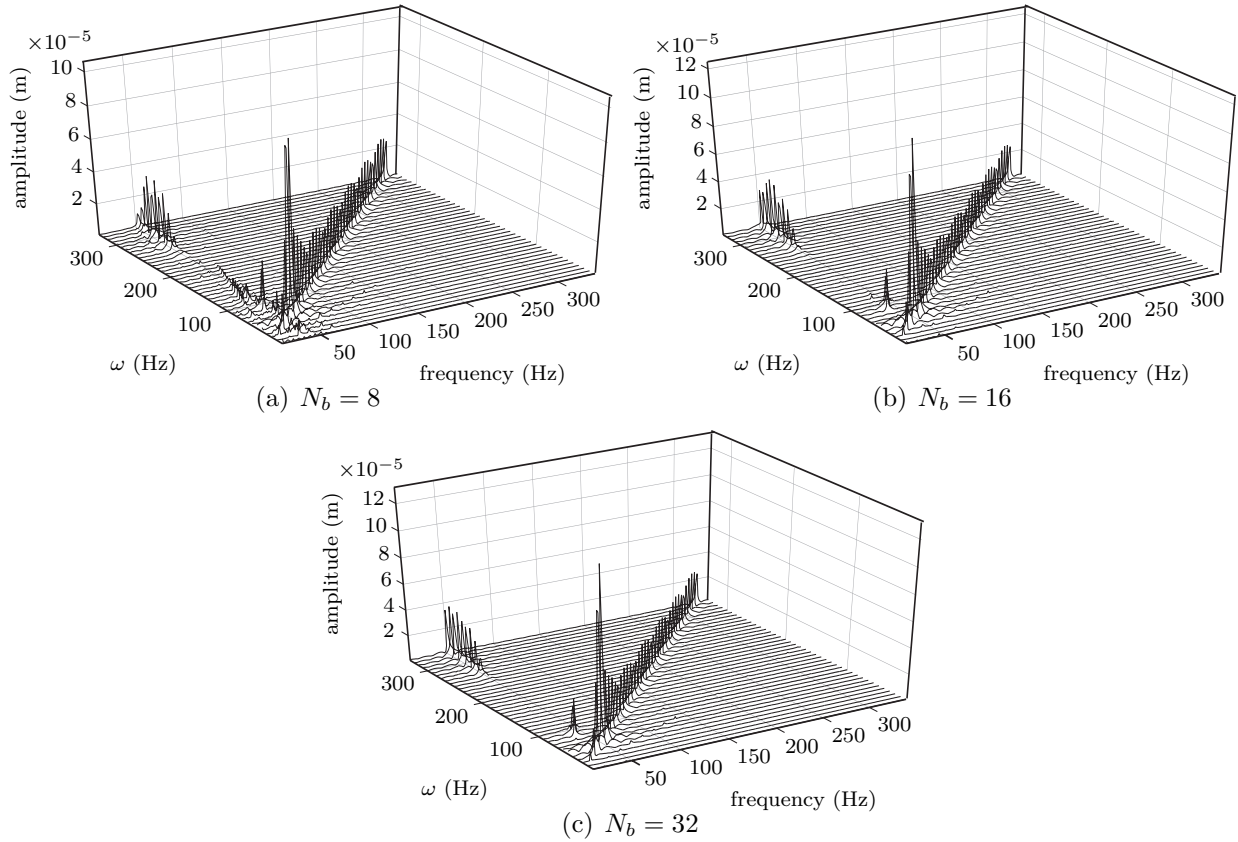


**Fig. 5.5** Cascade diagram under effects of the number of rollers through Hertz approach ( $me = 4 \times 10^{-5}$  m and  $\gamma_0 = 20 \mu\text{m}$ )

are illustrated in Fig. 5.6. It can be seen that with the increase of the number of rollers, the largest non-synchronous vibration decreases very slightly. In general, in comparison with internal radial clearance and mass imbalance, the number of rollers plays much less important roles on the non-synchronous vibration.

## 5.2 Lagrange Multipliers Approach

For comparison purposes, the Lagrange multipliers technique is also employed. Similarly, the non-synchronous vibration is analyzed with respect to the internal radial clearance, the mass imbalance and the number of rollers.

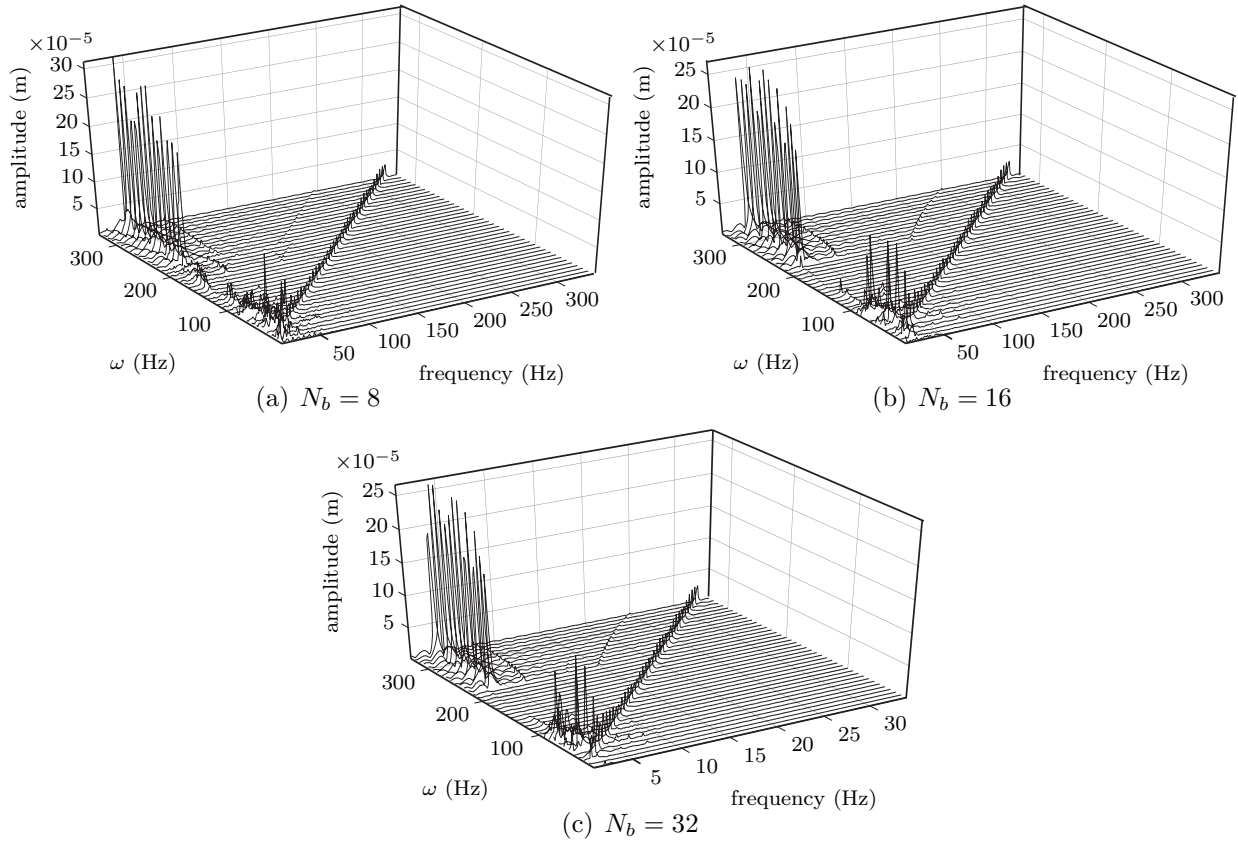


**Fig. 5.6** Cascade diagram under effects of the number of rollers through Hertz approach ( $me = 4 \times 10^{-5}$  m and  $\gamma_0 = 120 \mu\text{m}$ )

### 5.2.1 Sensitivity to Internal Radial Clearance

Through the Lagrange multipliers technique, the non-synchronous vibration with respect to the internal radial clearance is illustrated in Fig. 5.7. Analogous to the frequency responses through the Hertz approach, the non-synchronous vibration becomes much more significant with the increase of the internal clearance. Similarly, it is also noticeable that under higher internal clearance, the appearance of resonance in the synchronous vibration moves to lower frequency (not exact 50 Hz) slightly. This is due to the fact that the natural frequencies of the system are relevant to the internal radial clearance, and their relationship will be studied through nonlinear normal modes in the future work.

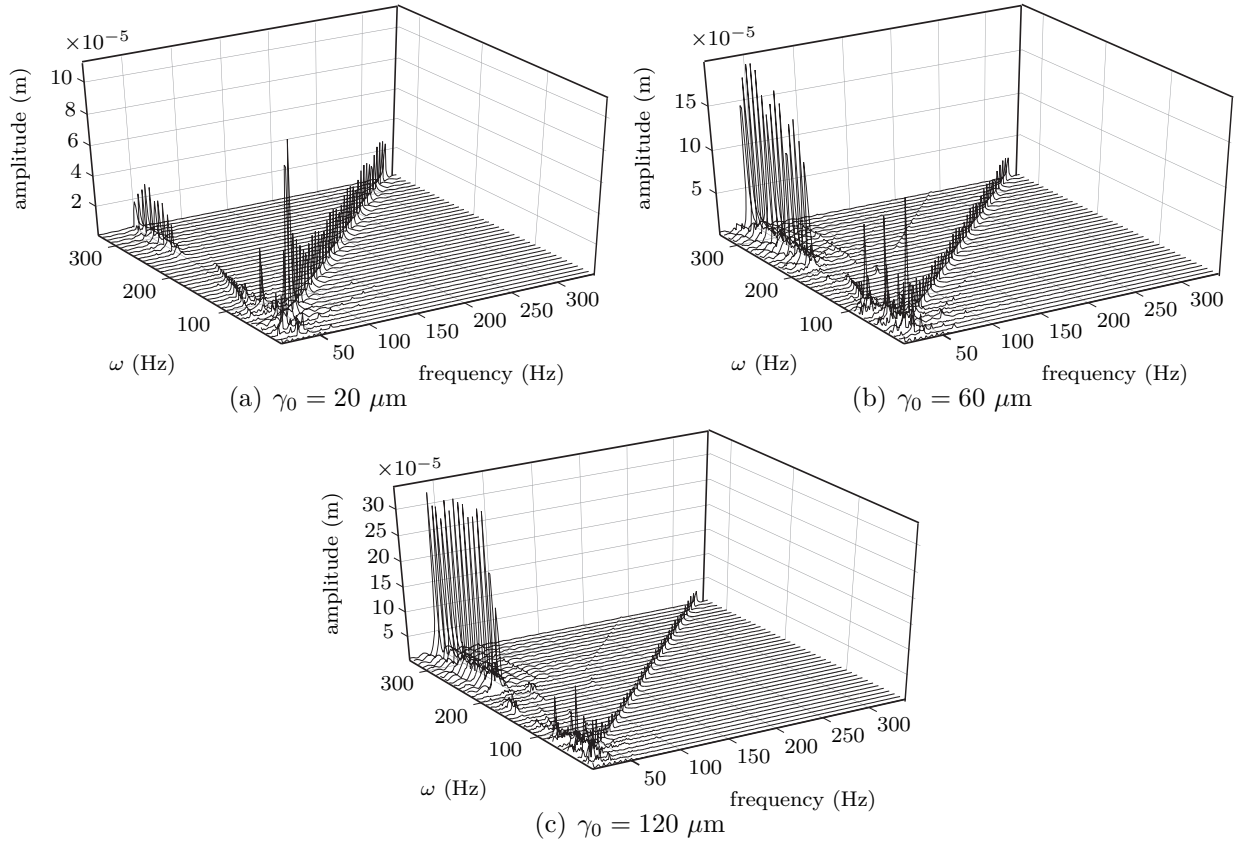


**Fig. 5.7** Cascade diagram under effects of the internal radial clearance through Lagrange multipliers approach ( $N_b = 8$  and  $me = 4 \times 10^{-5}$  m)

### 5.2.2 Sensitivity to Mass Imbalance

Similar results are obtained through the Lagrange multipliers technique for the influence of the mass imbalance on the non-synchronous vibration. It can be seen from Fig. 5.8 that with the increase of the mass imbalance, there is a corresponding growth of both the synchronous and non-synchronous vibrations. Also, it is of interest to see that the sub-synchronous whirl phenomenon grows significantly with higher mass imbalance.

### 5.2.3 Sensitivity to Number of Rollers

Within the framework of the Lagrange multipliers technique, the non-synchronous vibrations with respect to the number of rollers are shown in Fig. 5.9. Still, in comparison with the internal radial clearance and the mass imbalance, the effects of the number of

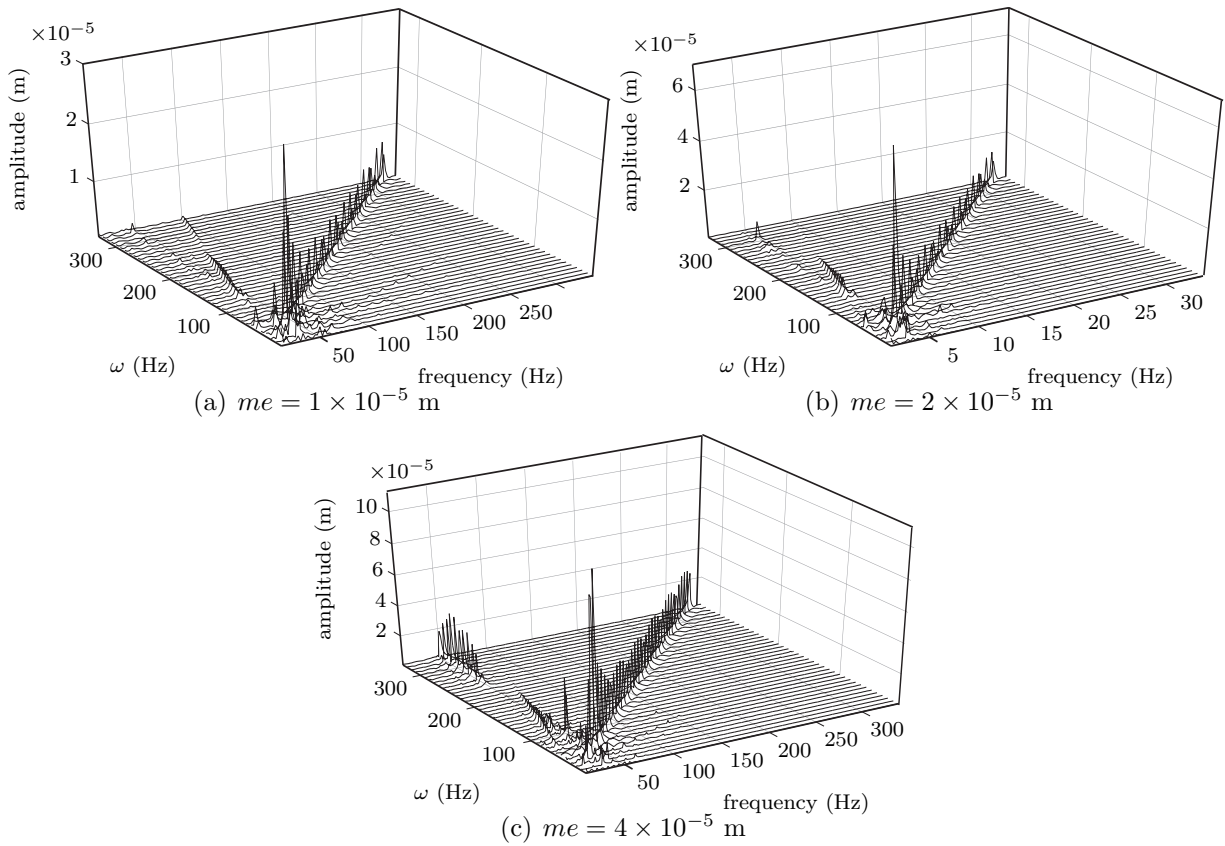


**Fig. 5.8** Cascade diagram under effects of the mass imbalance through Lagrange multipliers approach ( $N_b = 8$  and  $\gamma_0 = 20 \mu\text{m}$ )

rollers on the non-synchronous vibration are nonsignificant.

In general, through both the Hertz and the Lagrange multipliers approaches, very similar observations can be detailed: the non-synchronous vibration is affected by all the existing parameters, while the internal clearance is the key factor. It is also noticeable that both the non-synchronous and synchronous vibrations are controlled by the parameters of the roller bearing itself and are invariant with respect to the solution methods adopted (Hertz contact theory and Lagrange multipliers technique).

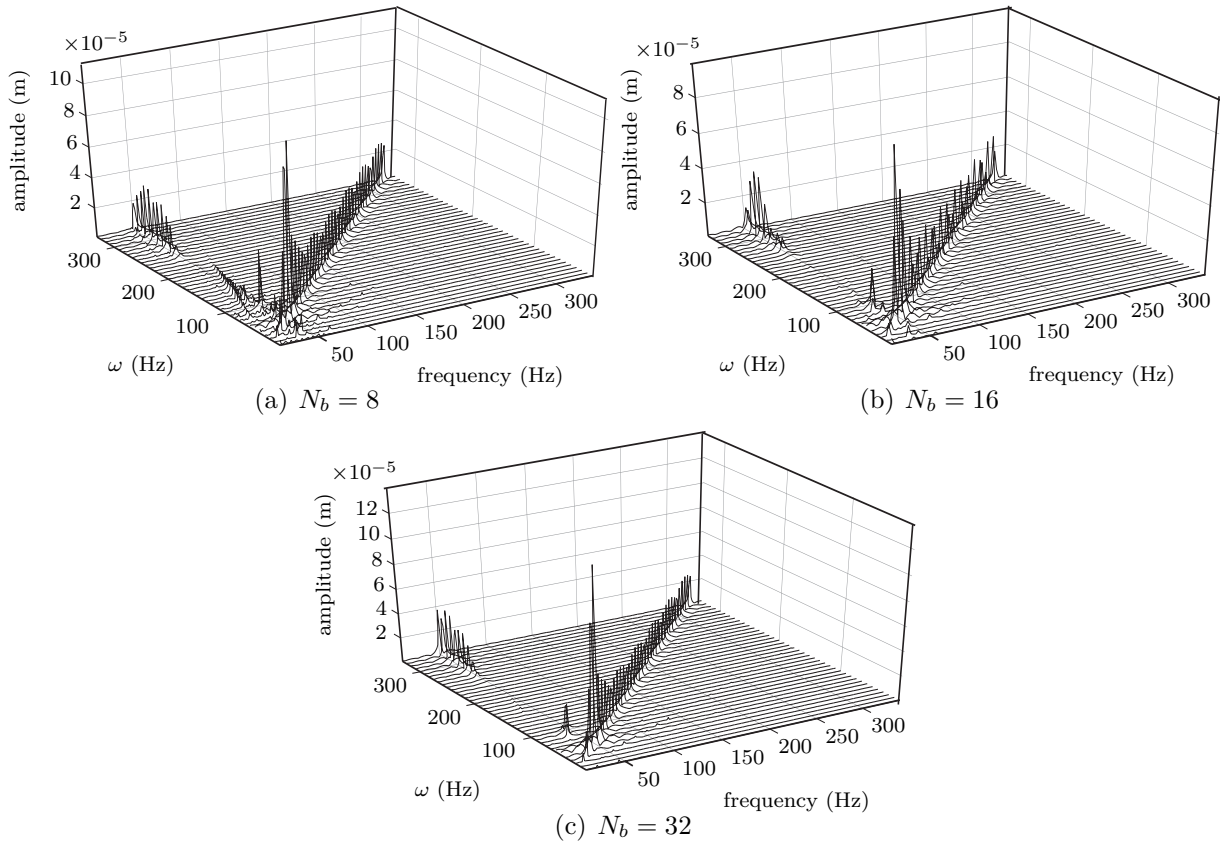


**Fig. 5.9** Cascade diagram under effects of the number of rollers through Lagrange multipliers approach ( $\gamma_0 = 20 \mu\text{m}$  and  $me = 4 \times 10^{-5} \text{ m}$ )

### 5.3 Largest Non-synchronous Vibration with Internal Radial Clearance

In engineering applications, the non-synchronous vibration is one important source of the failure of rotor-bearing systems and should be avoided (Crandall, 1990). Since the internal radial clearance plays the most significant role in controlling the non-synchronous vibration, it makes sense to obtain the relationship of the largest non-synchronous vibration with respect to the internal radial clearance. This relationship is possible to predict dangerous behaviors of the system with respect to the internal clearance.

From above analysis, the largest amplitude of the non-synchronous vibration is invariant with solution methods adopted. By means of the Hertz contact theory, the largest non-synchronous vibration with respect to the internal radial clearance is illustrated in Fig. 5.10

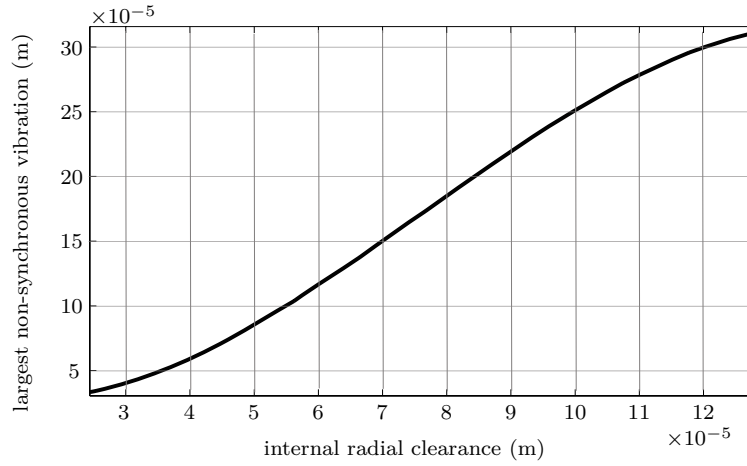


**Fig. 5.10** Largest non-synchronous vibration with respect to internal radial clearance ( $me = 4^{-5}$  m and  $N_b = 8$ )

( $N_b = 8$  and  $me = 4 \times 10^{-5}$  m). It can be seen that the largest non-synchronous vibration obeys a nonlinear relation with the internal radial clearance. Following Fleming et al. (2006), the curve fitting technique is used to formulate their relationship as:

$$\delta_{nsv} = P_1\gamma^3 + P_2\gamma^2 + P_3\gamma + P_4 \quad (5.1)$$

where  $\delta_{nsv}$  is the largest non-synchronous vibration,  $P_i$  ( $i = 1, \dots, 4$ ) are the fitted coefficients,  $\gamma$  is the internal radial clearance. The curve fitting coefficients are listed in Table 5.1.

**Table 5.1** Curve fitting coefficients for the largest non-synchronous vibration

Curve fitting coefficient	Values
$P_1$	$-3.125 \times 10^8$
$P_2$	$7.162 \times 10^4$
$P_3$	-1.956
$P_4$	$4.296 \times 10^{-5}$

Through this procedure, the relationship of the largest non-synchronous vibration with respect to the internal clearance is obtained. Thus, it is significant to avoid the possibility of failures of the system relevant to the internal clearance in specific working conditions.

## 5.4 Summary

In this chapter, the non-synchronous vibration in the rotor-bearing system is studied. Effects of the internal radial clearance, the number of rollers and the mass imbalance on the non-synchronous vibration are investigated. Cascade diagrams obtained via the Hertz theory and Lagrange multipliers technique are employed to study the non-synchronous vibration. The effect of the number of rollers are less significant in comparison with that of the internal clearance and the mass imbalance. Among the existing parameters, the internal radial clearance plays the most important role in controlling the non-synchronous vibration. In general, both the non-synchronous and synchronous vibration in roller bearings are controlled by the bearing's parameters, not by the contact approaches adopted. Finally, the relation of the largest non-synchronous vibration with respect to the internal radial clearance is extracted using curve fitting.



# Chapter 6

## Closing Remarks

### 6.1 Conclusions

In this work, a Jeffcott rotor bearing system with a flexible shaft and two supporting roller bearings is investigated in details. The excitation forces are the unbalanced forces added on the central disk, and the nonlinearity is due to the contact between rollers and the outer ring in supporting roller bearings. In order to construct the model mathematically, the finite element method is adopted.

Modal analysis is conducted on the linear model in which the supporting bearings are represented as a set of springs and dampers. Mode shapes of the system are obtained through the complex eigenvalue analysis, and the first critical speed (50 Hz) is found based on the Campbell diagram. Moreover, through modal analysis, the shaft is divided into 20 beam elements for the invariance of natural frequencies with respect to the mesh density. In order to reduce the computational efforts, modal reduction technique is used. In our system, the number of nonlinear DOFs is small in comparison with the total DOFs; hence, the computational efforts will be expected to reduce substantially. The Craig-Bampton modal reduction technique is adopted to reduce the system size with the advantage of high modal accuracy and low computational costs. System responses of the reduced-order model do good jobs in matching with that of the full-order model while the computational efforts are reduced significantly.

Based on the Jeffcott rotor model, contacts in the supporting roller bearing are studied. Actually, the modeling of bearing contacts is a complicated task which depends on many parameters under operating conditions, such as internal radial clearance, rotational velocity,

thermal expansion, etc. In our study, two approaches are adopted to handle the contacts: the Hertz theory and the Lagrange multipliers technique. Also, on the basis of the Hertz theory, the forcing function is extracted. This forcing function is the direct relationship of the contact force and bearing deflection with respect to the rotational velocity and is of interest to engineers in some specific working conditions. Besides, in the bearing model, the expansion of the internal clearance due to oil-flow effects at high speeds is studied. This expansion is investigated with respect to the rotational velocity and their relationship is extracted using curve fitting. In addition, with the help of the Hertz theory, the equivalent stiffness of the roller bearing is also studied through the linearization method. In this method, the stiffness is obtained by linearizing the contact forces over the rotor's displacements. Through this procedure, the vertical and horizontal bearing stiffness with respect to the internal clearance is calculated. Both of them remain constant under large internal clearance (for the horizontal case,  $\gamma_0 \geq 30 \mu\text{m}$ ; for the vertical case,  $\gamma_0 \geq 60 \mu\text{m}$ ). If the internal radial clearance is reduced further, both the horizontal and vertical stiffness increase rapidly. It is also noticeable that the coupling stiffness in the roller bearing is independent of the internal radial clearance.

In our study, both the time-marching technique and harmonic balance method are applied to solve the system governing equations. Among the time-marching techniques, both the Runge-Kutta method and the explicit Newmark- $\beta$  method are used. The responses obtained through Runge-Kutta and Newmark- $\beta$  method match well, and the computation through the Newmark- $\beta$  method is much cheaper. Thanks to this time-marching technique, the non-synchronous vibration of the system can be captured. Following the time-marching technique, a comparison of the time responses obtained via the Hertz theory and the Lagrange multipliers technique is conducted. Penetration is detected for the Hertz approach; while in the Lagrange multipliers technique, the rotor's maximum radial displacement is equivalent to the internal clearance. No penetration is detected. Through investigation, the internal radial clearance is proven to be the key factor in controlling the system responses, while the mass imbalance is the most significant parameter in the nature of contact forces. Besides, based on the time-marching technique, two cases are investigated through forcing functions. Furthermore, the time responses via forcing functions and the Hertz theory are compared, and they match well. Unlike the time-marching technique, the harmonic balance method transforms the displacement responses and nonlinear forces in the frequency domain. Thus, the second-order nonlinear differential equations are transformed into a set

of nonlinear algebraic equations. In our analysis, the nonlinear responses obtained by the harmonic balance method and time-marching technique are compared. The harmonic balance method is able to capture the synchronous vibration, while, for the non-synchronous vibration, it is not applicable. In addition, the effects of harmonic components and the internal clearance on the rotor's nonlinear response are investigated. Harmonic components become less important with the increase of their orders. Moreover, it is also noticeable that the internal radial clearance is the main factor controlling the convergence of the harmonic balance method.

Finally, the non-synchronous vibration is studied. Through fast Fourier transform of the periodic responses for each rotational velocity, the Cascade diagram is obtained to investigate the non-synchronous vibration. Effects of the mass imbalance, the internal radial clearance and the number of rollers on the non-synchronous vibration are analyzed in details. Among these parameters, the internal radial clearance is the most significant factor in the nature of the non-synchronous vibration. In addition, the nonlinear relationship of the largest non-synchronous vibration with respect to the internal radial clearance is extracted using curve fitting. Since the non-synchronous vibration is an important source of failures of rotating systems, this relationship is able to predict possible dangerous operating conditions.

## 6.2 Future Work

As an extension to the current work, several issues remain to be investigated further in the future:

- The case of roller bearings with flexible rings is not included in this work. In some specific operating conditions, the ring flexibilities are not negligible, and this flexible effects need to be considered in the roller bearing model;
- The variance of the internal radial clearance due to thermal effects is to be conducted, and forcing functions are to be extracted with thermal effects;
- The nonlinear normal modes of the rotor bearing system are to be conducted (Legrand et al., 2002);

- A more complex industrial rotor bearing model will be adopted in order to study the bearing contacts and the non-synchronous vibration.

## References

- M. L. Adams. *Rotating Machinery Vibration*. Marcel Dekker, Inc, 1999.
- C. Bai and Q. Xu. Dynamic model of ball bearings with internal clearance and waviness. *Journal of Sound and Vibration*, 294:23–48, 2006.
- T. M. Cameron and J. H. Griffin. An alternating frequency time domain method for calculating the steady state response of nonlinear dynamic systems. *Journal of Applied Mechanics*, 56:149–154, 1989.
- N. Carpenter, R. Taylor, and M. Katona. Lagrange constraints for transient finite element surface contact. *International Journal for Numerical Methods in Engineering*, 32:103–128, 1991.
- H. F. Castro, K. L. Cavalca, and R. Nordmann. Whirl and whip instabilities in rotor-bearing system considering a nonlinear force model. *Journal of Sound and Vibration*, 317:273–293, 2008.
- R. D. Cook and W. C. Young. *Advanced Mechanics of Materials*. Prentice Hall, 1999.
- R. R. Craig and M. C. C. Bampton. Coupling of substructures for dynamic analysis. *AIAA Journal*, 6:1313–1319, 1968.
- S. Crandall. From whirl to whip in rotordynamics. Lyon, France, 1990. Transactions of IFToMM Third International Conference on Rotordynamics.
- A. D. Dimarogonas and S. A. Paipetis. *Analytical Methods in Rotor Dynamics*. Applied Science, London, 1983.
- S. Faik and H. Witteman. Modelling of impact dynamics: a literature survey. Orlando, USA, 2000. International ADAMS User Interface Conference.
- D. P. Fleming and J. V. Poplawski. Unbalance response prediction for accelerating rotors on ball bearings with load-dependent nonlinear bearing stiffness. *International Journal of Rotating Machinery*, 1:53–59, 2005.

- D. P. Fleming, B. T. Murphy, J. T. Sawicki, and J. V. Poplawski. Transient response of rotor on rolling element bearings with clearance. Vienna, Austria, 2006. Seventh International Conference on Rotor Dynamics.
- G. Groll and D. J. Ewins. The harmonic balance method with arc-length continuation in rotor/stator contact problems. *Journal of Sound and Vibration*, 241:223–233, 1989.
- R. J. Guyan. Reduction of stiffness and mass matrices. *AIAA Journal*, 3, 1965.
- T. A. Harris. *Rolling Bearing Analysis*. John Wiley and Sons, 2001.
- T. A. Harris and M. N. Kotzalas. *Advanced concepts of bearing technology*. Taylor & Francis, 2006a.
- T. A. Harris and M. N. Kotzalas. *Essential concepts of bearing technology*. Taylor & Francis, 2006b.
- S. P. Harsha. Nonlinear dynamic analysis of a high-speed rotor supported on rolling element bearings. *Journal of Sound and Vibration*, 29, 2006a.
- S. P. Harsha. Nonlinear dynamic response of a balanced rotor supported by rolling element bearings due to internal radial clearance effect. *Mechanism and Machine Theory*, 41: 688–706, 2006b.
- M. W. Hirsch and S. Smale. *Differential Equations, Dynamical Systems, and Linear Algebra*. Academic Press, New York, 1974.
- H. Hu and J. H. Tang. Solution of a duffing-harmonic oscillator by the method of harmonic balance. *Journal of Sound and Vibration*, 294:637–639, 2006.
- J. Jing, G. Meng, Y. Sun, and S. Xia. On the non-linear dynamic of a rotor-bearing system. *Journal of Sound and Vibration*, 274:1031–1044, 2004.
- J. P. Jing, G. Meng, and S. B. Xia. On the oil-whipping of a rotor-bearing system by a continuum model. *Applied Mathematical Modelling*, 29:461–475, 2005.
- K. B. Kim and S. T. Noah. Bifurcation analysis for a modified jeffcott rotor with bearing clearances. *Nonlinear Dynamics*, 1:221–241, 1990.
- M. Lalanne and G. Ferraris. *Rotordynamics Prediction in Engineering*. John Wiley and Sons, 1998.
- M. Legrand, D. Jiang, C. Pierre, and S. W. Shaw. Nonlinear normal modes of a rotating shaft based on the invariant manifold method. *International Journal of Rotating Machinery*, 10:319–335, 2002.

- M. Leontiev, V. Karasev, and Degtiarev. S. Dynamics of a rotor in roller bearings. *Vibration of Machines: measurement, reduction, protection*, 1:45–50, 2007.
- T. C. Lim and R. Singh. Vibration transmission through rolling element bearings, part i: bearing stiffness formulaton. *Journal of Sound and Vibration*, 139:179–199, 1989.
- L. Meirovitch. *Fundamentals of Vibrations*. McGraw-Hill Book Co., 2001.
- A. R. Mijar and J. S. Arora. Review of formulations for elastostatic frictional contact problems. *Struct Multidisc Optimum*, 20:167–189, 2000.
- A. Muszynska. Whirl and whip rotor/bearing stability problems. *Journal of Sound and Vibration*, 110:443–462, 1986.
- A. Muszynska. Stability of whirl and whip in rotor bearing system. *Journal of Sound and Vibration*, 127:49–64, 1988.
- H. D. Nelson and J. M. McVaugh. The dynamics of rotor-bearing system using finite elements. *Journal of Engineering for Industry*, pages 593–600, 1976.
- A. Palmgren. *Ball and Roller Bearing Engineering*. SKF Industries, Los Angeles, 1945.
- C. A. Papadopoulos, P. G. Nikolakopoulos, and G. D. Gounaris. Identification of clearances and stability analysis for a rotor-journal bearing system. *Mechanism and Machine Theory*, 43:411–426, 2007.
- Pratt & Whitney. *Pratt & Whitney Project Description*. Pratt & Whitney, Canada, 2008.
- W. Qin, G. Chen, and G. M. Nonlinear response of a rub-impact overhung rotor. *Chaos, Solitons & Fractals*, 19:1161–1172, 2004.
- Z. Q. Qu. Model reduction for dynamical systems with local nonlinearities. *AIAA Journal*, 40:327–333, 2002.
- M. N. Sahinkaya, A. H. Abulrub, P. S. Keogh, and C. R. Burrows. Multiple sliding and rolling contact dynamics for a flexible rotor/magnetic bearing system. *IEEE/ASME Transactions on Mechatronics*, 12:179–189, 2007.
- J. J. Sinou. Non-linear dynamics and contacts of an unbalanced flexible rotor supported on ball bearings. *Mechanism and Machine Theory*, 44:1713–1732, 2009.
- H. Tamura, E. H. Gad, T. Kondou, T. Ayabe, and A. Sueoka. On the static running accuracy of ball bearings. *Bulletin of JSME*, 28:1240–1246, 1985.
- M. Tiwari and K. Gupta. Effect of radial internal clearance of a ball bearing on the dynamics of a balanced horizontal rotor. *Journal of Sound and Vibration*, 238:723–756, 2000.

- 
- R. Tiwari and N. S. Vyas. Stiffness estimation from random response in multi-mass rotor bearing systems. *Prob. Engng. Mech*, 13:255–268, 1998.
- C. Villa, J. J. Sinou, and F. Thouverez. Stability and vibration analysis of a complex flexible rotor bearing system. *Communciations in Nonlinear Science and Numerical Simulation*, 13:804–821, 2008.
- C. V. S. Villa, J. J. Sinou, and F. Thouverez. The invariant manifold approach applied to nonlinear dynamics of a rotor-bearing system. *European Journal of Mechanics-A/Solids*, 24:676–689, 2005.
- L. Wang, L. Cui, D. Zheng, and L. Gu. Nonlinear dynamics behaviors of a rotor roller bearing system with radial clearances and waviness considered. *Chinese Journal of Aeronautics*, 21:86–11, 2007.
- A. J. White and J. B. Young. Time-marching method for the prediction of two-dimensional, unsteady flows of condensing steam. *Journal of Propulsion and Power*, 9:579–587, 1993.
- T. Zheng and N. Hasebe. An efficient analysis of high-order dynamical system with local nonlinearity. *Journal of Vibration and Acoustics*, 121:408–416, 1999.

# Appendix A

## Elementary Matrices

The elementary translational mass matrix is:

$$[M_T]^e = \frac{\rho A l}{420} \begin{bmatrix} 156 & & & & & & & & \text{sym} \\ 0 & 156 & & & & & & & \\ 0 & -22l & 4l^2 & & & & & & \\ 22l & 0 & 0 & 4l^2 & & & & & \\ 54 & 0 & 0 & 13l & 156 & & & & \\ 0 & 54 & -13l & 0 & 0 & 156 & & & \\ 0 & 13l & -3l^2 & 0 & 0 & 22l & 4l^2 & & \\ -13l & 0 & 0 & -3l^2 & -22l & 0 & 0 & 4l^2 & \end{bmatrix}$$

The elementary rotational mass matrix is:

$$[M_R]^e = \frac{\rho A R^2}{120l} \begin{bmatrix} 36 & & & & & & & & \text{sym} \\ 0 & 36 & & & & & & & \\ 0 & -3l & 4l^2 & & & & & & \\ 3l & 0 & 0 & 4l^2 & & & & & \\ -36l & 0 & 0 & -3l & 36 & & & & \\ 0 & -36 & 3l & 0 & 0 & 36 & & & \\ 0 & -3l & -l^2 & 0 & 0 & 3l & 4l^2 & & \\ 3l & 0 & 0 & -l^2 & -3l & 0 & 0 & 4l^2 & \end{bmatrix}$$

The elementary gyroscopic matrix is:

$$[G]^e = \frac{2\rho AR^2}{120l} \begin{bmatrix} 0 & & & & & & & \text{skew} & \text{sym} \\ 36 & 0 & & & & & & & \\ -3l & 0 & 0 & & & & & & \\ 0 & -3l & 4l^2 & 0 & & & & & \\ 0 & 36 & -3l & 0 & 0 & & & & \\ -36 & 0 & 0 & -3l & 36 & 0 & & & \\ -3l & 0 & 0 & l^2 & 3l & 0 & 0 & & \\ 0 & -3l & -l^2 & 0 & 0 & 3l & 4l^2 & 0 & \end{bmatrix}$$

where  $\rho$  is the density,  $R$  is the radius,  $A$  is the cross section,  $l$  is the length of the beam element.

The elementary stiffness matrix is:

$$[K]^e = \frac{EI}{l^3} \begin{bmatrix} 12 & & & & & & & & \text{sym} \\ 0 & 12 & & & & & & & \\ 0 & -6l & 4l^2 & & & & & & \\ 6l & 0 & 0 & 4l^2 & & & & & \\ -12l & 0 & 0 & -6l & 12 & & & & \\ 0 & -12 & 6l & 0 & 0 & 12 & & & \\ 0 & -6l & 2l^2 & 0 & 0 & 6l & 4l^2 & & \\ 6l & 0 & 0 & 2l^2 & -6l & 0 & 0 & 4l^2 & \end{bmatrix}$$

where  $E$  is the elastic modulus of the shaft,  $I$  is the second inertial.

# Appendix B

## Forcing Functions Coefficients

**Table B.1** Curve fitting coefficients for internal radial clearance

Curve fitting coefficients	Internal radial clearance (m)
$a_0$	0.0006353
$a_1$	$2.129 \times 10^{-7}$
$a_2$	$-9.172 \times 10^{-12}$
$a_3$	$1.535 \times 10^{-16}$
$a_4$	$-9.53 \times 10^{-22}$

**Table B.2** Forcing function coefficients

Curve fitting coefficients	Mass eccentricity $4 \times 10^{-5}$ m	Mass eccentricity $2 \times 10^{-5}$ m
$a_0$	3378	4115
$a_1$	$3.504 \times 10^8$	$3.13 \times 10^8$
$b_0$	1.089	1.085
$b_1$	$6.945 \times 10^{-7}$	$7.21 \times 10^{-7}$